



HAL
open science

Stability of antigorite serpentinite and geochemical exchange with oceanic crustal rocks during ultrahigh-pressure subduction-zone metamorphism (Lago di Cignana Unit, Italian Western Alps)

Mattia Gilio, Marco Scambelluri, Samuele Agostini, Marguerite Godard,
Daniel Peters, Thomas Pettke

► To cite this version:

Mattia Gilio, Marco Scambelluri, Samuele Agostini, Marguerite Godard, Daniel Peters, et al.. Stability of antigorite serpentinite and geochemical exchange with oceanic crustal rocks during ultrahigh-pressure subduction-zone metamorphism (Lago di Cignana Unit, Italian Western Alps). *Journal of Petrology*, 2019, 60 (6), pp.1229-1262. 10.1093/petrology/egz030 . hal-02349539

HAL Id: hal-02349539

<https://hal.umontpellier.fr/hal-02349539>

Submitted on 6 Nov 2020

HAL is a multi-disciplinary open access archive for the deposit and dissemination of scientific research documents, whether they are published or not. The documents may come from teaching and research institutions in France or abroad, or from public or private research centers.

L'archive ouverte pluridisciplinaire **HAL**, est destinée au dépôt et à la diffusion de documents scientifiques de niveau recherche, publiés ou non, émanant des établissements d'enseignement et de recherche français ou étrangers, des laboratoires publics ou privés.



Draft Manuscript for Review

Stability of antigorite serpentinite and geochemical exchange with oceanic crustal rocks during ultrahigh-pressure subduction-zone metamorphism (Lago di Cignana Unit, Italian Western Alps)

Journal:	<i>Journal of Petrology</i>
Manuscript ID	Draft
Manuscript Type:	Original Manuscript
Date Submitted by the Author:	n/a
Complete List of Authors:	Gilio, Mattia; Universita degli Studi di Genova Dipartimento di Scienze della Terra dell'Ambiente e della Vita; Universita degli Studi di Pavia Dipartimento di Scienze della Terra e dell'Ambiente Scambelluri, Marco; University of Genova, Dipartimento di Scienze della Terra dell'Ambiente e della Vita Genova Agostini, Samuele; Istituto di Geoscienze e Georisorse, Consiglio Nazionale delle Ricerche (CNR), Via Moruzzi, 1, 56124 Pisa, Italy Godard, Marguerite; CNRS, Géosciences Montpellier, Université de Montpellier Peters, Daniel; University of Bern, Institute of Geological Sciences; Institut de Recherche en Astrophysique et Planetologie Pettke, Thomas; University of Bern, Institute of Geological Sciences
Keyword:	subduction, serpentinite, oceanic crust, ultrahigh-pressure metamorphism, fluid-rock exchange, element transfer, Lago di Cignana, Ti-chondrodite

SCHOLARONE™
Manuscripts

1
2
3 **1 Stability of antigorite serpentinite and geochemical exchange with oceanic crustal rocks**
4
5 **2 during ultrahigh–pressure subduction–zone metamorphism (Lago di Cignana Unit,**
6
7 **3 Italian Western Alps).**
8
9

10 4 Mattia Gilio^{1,2*}, Marco Scambelluri^{1,3}, Samuele Agostini³, Marguerite Godard⁴, Daniel
11
12 5 Peters^{5,6}, Thomas Pettke⁵
13

14
15 6 ¹Dipartimento di Scienze della Terra e dell’Ambiente e della Vita, Università degli Studi di
16
17 7 Genova, corso Europa 26, 16132 Genova, Italy
18

19
20 8 ²Dipartimento di Scienze della Terra e dell’Ambiente, Università degli Studi di Pavia, via
21
22 9 Ferrata 1, 27100 Pavia, Italy
23

24
25 10 ³Istituto di Geoscienze e Georisorse, Consiglio Nazionale delle Ricerche, via Moruzzi 1,
26
27 11 56124 Pisa, Italy
28

29
30 12 ⁴Géosciences Montpellier, Université Montpellier 2, cc60, Place Bataillon, 34095
31
32 13 Montpellier, France
33

34
35 14 ⁵Institute of Geological Sciences, University of Bern, Baltzerstrasse 3, 3012 Bern,
36
37 15 Switzerland
38

39
40 16 ⁶Institut de Recherche en Astrophysique et Planétologie, Observatoire Midi-Pyrénées, 14
41
42 17 Avenue Belin, 31400 Toulouse, France
43

44
45 18 **Keywords**
46

47
48 19 Subduction; serpentinite; oceanic crust; ultrahigh-pressure metamorphism; fluid-rock
49
50 20 exchange; element transfer; Lago di Cignana; Ti-chondrodite
51

52
53 21 **Abstract**
54
55
56
57
58
59
60

1
2
3 22 The Lago di Cignana Unit is a coesite- and diamond-bearing ophiolite recording
4
5 23 Alpine ultrahigh-pressure (UHP) metamorphism at 600 °C–3.2 GPa (~110 km depth). This
6
7 24 Unit is tectonically sandwiched between two ophiolitic slices: the eclogitic Zermatt–Saas
8
9 25 Zone (540 °C–3.2 GPa) and the blueschist Combin Zone (400 °C–0.9 GPa) along a tectonic
10
11 26 structure joining high-pressure (HP) units recording a ~1.2 GPa (40 km) pressure difference.
12
13 27 So far, the Zermatt–Saas Zone has been attributed to HP conditions and the mechanism
14
15 28 driving exhumation and accretion of the UHP Lago di Cignana Unit in its present structural
16
17 29 position is not fully understood. Here we show that the top of the Zermatt–Saas Zone consists
18
19 30 of a thin sliver of UHP serpentinites (the Cignana serpentinite), lying on top of a
20
21 31 homogeneous unit (the Zermatt serpentinite). The Zermatt and the Cignana serpentinites
22
23 32 underwent different pressure–temperature paths during the Alpine subduction history. The
24
25 33 serpentinite enveloping the UHP Lago di Cignana Unit shows a first crystallization of olivine
26
27 34 + Ti-clinohumite in rocks and veins at about 2.0 GPa and 450–500 °C. A second generation
28
29 35 of veins include Ti-chondrodite formed at higher PT conditions of about 3.0 GPa and 600–
30
31 36 650 °C, comparable to the UHP event recorded by the nearby eclogite and metasediments of
32
33 37 the Lago di Cignana Unit. Type 1 and type 2 veins are both overgrown by later stage Ti-
34
35 38 clinohumite.

39
40 39 The mineral association antigorite + olivine + Ti-clinohumite/chondrodite is thus
41
42 40 stable in serpentinites at U HP conditions in the coesite and diamond facies. Furthermore, the
43
44 41 trace element and isotopic compositions of the Cignana serpentine suggest geochemical
45
46 42 exchange with the nearby crustal rocks of the Lago di Cignana Unit. This geochemical
47
48 43 imprint is different from the one recorded by the Zermatt serpentinite, which only records
49
50 44 oceanic hydration and underwent subduction in a close system environment. This implies that
51
52 45 the UHP serpentinite enveloping Cignana was tectonically juxtaposed with the Cignana
53
54 46 crustal rocks during the prograde subduction history, exchanging fluid-mobile trace elements
55
56
57
58
59
60

1
2
3 47 and modifying its pristine oceanic isotopic signature. The crustal UHP Cignana rocks and the
4
5 48 associated UHP serpentinite were exhumed together along the major discontinuity separating
6
7 49 the Zermatt and the Combin Zones, which may represent a fossil plate interface active during
8
9 50 the exhumation stages.

51 INTRODUCTION

52 Serpentinites are considered as key rocks affecting the geochemical cycles of fluid
53 mobile elements and tectonics in subduction zones (**Spandler and Pirard, 2013; Deschamps**
54 **et al., 2013; Kendrick et al., 2017**). Due to their ability to transfer water (**Ulmer and**
55 **Trommsdorff, 1995**) and fluid mobile elements to great depths, they have been referred to as
56 'sponges' (**Deschamps et al., 2011**), whose behaviour during hydration and dehydration
57 processes controls the geochemical and physical properties of subducting slabs and overlying
58 mantle (**Reynard, 2013; Rüpke et al., 2004**). Increasing importance is now given to interface
59 domains between subducting and overlying plates, where serpentinite is part of tectonic
60 mélanges atop the slab (**Bebout, 2007; Scambelluri et al., 2014**), forms thick tectonic slices
61 detached from slabs and accreted to the plate interface (**Angiboust et al., 2014; Guillot et al.,**
62 **2015; Cannà et al., 2016**), or derives from hydration of supra-subduction mantle (**Guillot**
63 **et al., 2001; Bostock et al., 2002; Savov et al., 2005; Ryan et al., 2014**). From a geophysical
64 point of view, architecture and lithologies of the subduction plate interface are uncertain due
65 to limited resolution in geophysical screening of deep subduction environments. Several
66 models for the plate interface environment tried to integrate field/structural and
67 petrological/geochemical studies with geophysical investigations of present day subduction
68 zones (**Ranero & Sallares, 2004; Bebout, 2007; Brovarone et al., 2013; Agard et al., 2009;**
69 **Angiboust et al., 2009; 2014; Bostock, 2013**). These models suggest the plate interface is a
70 sharp contact between oceanic crust and mantle wedge, which preserves distinct lithological
71 domains, or coincides with a mechanical and metasomatic melange zone. One of these

1
2
3 72 models for deep (80 km) environments describes this plate interface as consisting of
4
5 73 decoupled slices of coherent oceanic crust and metasediments associated with thick portions
6
7 74 of serpentinized slab mantle (**Angiboust et al., 2009, 2014**). This implies complex
8
9 75 geometries with strain partitioning and deformation accumulated in 100–500 m thick
10
11 76 serpentinite shear zones enveloping less deformed bodies of oceanic crust and metasediments
12
13 77 (**Guillot et al., 2001; Angiboust et al., 2011; 2012b; 2014**). Understanding such geometries
14
15 78 and the processes involved during subduction and exhumation is vital to characterize the
16
17 79 timing of coupling–decoupling of different oceanic slices and their accretion at the plate
18
19 80 interface.

21
22 81 The interest in serpentinites increased in the mid–1990s, based on the
23
24 82 discovery of widespread ocean floor serpentinization (**Cannat et al., 1995**) and the stability
25
26 83 of antigorite to eclogite–facies conditions (**Ulmer & Trommsdorff, 1995; Scambelluri et**
27
28 84 **al., 1995; Schmidt & Poli, 1998**). This led to investigations on the role of subducted
29
30 85 serpentinized mantle in water and fluid–mobile element recycling to arc magmas
31
32 86 (**Scambelluri et al., 2004, 2014; Scambelluri & Tonarini, 2012; Deschamps et al., 2011,**
33
34 87 **2013; John et al., 2011; Kendrick et al., 2011; Debret et al., 2013a, 2013b; Cannaò et al.,**
35
36 88 **2015, 2016; Rüpke et al., 2004; Iwamori, 1998**) and its involvement in exhumation
37
38 89 tectonics (**Hermann et al., 2000; Schwartz et al., 2001**). Serpentinites are reliable tracers of
39
40 90 geochemical interactions and metasomatism in subduction zones (**Hattori et al., 2005;**
41
42 91 **Deschamps et al., 2011, 2013; Scambelluri & Tonarini, 2012; Scambelluri et al., 2015;**
43
44 92 **Cannaò et al., 2015, 2016; Lafay et al., 2013**). Serpentinites acquire their peculiar
45
46 93 geochemical (e.g. B, U/Cs, As, Sb; **Kodolányi et al., 2012; Peters et al., 2017**) and isotopic
47
48 94 (e.g. marine $^{87}\text{Sr}/^{86}\text{Sr}$, $\delta^{11}\text{B}$) characteristics during the main oceanic serpentinization event,
49
50 95 and these may variably evolve during their subduction. The study of subducted serpentinites
51
52 96 and associated oceanic crust and metasediments can be a powerful tool to reconstruct
53
54
55
56
57
58
59
60

1
2
3 97 geometry and architecture of fossil subduction systems (**Scambelluri & Tonarini, 2012;**
4
5 98 **Cannaò et al., 2015, 2016; Scambelluri et al., 2014, 2015**).

6
7 99 Serpentinized mantle can host up to 13 wt.% of water to HP and UHP depth
8
9 100 (**Ulmer & Trommsdorff, 1995**). Dehydration reactions like antigorite + brucite → olivine +
10
11 101 H₂O, and antigorite → olivine + orthopyroxene + chlorite + H₂O release substantial amounts
12
13 102 of water in subduction zones, triggering element exchange between serpentinites and adjacent
14
15 103 rocks. Although these reactions can provide reliable temperature constraints (**Sanchez–**
16
17 104 **Vizcaino et al., 2005; Scambelluri et al., 2004, 2014**), the steep slopes of dehydration
18
19 105 reactions in a pressure versus temperature plot prevent accurate pressure estimates (**Ulmer &**
20
21 106 **Trommsdorff, 1995**). To the contrary, the transition from Ti–Clinohumite to Ti–Chondrodite
22
23 107 (2.6–3.0 GPa for 500–650 °C), helps to constrain the pressure attained during high–pressure
24
25 108 (HP) metamorphism of serpentinite (**Shen et al., 2015**).

26
27
28 109 Serpentine and de-serpentinization fluid compositions help to unravel
29
30 110 element exchange and fluid–pathways in HP subduction settings. The HP ophiolites of
31
32 111 Zermatt–Saas Zone (**Figure 1**) and the associated ultrahigh–pressure (UHP) oceanic crust of
33
34 112 the Lago di Cignana Unit (**Figures 1 and 2**), are suitable locations to investigate fluid
35
36 113 exchange under UHP subduction conditions. The Zermatt–Saas Zone (ZSZ) is a slice of
37
38 114 eclogite–facies oceanic crust (**Ernst & Dal Piaz, 1978; Bucher et al., 2005; Angiboust et**
39
40 115 **al., 2009**) in contact with the continental Monte Rosa Nappe at the bottom and the
41
42 116 blueschist–facies metaophiolites of the Combin Unit at the top. The top of the ZSZ hosts
43
44 117 several tectonic slices of different ages, pressure–temperature evolution and provenance
45
46 118 (Teodulo, Etirol–Levaz, Allalin Gabbro; **Bucher & Grapes, 2009; Skora et al., 2015**). One
47
48 119 of these slices, the Lago di Cignana Unit (LCU), was subducted to more than 90 km depth
49
50 120 (3.2 GPa – 550 °C) during the Eocene and retains the highest recorded pressures amongst HP
51
52 121 ophiolites in the Alpine–Himalayan orogenic system (**Figure 1; Reinecke, 1998; Groppo et**

1
2
3 122 **al., 2009; Frezzotti et al., 2011**). As such, it represents a good proxy for studying the fluid
4
5 123 pathways and the tectonic coupling of different rock units within the plate interface during
6
7 124 UHP metamorphism.

8
9 125 There is strong debate about whether the Zermatt–Saas Zone was a coherent tectonic
10
11 126 unit during its subduction–exhumation cycle. Several structural and petrologic studies
12
13 127 suggest that this is the case, also based on original stratigraphic contacts preserved
14
15 128 (**Angiboust et al., 2009; Beltrando et al., 2010; Tartarotti et al., 2017**). Other work
16
17 129 indicates that the Zermatt–Saas Zone is a stack of different slices which followed distinct
18
19 130 subduction–exhumation paths (**Li et al., 2004; Bucher and Grapes, 2009; Groppo et al.,**
20
21 131 **2009; Rebay et al., 2012; Zanoni et al., 2016; Skora et al., 2015**). **Skora et al. (2015)**
22
23 132 evaluated and discussed Lu–Hf ages from various slices in the Zermatt–Saas Zone and
24
25 133 suggested an early subduction of the units at its structural top (50 Ma; Lago di Cignana,
26
27 134 Pfulwe, and Chamois), followed by a largely coeval peak metamorphism at around 43–39
28
29 135 Ma.

30
31
32
33 136 Classic petrologic work has reconstructed the evolution of the Zermatt Saas Zone
34
35 137 from basaltic eclogites, often ignoring (for a lack of viable geobarometers) the tectonic
36
37 138 history and PT evolution of the surrounding serpentinites. Using simple thermodynamic
38
39 139 modelling on Zermatt serpentinites directly underlying the Lago di Cignana Unit, **Rebay et**
40
41 140 **al. (2012)** reports peak estimates up to 2.7 GPa. Following these results, **Zanoni et al. (2016)**
42
43 141 suggested that such PT estimates may point to a domain of UHP conditions. Nonetheless, PT
44
45 142 estimates on basaltic eclogites suggest the Zermatt–Saas zone was equilibrated at an overall
46
47 143 lower P (**Angiboust et al., 2009**). Furthermore, it has remained unclear whether an antigorite
48
49 144 + olivine + Ti-clinohumite system will survive UHP conditions ($P \geq 3.0$ GPa), because this
50
51 145 assemblage was never found in natural sample but only observed in experimental work
52
53
54
55 146 (**Ulmer and Trommsdorff, 1995**).

1
2
3 147 In this work, we sampled serpentinites at increasing distance from the UHP Lago di
4
5 148 Cignana Unit (**Figure 2**) to test whether the transition from the UHP Cignana Unit to the
6
7 149 surrounding serpentinite is accompanied by a change in PT conditions recorded by
8
9 150 serpentinites and/or by a change in their trace element (TE) and isotopic (Sr and Pb)
10
11 151 composition. Our goal is to compare the geochemical and isotopic imprint of the ZSZ and the
12
13 152 Cignana serpentinites, verify whether element exchange occurred between the crustal UHP
14
15 153 Cignana rocks and the surroundings serpentinites and if so, at which conditions it took place.
16
17 154 This will shed light on the nature and behaviour of the plate interface during the Alpine
18
19 155 subduction cycle.
20
21
22

23 156 **GEOLOGIC AND PETROLOGIC BACKGROUND**

24
25 157 The Piemonte Ophiolite Nappe is the remnant of the Mesozoic Piemontese ocean,
26
27 158 subducted and incorporated into the Alpine orogen. In the Valtournenche area (Aosta Valley,
28
29 159 Italy), the Piemonte Ophiolite Nappe consists of a pile of tectonic slivers commonly divided
30
31 160 into Combin Zone on top, and Zermatt–Saas Zone at the bottom (**Bearth, 1967**). The high–
32
33 161 pressure ophiolite units from Valtournenche and Aosta Valley are overlain by the continental
34
35 162 Dent Blanche klippe (blueschist–facies) and Sesia-Lanzo (eclogite–facies) units. The Combin
36
37 163 Unit represents the sedimentary transition between the Piemonte ocean and the European
38
39 164 continental margin (**Figure 1**). It consists of metamorphic conglomerates, quartzites,
40
41 165 dolostones, and sedimentary breccias, containing slices of serpentinized mantle peridotite
42
43 166 equilibrated in epidote–blueschist facies during the Eocene (300–450 °C and ~0.9 GPa; ~44
44
45 167 Ma; **Reddy et al., 1999**).
46
47
48

49 168 The Zermatt–Saas Zone represents a subducted remnant of the Mesozoic
50
51 169 Tethys. It consists of: (1) serpentinized mantle peridotite (**Li et al., 2004; Rebay et al.,**
52
53 170 **2012**), (2) portions of oceanic crust (Fe–Ti and Mg–Al gabbros and metabasalts) strongly re–
54
55 171 equilibrated in eclogite, blueschists and greenschists facies (**Bucher et al., 2005**) and
56
57
58
59
60

1
2
3 172 subordinate oceanic metasediments (Mn-rich quartzites, calc-schists and marbles; **Bearth &**
4
5 173 **Schwander, 1981**). Previous work on Zermatt serpentinite, performed by **Rebay et al. (2012)**
6
7 174 and **Zanoni et al. (2012)** showed that this area underwent a complex tectonic and
8
9 175 metamorphic history, from oceanic hydration to Alpine subduction. The authors distinguished
10
11 176 three main deformation events, related to deformation-induced recrystallization of antigorite
12
13 177 and metamorphic olivine during the prograde (D1), peak (D2), and retrograde (D3)
14
15 178 metamorphic event. D1 develops an antigorite foliation (S1). Olivine + Ti-clinohumite +
16
17 179 magnetite veins cut the S1 foliation and are, in turn, deformed and stretched along an olivine-
18
19 180 bearing foliation (S2). Late crenulation (D3) and open folding deforms the pervasive HP S2
20
21 181 foliation and develops a weak, antigorite + chlorite foliation (S3). Zircon crystals associated
22
23 182 with the HP S2 foliation in serpentinite gave an age of about 65.5 Ma (**Rebay et al., 2017**).

24
25
26 183 The central section of the ZSZ shows concordant metamorphic peak
27
28 184 conditions (540 ± 20 °C and 2.3 ± 0.1 GPa; **Figure 3; Angiboust et al., 2009**) and ages (41-
29
30 185 38 Ma, **Skora et al., 2015**). To the contrary, the top-section of the ZSZ, in contact with the
31
32 186 Combin Unit, shows greater complexity. Here, oceanic and continental slices of different
33
34 187 provenance, PT histories, and metamorphic ages occur within olivine- and Ti-clinohumite-
35
36 188 bearing serpentinites (Etirol-Levaz, **Beltrando et al., 2010; Pfulwe, Skora et al., 2015;**
37
38 189 Allalin Gabbro, **Bucher & Grapes, 2009**; Teodulo Glacier Unit, **Weber & Bucher, 2015;**
39
40 190 Lago di Cignana Unit, **Groppo et al., 2009; Frezzotti et al., 2011; Reinecke, 1998**). One of
41
42 191 these slices of metasediments and eclogites, the Lago di Cignana Unit (LCU), crops out to the
43
44 192 South of the Cignana artificial lake, SW of the dam. The Lago di Cignana Unit is a small
45
46 193 slice of MORB-type oceanic crust covered by oceanic sediments tectonically sandwiched
47
48 194 between the lower ZSZ and the overlying Combin and Dent Blanche Units. The peculiar
49
50 195 feature of the Cignana crustal section is that it equilibrated under ultrahigh-pressure (UHP)
51
52 196 conditions during the alpine event (600 °C – 3.2 GPa; **Figure 3; Groppo et al., 2009;**
53
54
55
56
57
58
59
60

1
2
3 197 **Reinecke, 1998**), witnessed by the presence of coesite inclusions in mafic rocks and
4
5 198 metasediments and of microdiamonds in meta-sedimentary rocks (**Reinecke, 1991, 1998;**
6
7 199 **Frezzotti et al., 2011**). Pressure estimates of up to 3.6 GPa derive from microdiamond
8
9 200 occurrence (**Frezzotti et al., 2011**). U–Pb zircon ages of Cignana eclogite yield an average of
10
11 201 44.1 ± 0.7 Ma, interpreted to date the peak subduction event (**Rubatto et al., 1998**). Rb–Sr
12
13 202 cooling ages on white mica in Cignana metasediments indicate rapid exhumation at ~ 38 Ma
14
15 203 (**Amato et al., 1999**). Several authors (**Forster et al., 2004; Groppo et al., 2009; Reinecke,**
16
17 204 **1998**) consider these serpentinites to be part of the underlying, lower pressure, Zermatt–Saas
18
19 205 Zone.

206 ANALYTICAL METHODS

207 Bulk rock major element concentrations were measured either by XRF at the
208 Activation Laboratories in Toronto, Canada, or by the laser-ablation ICP–MS pressed
209 powder pellet (LA–ICP–MS PPP) technique at the University of Bern, Switzerland (**Peters &**
210 **Pettke, 2017**). Trace element measurements were done either by liquid–mode ICP–MS at the
211 University of Montpellier, France, or by LA–ICP–PPP at the University of Bern, Switzerland.
212 Data are reported in **Table 2**.

213 Liquid mode ICP–MS followed the procedures described in **Ionov et al. (1992)** and in
214 **Godard et al. (2000)**. 100 mg powdered sample aliquots were dissolved in a HF/HClO₄
215 mixture in screw-top Teflon beakers and then diluted for measurement by a factor of 1000,
216 2000, and 4000 for ultramafic, mafic, and silicic rocks, respectively, using an Agilent 7700X
217 quadrupole ICP–MS. External calibration solutions employed were multi–element standard
218 solutions (Merck) except for Nb and Ta, and In and Bi were used as internal standards. To
219 avoid memory effects due to the introduction of concentrations Nb–Ta solutions in the
220 instrument, Nb and Ta concentrations were determined by using, respectively, Zr and Hf as
221 internal standards. This surrogate calibration technique is adapted from the method described

1
2
3 222 by **Jochum et al. (1990)** for the determination of Nb by spark–source mass spectrometry.
4
5 223 Scandium, V, Mn, Co, Ni, Cu, Zn, and As were measured in helium cell gas mode, in order to
6
7 224 reduce polyatomic interferences. Reproducibility and accuracy of analyses were monitored
8
9 225 by measuring, as unknowns, the standards BHVO-1, BE-N and OU6 (used for trace–element
10
11 226 rich rocks, like gneiss, micaschist and black-wall), UB-N, BIR-1 and MRG1 (for intermediate
12
13 227 mafic rocks), and JP-1 and DTS-1 (for depleted chlorite harzburgite).

14
15
16 228 Bulk rock measurements performed by LA–ICP–MS PPP follow the procedures
17
18 229 documented in detail by **Peters & Pettke (2017)**. The sample processing procedure
19
20 230 comprised the following steps: (1) dry milling of crushed rock powder and (2) subsequent
21
22 231 wet milling of ~2.2 g of rock powder in 5.6 g of high purity water, all in agate milling
23
24 232 equipment using a Retsch PM 100 planetary ball mill, to obtaining an average powder grain
25
26 233 size a few μm . (3) The sample suspension is then dried down on a hot plate under a fume
27
28 234 hood at 70 °C. (4) The production of the pressed powder pellets involves homogenisation of
29
30 235 the dried powder and mixing by hand of 120 mg rock powder with 30 mg of microcrystalline
31
32 236 cellulose as binder using a small agate mortar and pestle, and then pressing robust pellets in a
33
34 237 manual hydraulic press at 500 MPa using an in–house built steel apparatus. The resulting
35
36 238 pellets were measured at 6 spots each with a laser beam size of 120 μm , an energy density of
37
38 239 5 J/cm² at a repetition rate of 10 Hz, and calibrated by bracketing standardisation employing
39
40 240 the United State Geological Survey (USGS) basalt glass GSD–1G. LA–ICP–MS
41
42 241 measurements were done using a Geolas Pro 193 nm ArF excimer laser coupled with an Elan
43
44 242 DRC–e ICP–MS at the University of Bern, Switzerland. Instrument optimisation procedures
45
46 243 followed those detailed in **Pettke et al. (2012)**. Data reduction employed SILLS (**Guillong et**
47
48 244 **al., 2008**), and 100 wt.% minus LOI (wt.%) was used as the internal standard for
49
50 245 quantification. Due to lack of data on Fe³⁺/Fe²⁺, total iron was calculated as FeO. Analytical
51
52 246 accuracy was monitored by measurement of BCR–2G standard as PPP, and data correspond
53
54
55
56
57
58
59
60

1
2
3 247 to the long-term averages reported in **Peters & Pettke (2017)** except for Be and Cd, for
4
5 248 which measurements near the respective limits of detection can produce strong overestimates
6
7 249 (Peters and Pettke, 2017).
8

9 250 Isotope ratio measurements were performed using a Finnigan MAT 262 multiple
10
11 251 collector thermal ionisation mass spectrometer (TIMS) at IGG-CNR of Pisa (Italy). For Pb,
12
13 252 the instrument was operated in static mode. Lead fractions were purified with conventional
14
15 253 ion chromatography using Dowex AG1-X8 anion resin, using standard HBr and HCl elution
16
17 254 procedures. Lead was loaded on single Re (99.999% pure) filaments with TEOS solution and
18
19 255 measured at a pyrometer-controlled temperature of 1310 °C. Replicate analyses of Pb
20
21 256 standard SRM981 yielded isotope ratios are accurate to within 0.025% (2SD) per mass unit,
22
23 257 after applying a mass bias correction of 0.15±0.01% per mass unit relative to the NIST SRM
24
25 258 981 reference composition of **Todt et al. (1996)**. Lead blanks were of the order of 0.2 – 0.4
26
27 259 ng during the period of chemistry processing; hence, no blank correction was made.
28
29 260 Strontium isotope ratio measurements were performed in dynamic mode. Strontium fractions
30
31 261 were purified using the Sr-spec ion exchange resin. Instrumental mass bias correction was
32
33 262 done by internal normalisation to $^{86}\text{Sr}/^{88}\text{Sr} = 0.1194$. Replicate measurements of NIST SRM
34
35 263 987 (SrCO_3) standard gave an average value of 0.710207 ± 13 (2SD, $n = 47$). Our data were
36
37 264 adjusted to $^{87}\text{Sr}/^{86}\text{Sr} = 0.710250$. Throughout the full chemical process, the Sr blanks were
38
39 265 approximately 0.3 ng, which are negligible for the analysed samples (0.3–0.5 g of sample,
40
41 266 depending on Sr content). Lead and Sr isotope ratios are reported with age correction (40 Ma;
42
43 267 **Rubatto et al., 1998**) using U, Th, Pb, Rb, and Sr concentrations obtained from liquid mode
44
45 268 ICP-MS measurements, respectively.
46
47
48
49

50 269 In-situ major element (SiO_2 , TiO_2 , Al_2O_3 , Cr_2O_3 , FeO , MgO , MnO , CaO , NiO , Na_2O ,
51
52 270 and K_2O) compositions of minerals (Table 2–6) were measured using a JEOL JXA 8200
53
54 271 Superprobe equipped with five wavelengths-dispersive (WDS) spectrometers, an energy
55
56
57
58
59
60

1
2
3 272 dispersive (EDS) spectrometer, and a cathodoluminescence detector (accelerating potential
4
5 273 15 kV, beam current 15nA), operating at the Dipartimento di Scienze della Terra, University
6
7 274 of Milano. The measurements of all elements were performed with a 30-second counting
8
9 275 time. Results with total oxide percentage lower than 98% and higher than 102% were
10
11 276 immediately discarded from the data set. A second measurement quality check was done
12
13 277 based on atoms per formula unit, discarding measurements that showed more than 0.5%
14
15 278 deviation from the stoichiometric composition.

17 18 279 **RESULTS**

19 20 280 **Petrography and microstructures**

21
22
23 281 Samples were collected along a profile from the internal part of the Zermatt–Saas
24
25 282 Zone into the LCU UHP unit, localised in Figure 2 and reported in Table 1. Tectonic units
26
27 283 sampled include (1) the serpentinites from the Zermatt Saas Zone, in the area described in
28
29 284 **Rebay et al. (2012)**, (2) the Lago di Cignana Unit (basaltic eclogites and metasediments),
30
31 285 and (3) the serpentinites directly in contact with the UHP Lago di Cignana Unit referred to
32
33 286 here as Cignana serpentinites; serpentinites and Ti–chondrodite/clinohumite veins).

34 35 36 287 *Zermatt–Saas Zone Serpentinite*

37
38
39 288 Zermatt–Saas Zone serpentinites crop out in a structurally lower area with respect to
40
41 289 the LCU (**Figure 2**). Three samples of Zermatt serpentinite (ZSG1405, ZSG1406, ZSG1410)
42
43 290 from the area described in **Rebay et al. (2012)** were investigated in detail. The Zermatt
44
45 291 serpentinite displays a well-developed antigorite (Atg) + olivine (Ol) + diopside (Di) ±
46
47 292 magnetite (Mag) foliation (S₂) parallel to boudinaged rodingite dykes and wrapping around
48
49 293 less deformed serpentinite domains. This foliation and the less deformed serpentinite include
50
51 294 pre-kinematic clasts of mantle clinopyroxene (Cpx), bastites after mantle pyroxene, and
52
53 295 mesh structures (serpentine + magnetite) after mantle olivine (**Figure 4a–b**). Metamorphic
54
55
56
57
58
59
60

1
2
3 296 diopside aggregates are stretched along the main foliation or grow around mantle
4
5 297 clinopyroxene porphyroclasts. Sample ZSG1406 contains fragments of olivine + Ti-
6
7 298 clinohumite (Ti-Chu) veins, locally showing tiny Ti-chondrodite (Ti-Chn) relict grains
8
9 299 (**Figure 4c**).

10
11
12 300 *Lago di Cignana eclogite and metasediments*
13

14
15 301 The five metasediment samples comprise metaquartzite (LCG1414 and LCG1415),
16
17 302 meta-calcschist (LCG1416A and LCG1416B), and marble (LCG1501), in addition to one
18
19 303 basaltic eclogite (LCG1401; **Table 1**).

20
21
22 304 The basaltic eclogite (**Figure 5a**) consists of garnet (Grt), omphacite (Omp), phengite
23
24 305 (Ph), and rutile (Rt). Garnet shows inclusion-rich cores, mostly coesite (Coe), quartz (Qz)
25
26 306 phengite, zircon (Zrn), rutile, and apatite (Ap), and inclusion-poor rims. Omphacite occurs as
27
28 307 large (mm-sized) crystals, generally zoned from core to rim. Eclogite shows various degrees
29
30 308 of re-equilibration along weak foliations defined by blue- and/or green-schist facies
31
32 309 minerals, mostly glaucophane (Gln) after omphacite, chlorite (Chl) and barroisite (Brs) after
33
34 310 garnet. Amongst collected eclogites, sample LCG1401 (**Figure 5a**) show the weakest
35
36 311 retrograde overprint (<5%).
37
38
39

40 312 The Cignana metasediments consist of (1) impure, locally Mn-rich, quartzite
41
42 313 (LCG1415, **Figure 5b-c-d**), (2) garnet calcschists (LCG1416A and LCG1416B, **Figure 5e-**
43
44 314 **f**), and (3) garnet-bearing impure marbles (LCG1501). Quartzite has poikiloblastic garnet
45
46 315 and tourmaline (Tur) with inclusions of coesite (optically identified, now mostly quartz),
47
48 316 phengite/piemontite, apatite, and rutile. Mn-quartzite contains garnet, phengite, piemontite
49
50 317 (Pmt), pseudomorphs after lawsonite (Lws), and epidote (Ep) with an allanite (Aln) core
51
52 318 (**Figure 5c-d**). Mn-garnet occurs within layers and close-packed nodules of 50–300 µm-
53
54 319 sized crystals and often contains coesite inclusions (**Figure 5d**). Quartzite locally hosts large
55
56
57
58
59
60

1
2
3 320 (1–2 mm) garnet poikiloblasts and zoned tourmaline (LCG1415). Oriented phengite (3T
4
5 321 polytype; **Groppo et al., 2009**) defines the foliation in quartzites. Exhumation–related quartz
6
7 322 sub–grain growth along with undulous extinction suggests that all quartz recrystallized from
8
9 323 original UHP coesite during exhumation. Quartzites are partially retrogressed to epidote–
10
11 324 greenschist facies: albite (Ab) replaces phengite, albite and muscovite (Ms) replace
12
13 325 lawsonite, and chlorite and barroisite replace garnet. Calcschist (LCG1416A and LCG1416B)
14
15 326 and impure marble (LCG1501) contain calcite (Cal), quartz, poikiloblastic garnet, epidote,
16
17 327 phengite, and rare paragonite (**Figure 5e–f**). Typical inclusions in garnet are calcite, apatite,
18
19 328 rutile, coesite, and white mica. The UHP eclogitic assemblage is rarely preserved in
20
21 329 calcschists. Garnet is partially chloritized at rims and late iron hydroxides replace HP mica
22
23 330 and epidote.

27 331 *Cignana Serpentinites*

28
29
30 332 A serpentinite body, 1km long and 100m thick, crops out 200m to the West of the
31
32 333 Southern section of the Lago di Cignana Unit (**Figure 2**). The Cignana serpentinite shows an
33
34 334 antigorite + olivine–bearing HP foliation deforming rodingite dykes comparable to the S2
35
36 335 foliation described for the underlying Zermatt serpentinites (**Rebay et al., 2012**). In Cignana,
37
38 336 widespread Ti–rich metamorphic veins cross–cut the olivine–bearing foliation and are, in
39
40 337 turn, crenulated by later deformation events. We investigated four serpentinite samples
41
42 338 (ZSG1403, ZSG1502S, ZSG1507S and ZSG1510), and three veins (ZSG1402, ZSG1502V,
43
44 339 ZSG1507).

45
46
47 340 The serpentinite foliation is defined by elongated domains of HP metamorphic
48
49 341 olivine, metamorphic diopside, and magnetite embedded in antigorite (**Figure 4d**). Chlorite
50
51 342 aggregates with magnetite cores are stretched along the main foliation. Two types of veins
52
53 343 cut the Cignana serpentinite: one dominated by Ti–clinohumite (type 1) and another contains
54
55 344 Ti–chondrodite (type 2). Type 1 veins host 3–5 mm Ti–clinohumite crystals, olivine, chlorite,

1
2
3 345 magnetite, and rare diopside (**Figure 4e**). Type 2 veins are 1–3 cm thick and up to 20 cm
4
5 346 long, characterised by the occurrence of primary Ti–chondrodite. Type 2 veins consist of Ti–
6
7 347 chondrodite, chlorite, olivine, apatite, and diopside (**Figure 4f–g**) and display a
8
9 348 compositional banding consisting in 5–10mm thick chlorite–rich rims and Ti–chondrodite–
10
11 349 rich cores. Ti–chondrodite occurs as 0.5–1 mm–sized, isolated crystals, filled with inclusions
12
13 350 of ilmenite (Ilm), zircon and REE–bearing phases (**Figure 4f**). The Ti–chondrodite vein
14
15 351 crystals display corroded rims which recrystallize into 50–500 μm –sized, inclusion–free, Ti–
16
17 352 clinohumite neoblasts (**Figure 4f**). Olivine generally occurs as relics, partially replaced by
18
19 353 Ti–clinohumite. In type 2 veins, chlorite occurs as idiomorphic, inclusion–free crystals
20
21 354 (**Figure 4f**), and apatite occurs as mm–sized aggregates of solid and fluid inclusions–rich
22
23 355 crystals (**Figure 4g**). Vein diopside occurs as sub–mm fibres bordering the Ti–clinohumite–
24
25 356 rich bands (**Figure 4h**). Elongated fluid inclusions (Flincs) occur parallel to the diopside
26
27 357 elongation axis. Such diopside fibres extensively recrystallized into finer–grained, inclusion–
28
29 358 free diopside crystals (**Figure 4h**). The type 2 Ti–chondrodite–bearing veins contain no relics
30
31 359 of potential igneous minerals, like aphyric clinopyroxene or ilmenite, which might hint to a
32
33 360 Fe–Ti gabbroic protolith for these bodies (i.e. **Scambelluri & Rampone, 1999**).

34
35
36
37 361 Type 1 and type 2 veins are deformed by an olivine–bearing antigorite foliation and
38
39 362 are crenulated during a later–stage deformation event. Crenulations display an olivine–free,
40
41 363 antigorite axial plane foliation. In both type 1 and type 2 veins, the original mineralogy
42
43 364 recrystallized into finer–grained (<1 mm), inclusion–free, Ti–clinohumite (2), chlorite (2),
44
45 365 and diopside (2).

366 **Bulk–rock compositions**

367
368 The major and trace element and isotopic bulk compositions of metasediments, meta–
369 Zone are reported in **Tables 2 and 3** and illustrated in **Figures 6, 7, 8, 9 and 10**.

1
2
3 370 *Major elements*
4

5
6 371 The Zermatt–Saas Zone serpentinite displays a rather homogeneous harzburgitic
7
8 372 composition (except for higher FeO content of sample ZSG1406), but with much lower Al₂O₃
9
10 373 (~1.5–1.7 wt.%) and CaO (~0.5%) content than Cignana serpentinites (**Figure 6a–b**).

11
12
13 374 The Cignana basaltic eclogite (LCG1501) is a typical oceanic Fe–Ti gabbro, has
14
15 375 Al₂O₃ ~ 15.8%, TiO₂ ~ 2.5% and low L.O.I content (0.4%), compatible with an altered
16
17 376 oceanic Fe–Ti gabbro protolith, as suggested by **Groppo et al. (2009)**. The Cignana
18
19 377 metasediments include several lithological subtypes with varying silica and CO₂ contents.
20
21 378 The most abundant varieties include Qz–micaschists with Mn–rich layers and calcschists.
22
23 379 Qz–micaschists have a SiO₂ content >70% and Al₂O₃ of 7–12%; their compositional
24
25 380 variability includes high MnO (~ 3.7%; sample LCG1414) and high B (360 µg/g; sample
26
27 381 LCG1415) concentrations. Centimetre to m–sized layers of calcschist (CaO ~ 20–30%,
28
29 382 L.O.I. ~ 20–30%; LCG1416A and LCG1416B) and silicate–bearings marbles (CaO ~ 30%,
30
31 383 L.O.I. ~ 35%; LCG1501) reflect local variability in carbonate content.
32
33
34

35 384 The Cignana serpentinite displays a harzburgitic to lherzolitic composition with Al₂O₃
36
37 385 ~ 2.5–4.5% and CaO from ~ 2–4% up to 11.6% (this latter value reflects the exceptionally
38
39 386 high diopside modal composition of sample ZSG1507S of about 40 vol.%; **Figure 6a–b**). Ti–
40
41 387 clinohumite veins enclosed in Cignana serpentinites display variable major element
42
43 388 compositions, especially for their FeO (~7–15%) and CaO (~3–9%) content. This difference
44
45 389 reflects their relative abundance in magnetite, diopside, olivine, and Ti–clinohumite. The Ti–
46
47 390 chondrodite vein has a major element (FeO, MgO, CaO, and Al₂O₃; **Figure 6a–b**) and Cr–Ni
48
49 391 (**Figure 7**) composition comparable to mantle peridotites, Cignana serpentinite, and the Ti–
50
51 392 clinohumite veins.
52
53

54
55 393 *Trace elements*
56
57
58
59
60

1
2
3 394 *Zermatt Serpentinite*. The Zermatt serpentinite displays rather depleted TE and REE
4
5 395 patterns (**Figures 8 and 9**; C1 chondrite and PM from **McDonough & Sun, 1995**). Rare
6
7 396 earth elements (REE) decrease from heavy to light and show a variably small negative Eu
8
9 397 anomaly (**Figure 8**). All samples display comparable PM-normalized TE patterns, with
10
11 398 notable enrichments in B, Bi, W, Mo, As, and Sb with respect to the mantle depletion trend
12
13 399 (**Figure 9**).

14
15
16 400 *LCU crustal rocks*. The Cignana eclogite has a flat REE and TE pattern (**Figures 8**
17
18 401 **and 9**). Except for a slight depletion in Cs, Rb, Ba, and K, all other TE are equally enriched,
19
20 402 between 10 and 30 times the primitive mantle. The Cignana metasediments have
21
22 403 homogeneous REE patterns, showing steady decrease from light to heavy REE (**Figure 8**).
23
24 404 All samples display a weak negative Eu anomaly, absent in the eclogite sample. The TE
25
26 405 patterns show positive peaks in Cs, Rb, Pb, As, and Sb and negative peaks in Cd and Ti
27
28 406 (**Figure 9**). Quartzites and calcschists show similar trends, except for Pb and Sr, up to one
29
30 407 order of magnitude higher in calcschists, and for As and Sb, generally higher in quartzites.
31
32 408 The remarkably high B content (365 µg/g) of sample LCG1415 reflects the presence of
33
34 409 tourmaline.

35
36
37
38 410 *Cignana Serpentinite*. The Cignana serpentinite shows rather flat REE patterns, with
39
40 411 values ranging between 1 and 10 C1 chondrite composition (**Figure 8**). The TE patterns
41
42 412 scatter, showing positive anomalies for several fluid mobile elements (**Figure 9**). Noticeably,
43
44 413 As and Sb values are very variable, ranging from PM values (ZSG1510; 0.07 and 0.01 µg/g)
45
46 414 up to values two orders of magnitude higher (sample ZSG1502S, 1.82 and 0.3 µg/g).
47
48 415 Moreover, the Cignana serpentinite displays (strong) enrichments in B, Bi, W, As, Sb, Sr and
49
50 416 Th. The TE patterns of Ti-clinohumite veins hosted by the Cignana serpentinites closely
51
52 417 resemble that of the host Cignana serpentinite, except for increased Nb, Ta, and Ti contents.
53
54 418 The type 2 Ti-chondrodite vein (ZSG1402) is, instead, extremely enriched in all REE and
55
56
57
58
59
60

1
2
3 419 most TE (especially Nb, Ta, Th, U), by up to 2 orders of magnitude relative to the host
4
5 420 serpentinites. Type 2 vein displays a light-REE pattern comparable with metasediments and a
6
7 421 slightly enriched heavy-REE pattern, most comparable with eclogite. Elements such as Cs,
8
9 422 Rb, Ba, B, Cd, Pb, As, Sb, Sr, Ga, and Li display values comparable with those of Cignana
10
11 423 serpentinites.

14 424 *Isotopic Compositions*

17 425 Selected samples from the Lago di Cignana Unit and from the Cignana and Zermatt
18
19 426 serpentinites were analysed for their Pb and Sr isotopic compositions. All results, corrected
20
21 427 for an age of 40 Ma, are shown in **Table 3** and displayed in **Figure 10**. The Zermatt
22
23 428 serpentinite shows non-radiogenic Pb isotopic values (lower than DM values) for all three
24
25 429 isotopic systems ($^{206}\text{Pb}/^{204}\text{Pb}$, $^{207}\text{Pb}/^{204}\text{Pb}$, and $^{208}\text{Pb}/^{204}\text{Pb}$ are 16.887–17.731, 14.841–15.548,
26
27 430 and 35.776–37.555, respectively) and $^{87}\text{Sr}/^{86}\text{Sr} = 0.707051$, typical for Jurassic seawater
28
29 431 serpentinization (**Jones & Jenkyns, 2001**; **Vils et al., 2009**; **Cannaò et al., 2016**). The
30
31 432 Cignana eclogite shows typical isotopic composition for MORB (Kelemen et al., 2014), with
32
33 433 $^{206}\text{Pb}/^{204}\text{Pb}$, $^{207}\text{Pb}/^{204}\text{Pb}$, and $^{208}\text{Pb}/^{204}\text{Pb}$ being 18.547, 15.518, and 37.986, respectively and
34
35 434 $^{87}\text{Sr}/^{86}\text{Sr} = 0.703764$. The Cignana metasediments (quartzite and calcschist) show similar
36
37 435 values as GLOSS-II (**Plank, 2014**); $^{206}\text{Pb}/^{204}\text{Pb}$, $^{207}\text{Pb}/^{204}\text{Pb}$, and $^{208}\text{Pb}/^{204}\text{Pb}$ are between
38
39 436 18.636–18.706, 15.642–15.652, and 38.719–38.881, respectively and $^{87}\text{Sr}/^{86}\text{Sr}$ is between
40
41 437 0.709368 and 0.711573. The Cignana serpentinite has Pb and Sr isotope values between DM
42
43 438 and MORB values ($^{206}\text{Pb}/^{204}\text{Pb}$, $^{207}\text{Pb}/^{204}\text{Pb}$, and $^{208}\text{Pb}/^{204}\text{Pb}$ are 18.172–18.341, 15.402–
44
45 439 15.596, and 37.692–38.129, respectively. $^{87}\text{Sr}/^{86}\text{Sr}$ are 0.703883–0.704160, lower values than
46
47 440 Jurassic seawater (**Jones & Jenkyns, 2001**) and like MORB (**Kelemen et al., 2014**) and the
48
49 441 Cignana eclogite. Ti-bearing veins in serpentinites retain similar $^{87}\text{Sr}/^{86}\text{Sr}$, and close to
50
51 442 MORB values (0.704221 in Ti-chondrodite vein and 0.704059 in Ti-clinohumite vein). The
52
53 443 Ti-clinohumite vein has Pb isotopic compositions comparable with the host serpentinite. To
54
55
56
57
58
59
60

1
2
3 444 the contrary, the Ti–chondrodite vein is quite enriched in radiogenic lead, having values over
4
5 445 the range reported for reservoirs around the Lago di Cignana Unit (eclogite and
6
7 446 metasediments).
8
9

10 447 **Mineral compositions**

11 12 448 *Major elements*

13
14
15 449 We performed electron probe measurements on rock–forming minerals of the Cignana
16
17 450 eclogite and metasediments, on the Cignana serpentinites and their Ti–clinohumite and Ti–
18
19 451 chondrodite veins, and on the Zermatt serpentinites. Representative mineral data are reported
20
21 452 in **Tables 4-9**; the full dataset is shown in the **repository data**. Cignana eclogite consists of
22
23 453 garnet, omphacite and rutile. Garnet is of almandine–grossular composition and has Fe-rich
24
25 454 cores (Alm ~ 56–57% and Prp ~ 7%) and Mg contents increase towards the rims (Alm ~
26
27 455 50–51% and Prp ~ 8–9%). Jadeite content in omphacite increases from ~ 50% in the core to
28
29 456 ~ 70% in the rim. Epidote occurs as small inclusions within garnet cores and has ~ 50%
30
31 457 clinzoisite component. In the Cignana quartzite, garnet is almandine–grossular and has Ca–
32
33 458 rich cores (Alm ~ 50–53%, Grs ~ 27–28%, Sps ~ 10–11% and Prp ~ 4%) and Fe(II) content
34
35 459 increases towards the rims (Alm ~ 69–70%, Grs ~ 10–11%, Sps ~ 1–2% and Prp ~ 16–
36
37 460 17%). Tourmalines are dravites, with schorl contents increasing from cores (~ 18–19%) to
38
39 461 rims (~ 30–31%). Mn–rich layers in quartzites consists of quartz, Mn–rich (sps > 70%)
40
41 462 garnet, phengite, and epidote (allanite cores and clinzoisite ~ 30% towards the rims). In the
42
43 463 Zermatt serpentinites antigorite (**Figure 11a**) has low Al contents (~0.05–0.09 a.p.f.u.) and
44
45 464 high Mg# (~0.97–0.98); Olivine (**Figure 11b**) has low NiO₂ contents (~0.05–0.1%) and
46
47 465 Mg# (~0.96–0.98) comparable with associated antigorite, and Ti–chondrodite and Ti–
48
49 466 clinohumite have different compositions with respect to Cignana serpentinites, presenting
50
51 467 lower Ti contents and higher Fe(II) + Mg (**Figure 12a–b**). The Cignana serpentinites and the
52
53
54
55
56
57
58
59
60

1
2
3 468 Ti-clinohumite/chondrodite veins have similar mineralogy (despite changes in modal
4
5 469 amounts of the single phases) and consist of antigorite, chlorite, olivine, diopside, magnetite,
6
7 470 and Ti-clinohumite. Antigorite (**Figure 11a**) has Mg#~0.86–0.88 and variable Al contents
8
9 471 (0.9–0.15 a.p.f.u.). Olivine (**Figure 11b**) shows similar compositions both in the serpentinites
10
11 472 and in the Ti-clinohumite veins, having Mg#~0.84–0.88 and variable NiO₂ contents (~0.15–
12
13 473 0.5%). Similarly, Ti-clinohumite (**Figure 12a**) has similar compositions both in Ti-
14
15 474 clinohumite and in Ti-chondrodite veins (Ti~0.3–0.5 a.p.f.u.).

475 *Trace elements*

476 The full LA-ICP-MS mineral trace element dataset for the Cignana eclogite and
477 metasediments and the Cignana and Zermatt serpentinites and Ti-clinohumite veins is
478 reported in the **repository data**. Representative analyses are shown in **Tables 10-13** and
479 plotted in **Figure 13**. Antigorite (**Figure 13**) displays rather similar TE and REE patterns,
480 both in Cignana and Zermatt serpentinites. REE are depleted (0.01 to 0.1 C1 chondrite) and
481 show a slight increase from light to heavy REE. Cignana serpentines are slightly more
482 enriched in light REEs. Cignana serpentines show enrichment in Th, Be, Ta, La and Ce.
483 Conversely, Zermatt serpentines have higher B, As, and Sb. In the Cignana serpentinite,
484 olivine is depleted in light-REE and enriched in heavy REEs, B, Sb, and Li (**Figure 13**).
485 While the major element composition of diopside from the Zermatt and Cignana serpentinite
486 is similar, its REE and TE compositions differ (**Figure 13**). The Cignana diopside is enriched
487 in REE (~5–10 times the C1 chondrite), while in the Zermatt serpentinite, diopside is
488 depleted in REE, showing a slight negative Eu anomaly. Besides REE's, the Cignana
489 diopside is enriched in Rb, U, Th, Be, Ce, Pb, and Sr. Conversely, Zermatt diopside contains
490 considerable amounts of W, B, As, and Sb. Ti-clinohumite (**Figure 13**) has generally similar
491 patterns in all Cignana lithologies. Ti-clinohumite is enriched in Nb, Ta, B, W, As, Sb, and

1
2
3 492 REE. To the contrary, Ti-clinohumite in Zermatt serpentinite has more depleted trends, with
4
5 493 lower levels of REE, Nb, and Ta.
6

7 494 **DISCUSSION**

8 495 **PT evolution of the Cignana serpentinite**

9
10
11
12
13 496 The Lago di Cignana Unit consists of oceanic crustal rocks such as eclogites and
14
15 497 metasediments which underwent a complex Alpine subduction history to UHP metamorphic
16
17 498 conditions. Prograde zoning in garnet, omphacite and white mica, observed in both
18
19 499 metasedimentary rocks and metagabbros, records subduction to UHP depth along a cold
20
21 500 geothermal gradient (~ 7 °C/km; **Amato et al., 1999; Groppo et al., 2009; Reinecke, 1998;**
22
23 501 **Rubatto et al., 1998; Skora et al., 2015**). Re-hydration and destabilization of HP phases in
24
25 502 eclogite and metasediments indicates exhumation to greenschist-facies conditions following
26
27 503 the UHP peak (26 km/m.y.; **Amato et al., 1999**). HP serpentinites sandwich the UHP Lago di
28
29 504 Cignana Unit and display an antigorite + olivine foliation deforming olivine + Ti-
30
31 505 clinohumite + magnetite \pm diopside metamorphic veins. **Rebay et al. (2012)** recently studied
32
33 506 the serpentinites and associated eclogites lying below the Lago di Cignana Unit (the Zermatt
34
35 507 serpentinite). These serpentinites reached pressure conditions of 2.4–2.6 GPa during the
36
37 508 Alpine HP event (**Rebay et al., 2012; Angiboust et al., 2009**), like several other ophiolite
38
39 509 domains in the Western Alps (e.g. Erro-Tobbio, **Scambelluri et al., 1995**; Lanzo Ultramafic
40
41 510 Massif, **Pelletier and Müntener, 2006; Debret et al., 2013a, 2013b**). The serpentinites lying
42
43 511 above the Lago di Cignana Unit (the “Cignana serpentinites”) were, instead, never
44
45 512 investigated in detail and are commonly attributed to the Zermatt-Saas Zone. Our
46
47 513 observations of the Zermatt and Cignana serpentinites add further detail and information to
48
49 514 this scenario.
50
51
52
53
54
55
56
57
58
59
60

1
2
3 515 The HP Zermatt serpentinites are characterized by the formation of HP olivine via the
4
5 516 dehydration of brucite, according to the reaction (1) antigorite + brucite = olivine ± chlorite +
6
7 517 H₂O, which liberates a fluid phase drained in olivine + Ti-clinohumite + magnetite veins
8
9 518 (**Figure 14**). This type of vein forms in serpentinites during prograde metamorphism in the
10
11 519 presence of free water, after simultaneous breakdown of brucite (reaction 1 in Figure 14) and
12
13 520 former Ti-bearing clinopyroxene, according to the generalized reaction: mantle
14
15 521 clinopyroxene + olivine + antigorite = diopside + chlorite + Ti-clinohumite + H₂O (**López**
16
17 522 **Sánchez-Vizcaíno et al., 2009**). Genesis of such veins has been related to these dehydration
18
19 523 reactions in the Zermatt-Saas Zone (**Rebay et al., 2012; Zanoni et al., 2012**), as well as in
20
21 524 other HP serpentinites such as Erro-Tobbio (**Scambelluri et al., 1995**), the Lanzo Massif
22
23 525 (**Debret et al., 2013a**), and Cerro de Almirez (**López Sánchez-Vizcaíno et al., 2009**).

26
27 526 The Cignana serpentinites display a well-developed antigorite + olivine foliation,
28
29 527 locally deforming two distinct types of veins containing titanate phases: type 1 and type 2
30
31 528 veins. Type 1 veins contain Ti-clinohumite as the main Ti-bearing phase (large crystals,
32
33 529 locally overgrown by finer-grained Ti-clinohumite), plus olivine, chlorite, magnetite, and
34
35 530 rare diopside (**Figure 4e**). **Figure 14** shows a series of reaction lines (adapted from **Shen et**
36
37 531 **al., 2015**) in the system TiO₂-MgO-SiO₂-H₂O (plus the reactions graphite-diamond and
38
39 532 quartz-coesite for comparison with the LCU crustal lithologies), based on which the *P-T*
40
41 533 formation conditions of type 1 veins can be constrained (in analogy to the veins reported for
42
43 534 Almirez; **López Sánchez-Vizcaíno et al., 2009**). The *P-T* field is roughly divided into two
44
45 535 domains by reaction (5): an orange shaded area delimiting the stability field of Ti-
46
47 536 clinohumite, and a reddish area at higher pressure where Ti-chondrodite is stable. The black
48
49 537 arrow is the *PT* path proposed by **Groppo et al. (2009)** for eclogites in the Lago di Cignana
50
51 538 Unit. The origin of type 1 veins can be related to the formation of metamorphic diopside and
52
53 539 to brucite dehydration, according to reaction (1) and (2) respectively. Brucite dehydrates at a
54
55
56
57
58
59
60

1
2
3 540 temperature of around 500 °C, which corresponds to about 2.0–2.5 GPa (~ 75km depth)
4
5 541 considering the P – T estimates of eclogites from the ZSZ (Angiboust et al., 2009) and a
6
7 542 typical Alpine subduction geothermal gradient (6.5–7.5 °C/km; Scambelluri et al., 1995;
8
9 543 López Sánchez–Vizcaíno et al., 2009; Groppo et al., 2009). The TE composition of these
10
11 544 veins (Figure 9) closely compares to that of the host rock, suggesting dehydration in a closed
12
13 545 system, with little to no influx of externally derived components and fluids. As such, the
14
15 546 Cignana and Zermatt serpentinites released moderate amounts of aqueous fluid during
16
17 547 subduction, which slightly remobilized many elements and locally recrystallized as Ti–
18
19 548 clinohumite-bearing veins.

20
21
22
23 549 The second occurrence of Ti-bearing minerals concerns the type 2 veins, hosting
24
25 550 coarse Ti-chondrodite, chlorite, olivine, diopside, and apatite (Sample ZSG1402). The
26
27 551 presence of Ti-chondrodite as main vein-forming mineral readily indicates that type 2 veins
28
29 552 formed at higher pressures than type 1, in the stability field of Ti-chondrodite (orange shaded
30
31 553 area in Figure 14). Importantly, the P – T conditions necessary for the formation of Ti–
32
33 554 chondrodite-bearing veins are not recorded in the Zermatt–Saas Zone. To the contrary, they
34
35 555 are compatible with the P – T path recorded in the Lago di Cignana Unit eclogites and
36
37 556 metasediments (Figure 14; Groppo et al., 2009). Such estimates for the formation of type 2
38
39 557 veins lie at higher temperature than the dehydration reaction (1), which generated type 1
40
41 558 veins, and at lower temperature than the expected antigorite dehydration of reaction (2). As
42
43 559 such, it is unlikely that the fluid responsible for the type 2 veining had an internal origin as
44
45 560 for the type 1 veins. Instead, this fluid was probably externally derived (i.e. non–
46
47 561 serpentinitic). Hypotheses on the possible origins of such fluid are discussed below.

50
51 562 Deformation and recrystallisation of type 1 and 3 veins occurred during a lower
52
53 563 pressure deformation event (D3). Large crystals are replaced by smaller metamorphic phases:
54
55 564 Ti-clinohumite(2) replaces Ti-chondrodite and Ti-Clinohumite (Figure 4e–f–g–h); when

1
2
3 565 present, first generation olivine, chlorite, apatite, and diopside recrystallize. Regarding the
4
5 566 origin of such Ti–chondrodite veins, we propose here that type 2 veins crystallized from a
6
7 567 fluid derived from the nearby crustal Cignana rocks for the following petrologic and
8
9 568 geochemical reasons. Compared to type 1 Ti–clinohumite veins, the type 2 Ti–chondrodite
10
11 569 veins are strikingly enriched in REE, Th, U, Nb, Ta, As, Sb, and Y (**Figure 9**). This
12
13 570 enrichment can be interpreted to be due either to (1) metasomatism of initial gabbroic
14
15 571 dykelets (**Scambelluri & Rampone, 1999**) or to (2) channelized infiltration of metamorphic
16
17 572 fluids enriched in crustal components into the Cignana serpentinite at UHP conditions. In the
18
19 573 Voltri Massif, **Scambelluri & Rampone (1999)** described Ti–chondrodite + Ti–clinohumite
20
21 574 + diopside + chlorite bearing veinlets associated with the occurrence of igneous
22
23 575 clinopyroxene and ilmenite relics, which provided evidence for an origin from metasomatized
24
25 576 Fe–Ti gabbroic dykelets. Differently from Voltri, magmatic clinopyroxene and ilmenite relics
26
27 577 are absent in the Ti–chondrodite + olivine veinlets from Cignana. Nevertheless, favouring
28
29 578 hypothesis (2) does not enable to rule out hypothesis (1). However, a magmatic origin of such
30
31 579 veins should be recorded by the immobile elements in the bulk composition (e.g. Cr and Ni),
32
33 580 which are very different in concentration in a former gabbroic dyke with respect to a
34
35 581 peridotite. **Figure 7** shows that Cr–Ni bulk compositions of the Cignana Ti–chondrodite
36
37 582 veins are comparable with serpentinites, peridotites and type 1 veins is and strongly different
38
39 583 from reference eclogites and gabbroic dykes. This bears implications on the fluid origin of
40
41 584 type 2 Ti–chondrodite veins.
42
43
44
45

46
47 585 The petrogenetic sequence presented in **Figure 15** summarizes and compares the
48
49 586 metamorphic evolutions of the Zermatt serpentinites with the Cignana serpentinite and the
50
51 587 Lago di Cignana Unit. The mineralogical and textural evolution of the Cignana serpentinites
52
53 588 thus reveals prograde, peak, and retrograde events. The three metamorphic stages recorded in
54
55 589 type 1 and 2 veins and in their LP recrystallization products are comparable to the
56
57
58
59
60

1
2
3 590 metamorphic evolution defined for the coesite-bearing eclogites and metasediments (**Groppo**
4
5 591 **et al., 2009**). The type 1 veins can correspond to the prograde metamorphic zoning observed
6
7 592 in eclogitic garnet (**Reinecke, 1998; Groppo et al., 2009**), while type 2 Ti-chondrodite-
8
9 593 bearing veins in serpentinites likely formed under peak metamorphic conditions in the coesite
10
11 594 stability field. Consequently, peak conditions are consistent for both the Lago di Cignana
12
13 595 Unit and the Cignana serpentinites. Retrograde re-equilibration of eclogite and
14
15 596 metasediments (formation of chlorite after garnet and barroisite and glaucophane after
16
17 597 omphacite) indicates near-isothermal decompression (**Groppo et al., 2009**). In serpentinites,
18
19 598 this retrograde event causes the recrystallization of type 1 Ti-clinohumite and type 2 Ti-
20
21 599 chondrodite veins. As such, the microstructural and mineralogical record of the Ti-bearing
22
23 600 veins provides constraints to the evolution of the Lago di Cignana Unit and of the
24
25 601 surrounding serpentinites throughout their prograde, peak and retrograde evolution. A main
26
27 602 implication of this finding is the stability of the mineral association antigorite + olivine in
28
29 603 natural samples at UHP metamorphic condition, as predicted from experimental work by
30
31 604 **Ulmer & Trommsdorff (1995)**.

32
33
34
35
36 605 Zermatt-Saas serpentinites (ZSG1405, ZSG1406 and ZSG1410) are closely
37
38 606 comparable to Cignana serpentinites in petrology, microstructure, and field occurrence. As
39
40 607 such, it is difficult to clearly distinguish the Cignana serpentinites from the Zermatt-Saas
41
42 608 serpentinites; hence, the definition of a boundary for the UHP event in serpentinites is not
43
44 609 possible. Furthermore, the occurrence of Ti-chondrodite is not limited to the area
45
46 610 surrounding the LCU. Ti-Chondrodite is found in sample ZSG1406 and it is reported in other
47
48 611 sections of the Zermatt-Saas Zone (**Rebay et al. (2012)**; Tartarotti, Hermann, personal
49
50 612 communications). This might imply (1) deeper subduction of the Zermatt area than so far
51
52 613 known and only local preservation of the UHP mineralogy, or (2) that the Zermatt-Saas
53
54 614 consists of slices of oceanic crust and metasediments which were equilibrated at different
55
56
57
58
59
60

1
2
3 615 depths, and were then incorporated into the plate interface during exhumation. In this latter
4
5 616 case, the model of tectonic coherence of the Zermatt–Saas unit should be reconsidered, an
6
7 617 arduous task given the extensive greenschist–facies retrogression of metabasic rocks and/or
8
9 618 lack of viable pressure indicators. Trace element and isotopic analyses in serpentinites
10
11 619 (discussed below) proved to be a useful tool to discriminate between different serpentinite
12
13 620 slices.

621 **Geochemical evolution**

16
17
18
19 622 Recent work (**Hattori & Guillot, 2003; Deschamps et al., 2011, 2012, Lafay et al.,**
20
21 623 **2013; Scambelluri et al., 2014, 2015; Cannaò et al., 2015, 2016; Debret et al., 2013b**) has
22
23 624 investigated the role of serpentinites in acquiring and releasing FME during tectonic
24
25 625 processes. Interaction with subduction fluids (**Cannaò et al., 2015, 2016**), as well as
26
27 626 lizardite–antigorite and antigorite dehydration reactions (**Kodolányi and Pettke, 2011;**
28
29 627 **Debret et al., 2013a, 2013b**), change the TE budget of a serpentinite and might affect its Sr–
30
31 628 Pb isotopic signature (**Cannaò et al., 2015, 2016**). FME geochemistry, coupled with detailed
32
33 629 field and microstructural investigations, helps unravelling (1) the timing and tectonic setting
34
35 630 of fluid–rock interaction and (2) the evolution of the serpentinites during their subduction–
36
37 631 exhumation cycle.

38
39
40
41 632 Using this geochemical petrology approach, we discuss (1) the tectonic setting of
42
43 633 initial serpentinitization and the evolution and FME exchange of the Zermatt and Cignana
44
45 634 serpentinites and (2) the origin of fluids interacting with serpentinites. This will allow us to
46
47 635 propose a possible evolution of the Zermatt–Saas Zone near the Lago di Cignana Unit.

50 636 *Inherited features of Zermatt and Cignana serpentinites*

51
52
53 637 The Western Alpine ophiolites are fragments of different sections of the Ligurian–
54
55 638 Piemontese slow–spreading ocean opened during the Jurassic (**Dal Piaz et al., 2003;**

1
2
3 639 **Piccardo, 2008; Rampone et al., 2014**). Studies of pristine non-subducted sections of this
4
5 640 ocean basin show that the mantle peridotites underwent melt depletion and refertilization by
6
7 641 circulating melts in the stability fields of spinel and subsequently plagioclase. The final
8
9 642 composition of a peridotite is thus the result of combined processes of melt extraction, melt
10
11 643 percolation and melt-rock interactions, leading to dissolution of pyroxenes and
12
13 644 recrystallization of olivine (**Godard et al., 2000; Rampone et al., 2004; Müntener et al.,**
14
15 645 **2004**). This complex mantle history can be traced back in serpentinites by studying the
16
17 646 composition of mantle clinopyroxene relics and bulk rock major and rare earth elements,
18
19 647 which largely remain unaltered by serpentinization (**Niu, 2004**).

20
21
22
23 648 Zermatt and Cignana serpentinites only sporadically preserve relics of pristine mantle
24
25 649 clinopyroxene (e.g. **Figure 4a**). This scarcity of mineralogical relics of mantle phases affects
26
27 650 the whole Zermatt–Saas Zone (**Dal Piaz et al., 2003; Li et al., 2004; Angiboust et al., 2009;**
28
29 651 **Rebay et al., 2012**). Therefore, as a careful characterization of the serpentinite protolith
30
31 652 mineralogy is not feasible, geochemical data are used to constrain the mantle precursor rocks
32
33 653 and to define mass transfer and fluid/rock interaction during serpentinization at the seafloor
34
35 654 and during subduction.

36
37
38
39 655 To a first order, ocean floor serpentinization does not significantly affect the initial
40
41 656 peridotite major element budget and ratios (**Bogolepov, 1970; Coleman & Keith, 1971; Niu,**
42
43 657 **2004; Deschamps et al., 2013**). Exceptions are local CaO depletion due to serpentinization
44
45 658 and/or chloritization of Ca-bearing plagioclase and clinopyroxene, and/or fluid element
46
47 659 addition, introduction of silica (talc metasomatism; **Paulick et al, 2006**), Mg loss by marine
48
49 660 weathering (**Snow and Dick, 1995**), or CO₂ addition forming ophicarbonates near the ocean
50
51 661 floor (carbonation; **Bideau et al., 1991**). **Figure 6a–b** shows major element relations in
52
53 662 Zermatt and Cignana serpentinites. The Zermatt serpentinite displays a refractory
54
55 663 composition, with MgO > 37 % and low Al₂O₃ and CaO levels. To the contrary, the Cignana

1
2
3 664 serpentinite shows more enriched compositions, with lower MgO content and higher CaO
4
5 665 and Al₂O₃ (**Figure 6a–b**). As a first approximation, the major element composition of the
6
7 666 Zermatt and Cignana serpentinites may suggest a derivation from harzburgitic and lherzolitic
8
9 667 protolith, respectively.
10

11
12 668 In **Figure 9**, the REE compositions and patterns of (1) pristine depleted harzburgites
13
14 669 and (2) refertilized (plagioclase-impregnated) lherzolite from the Lanzo Massif (**Guarnieri**
15
16 670 **et al., 2012**) overlap with the Zermatt and Cignana serpentinites, respectively. One Cignana
17
18 671 serpentinite (sample ZSG1407S) is slightly more enriched, due to a larger mode of diopside.
19
20 672 In summary, the Zermatt and Cignana serpentinites features likely represent local
21
22 673 compositional variations within a coherent lithospheric mantle, which is a common feature of
23
24 674 the Thetian ophiolitic oceanic lithosphere (Internal Ligurides, **Rampone & Piccardo, 2000**;
25
26 675 **Erro–Tobbio, Rampone et al., 2014**; Lanzo, **Müntener et al., 2004**; **Guarnieri et al., 2012**).
27
28 676 Alternatively, the Cignana serpentinite might be a tectonic sliver sampling a different section
29
30 677 of lithospheric mantle, detached and juxtaposed over the Zermatt serpentinites only during
31
32 678 exhumation.
33
34
35

36 679 *Variation of the initial composition of the Zermatt and Cignana serpentinite*

37
38

39 680 Mantle peridotites can be serpentinized in oceanic as well as in subduction zone
40
41 681 settings. The serpentinization reactions occurring in the two different environments can be
42
43 682 accompanied by enrichments and/or depletion in key FME tracers (**Deschamps et al., 2013**;
44
45 683 **Peters et al., 2017**; **Kodolányi et al., 2012**; **Scambelluri & Tonarini, 2012**; **Lafay et al.,**
46
47 684 **2013**; **Debret et al, 2013b**). During subduction recrystallization, serpentinite can acquire TE,
48
49 685 depending on element mobility in aqueous solutions and on fluid–rock compatibility ratio
50
51 686 (K_d). Hence, previous studies led to identify the tectonic setting where different TE are
52
53 687 added, or removed, from serpentinites (e.g. **Scambelluri & Philippot, 2001**; **Kodolányi et**
54
55
56
57
58
59
60

1
2
3 688 **al., 2012; Debret et al., 2013b; Scambelluri et al., 2014; Peters et al., 2017)**. This allowed
4
5 689 to trace back distinct stages in tectonic history of the serpentinites, looking at differences in
6
7 690 micro-texture and trace element composition (**Cannaò et al., 2015, 2016**).

8
9
10 691 *Zermatt serpentinite*. Major element and REE patterns of the Zermatt serpentinite
11
12 692 indicate an origin from a depleted mantle peridotite protolith. The PM-normalized TE
13
14 693 composition of such serpentinites (**Figure 10**) shows that most TE (Cs, Rb, Ba, Th, U, K, Sr,
15
16 694 Zr, Hf, Ti, Ga, Li, Y, Sc) follow the mantle depletion trend, suggesting their concentrations
17
18 695 are largely controlled by depletion via melt extraction in the mantle. Differently, Bi, B, W,
19
20 696 Sn, Pb, As, Sb, and Mo show positive anomalies with respect to the mantle depletion trend;
21
22 697 some of the above TE also show higher contents with respect to refertilized, plagioclase-
23
24 698 impregnated peridotite from the Lanzo massif (**Guarnieri et al., 2012**). Recent work on
25
26 699 serpentinites from present-day abyssal and forearc settings, and from ophiolites pointed out
27
28 700 such enrichments can equally be attributed to ocean floor or subduction zone serpentinization
29
30 701 (**Niu, 2004; Boschi et al., 2008; Vils et al., 2009; Deschamps et al., 2011, 2012; Kodolányi**
31
32 702 **et al., 2012; Peters et al., 2017**). As such, the positive TE anomalies of the Zermatt
33
34 703 serpentinite cannot be attributed to a specific serpentinization environment. The lack of
35
36 704 prominent Cs enrichments while B is strongly enriched implies absence of a sedimentary
37
38 705 signature, however (**Peters et al., 2017**), and no significant U uptake (**Kodolányi et al.,**
39
40 706 **2012; Deschamps et al. 2013; Peters et al., 2017**) indicates slightly less oxidised
41
42 707 serpentinization fluids compared to, e.g., sea water (Langmuir, 1978). This is further
43
44 708 supported by $W/Mo > 1$, since fluid-mediated Mo transport and enrichment is more redox-
45
46 709 sensitive than for W for these otherwise geochemically very similar elements (e.g.,
47
48 710 **Koschinsky and Hein, 2003; Mohajerin et al., 2016**). Molybdenum will thus be less
49
50 711 strongly enriched than W by less oxidised fluids ($W/Mo = 0.06-0.18$ for mid-ocean ridge
51
52 712 serpentinites with $U = 0.211-1.02 \mu\text{g g}^{-1}$ in **Jöns et al., 2010**). Overall, such fluid
53
54
55
56
57
58
59
60

1
2
3 713 characteristics and resulting fluid signatures are like FME enrichment patterns observed in
4
5 714 some ocean floor serpentinites that have been sampled in somewhat deeper parts of the
6
7 715 lithospheric mantle at the ocean floor (**Peters et al., 2017**).

8
9
10 716 During oceanic serpentinization, the original peridotite also exchanges isotopes with
11
12 717 seawater. The very low Pb amount in seawater (Pb ~ 0.002 µg/g; **Li, 1982**) does not change
13
14 718 significantly the Pb content of serpentinite with respect to the original peridotite (Pb ~ 0.05
15
16 719 µg/g in DM), and does not strongly change the isotopic composition of these rocks. In this
17
18 720 respect, the 0.06–0.13 µg/g Pb and the Pb isotopic ratio of the Zermatt serpentinites are
19
20 721 within the range of the reference mantle peridotite (DM and unaltered Lanzo levels; Figures 9
21
22 722 and 10). Regarding Sr, the bulk Sr contents of serpentinites are strongly influenced by (1) the
23
24 723 presence of clinopyroxene porphyroclasts, which retain most of the bulk Sr content and have
25
26 724 a mantle isotopic imprint ($^{87}\text{Sr}/^{86}\text{Sr} \sim 0.7030$) and (2) by the amount of Sr introduced by the
27
28 725 aqueous fluid hydrating the rock during serpentinization. As clinopyroxene is generally more
29
30 726 resistant than olivine to serpentinization, partially serpentinized peridotites will retain most of
31
32 727 their mantle isotopic signature and thus have a Sr isotopic composition lying on a mixing line
33
34 728 between pristine peridotite and seawater. Since mantle clinopyroxene clasts in the Zermatt
35
36 729 serpentinite are scarce (< 5 vol.%), the bulk isotopic composition of these rocks well
37
38 730 approximates the composition of the serpentinization fluid. As such, the $^{87}\text{Sr}/^{86}\text{Sr}$
39
40 731 compositions of the Zermatt serpentinites ($^{87}\text{Sr}/^{86}\text{Sr} = 0.707051\text{--}0.708303$) imply exchange
41
42 732 with Jurassic seawater in accordance with TE data, without further indications for interaction
43
44 733 with either sediment–equilibrated fluids in forearc regions or subduction–derived fluids along
45
46 734 the subduction interface.

47
48
49
50
51 735 Like the bulk–rock TE composition, rock forming minerals in Zermatt serpentinite
52
53 736 display enrichments in B, As, and Sb. These elements are equally stored in antigorite and
54
55 737 metamorphic diopside. Antigorite displays a steady increase in HREEs relative to LREEs,
56
57
58
59
60

1
2
3 738 and strong enrichments in B, As, and Sb, showing a pattern compatible with oceanic
4
5 739 serpentinization of olivine (**Kodolányi et al., 2012**). Similarly, prograde diopside REE
6
7 740 patterns likely reflect the composition of the original mantle clinopyroxene, with enrichments
8
9 741 of B, W, As, and Sb due to oceanic hydration. Ti-clinohumite shows an enrichment in Nb
10
11 742 and Ta up to PM levels, consistent with the high compatibility of high field strength elements
12
13 743 in humite-group minerals (**Garrido et al., 2005**). The strong B enrichment in Ti-clinohumite
14
15 744 from HP veins suggests its preferential partitioning into the fluid-phase compared to other
16
17 745 elements during serpentinite dehydration.

18
19
20
21 746 In summary, TE and the Sr-Pb isotopes suggest that the Zermatt serpentinite
22
23 747 represents a section of the oceanic slab, which was serpentinized during the Jurassic
24
25 748 spreading of the Tethys and still largely retains the original oceanic geochemical signature
26
27 749 despite its deep subduction and exhumation during the Alpine orogeny.

28
29
30 750 *Cignana serpentinite*. Compared with reference refertilized plagioclase peridotite
31
32 751 from Lanzo (**Figure 9**), the Cignana serpentinites show enrichments in Th, U, B, W, Nb, Ta,
33
34 752 Be, Sn, As, Sb, and Sr. Like in the Zermatt serpentinite, FME patterns might be related to
35
36 753 interaction with seawater-derived and slightly reduced fluids in oceanic environments.
37
38 754 However, the elevated Th, Be, Nb, Ta, and Sr contents combined with high As and Sb when
39
40 755 compared to the Zermatt serpentinite, suggest inputs from reservoirs other than seawater.

41
42
43 756 Arsenic and Sb, for instance, are generally acquired in moderate amounts during
44
45 757 oceanic serpentinization except for proximity to major hydrothermal sites where significant
46
47 758 sulphide precipitation occurs (**Andreani et al., 2014**). Moreover, several recent works
48
49 759 suggest that elevated contents of As and Sb can be acquired during subduction and
50
51 760 serpentinite emplacement in the accretionary wedge and plate interface (**Hattori & Guillot,**
52
53 761 **2003, 2007; Hattori et al., 2005; Deschamps et al., 2011, 2012; Lafay et al., 2013;**

1
2
3 762 **Scambelluri et al., 2014; Cannaò et al., 2015, 2016**). **Figure 16a** shows the potential
4
5 763 relationships between As and Sb of the Zermatt and Cignana serpentinites compared with
6
7 764 eclogite and metasediments from the Lago di Cignana Unit and with some major global
8
9 765 reservoirs (GLOSS-II, **Plank, 2014**; depleted mantle, **Rehka & Hofmann, 1997**; Jurassic
10
11 766 seawater, **Jones & Jenkyns, 2001**; average continental crust, **Rudnick and Gao, 2003**).
12
13 767 While the Zermatt–Saas serpentinite plots near DM and PM (suggesting just oceanic
14
15 768 alteration) the Cignana serpentinites display variable increase in their As and Sb budgets with
16
17 769 respect to Zermatt–Saas. This enrichment can be either due to (1) an intensive oceanic
18
19 770 hydrothermal alteration (**Andreani et al., 2014**) or to (2) exchange with crustal rock
20
21 771 reservoirs during subduction (**Lafay et al., 2013; Scambelluri et al., 2014; Cannaò et al.,**
22
23 772 **2015, 2016**). The Cignana serpentinite also plots close to the Lago di Cignana eclogite and
24
25 773 metasediments, suggesting an exchange of these elements with such rocks during subduction.
26
27 774 Furthermore, this enrichment is comparable with that recorded by other HP serpentinites
28
29 775 (Voltri) and metaperidotites (Cima di Gagnone) for which the uptake of As and Sb via
30
31 776 interaction of crust–derived subduction fluids has been shown on textural and geochemical
32
33 777 grounds (**Cannaò et al., 2015; 2016; Scambelluri et al., 2014**).

34
35
36
37
38 778 A further discrimination between oceanic and subduction input of FME to
39
40 779 serpentinites can be defined by the B vs. Sr diagram (**Figure 16b**). The diagram shows that
41
42 780 oceanic abyssal serpentinites are more enriched in B relative to Sr, whereas the subduction
43
44 781 zone serpentinites display an opposite trend. In **Figure 16b**, the Zermatt–Saas serpentinite
45
46 782 overlaps the abyssal serpentinite trend whereas the Cignana serpentinite is strongly enriched
47
48 783 in Sr with respect to B. This suggests a dual origin for the observed enrichments: prevalently
49
50 784 oceanic in the Zermatt serpentinite vs. prevalently subduction–related in the Cignana
51
52 785 serpentinite.
53
54
55
56
57
58
59
60

1
2
3 786 Finally, **Figure 16c** shows the concentrations in Th and U within the same suite of
4
5 787 Zermatt and Cignana rocks. The strong enrichment in U of abyssal serpentinites has been
6
7 788 widely documented as due to interactions with ocean waters (up to 3.2 $\mu\text{g/g}$; **Bailey and**
8
9 789 **Ragnarsdottir, 1994; Kodolányi et al., 2012; Deschamps et al., 2013; Peters et al., 2017**).
10
11 790 The Zermatt serpentinite plots close to the DM and overlies the field of unaltered oceanic
12
13 791 Lanzo peridotite and suggests scarce U uptake from seawater, i.e., in slightly reduced
14
15 792 environments such as deeper parts of the oceanic mantle (Peters et al., 2017) or at the sea
16
17 793 floor. Conversely, the Cignana serpentinite fall along a trend of coupled U and Th enrichment
18
19 794 towards crustal reservoirs: a same trend followed by some subduction zone serpentinites
20
21 795 (**Deschamps et al., 2013**, and reference therein).

22
23
24
25 796 Rock forming minerals in Cignana serpentinite show enrichments like those reported
26
27 797 for the bulk rock. Like antigorite from the Zermatt serpentinite, antigorite from the Cignana
28
29 798 serpentinite shows an enrichment in heavy- respect to light-REE and enrichments in B, As
30
31 799 and Sb, compatible with the oceanic serpentinization of olivine (**Kodolányi et al., 2012**).
32
33 800 However, elevated levels of Th and Be in antigorite (present also in diopside) cannot be
34
35 801 solely attributed to oceanic serpentinization and, as suggested for bulk rock, might indicate
36
37 802 Th and Be enrichment during subduction (**Figure 13**). Ti-clinohumite shows an enrichment
38
39 803 of up to 100 PM in Nb and Ta, again consistent with the high compatibility of high field
40
41 804 strength elements in humite-group minerals (**Garrido et al., 2005**).

42
43
44
45 805 Since dehydration of crustal lithologies during subduction may produce fluids
46
47 806 carrying substantial amounts of Sr, Be and possibly Th, the TE data shown in **Figure 16**
48
49 807 suggest that the Cignana serpentinites underwent exchange with subduction fluids that
50
51 808 increased their budget in Sr, Be and Th with respect to the Zermatt serpentinite, which
52
53 809 essentially records an oceanic imprint. The serpentinization environment and process of
54
55 810 Cignana can be traced also by Sr and Pb isotopic compositions. **Figure 17** reports the Sr and

1
2
3 811 Pb isotopic values of Zermatt serpentinites along with the Cignana serpentinite, eclogite and
4
5 812 metasediments. Also shown are the DM, MORB, Continental Crust, and GLOSS-II
6
7 813 compositions (GLOSS-II; **Plank, 2014**; depleted mantle, **Rehka & Hofmann, 1997**; Jurassic
8
9 814 seawater, **Jones & Jenkyns, 2001**; average continental crust, **Rudnick and Gao, 2003**). As
10
11 815 previously explained, the Zermatt and Cignana serpentinites underwent intensive (~95 vol.%)
12
13 816 serpentinization, which implies that their isotopic composition records that of the
14
15 817 serpentinizing fluid. The Sr isotope values of the Zermatt serpentinite overlap with Jurassic
16
17 818 seawater ($^{87}\text{Sr}/^{86}\text{Sr} = 0.7070$), which confirms that serpentinization prevalently occurred in
18
19 819 oceanic environment. Similarly, the Cignana serpentinite experienced an oceanic
20
21 820 serpentinization, as suggested by B and Cs signatures and by the presence of boudinaged
22
23 821 rodingite dykes. However, the more primitive Sr isotopic composition of this serpentinite
24
25 822 points to an exchange with a different fluid that may have exchanged with metabasaltic
26
27 823 material such as the Cignana eclogite.

30
31 824 To conclude, the Zermatt–Saas serpentinites largely inherit an oceanic signature
32
33 825 acquired by interactions with seawater. The Cignana serpentinites were originally exposed
34
35 826 near the sea–floor and acquired an oceanic signature still recorded by trace elements such as
36
37 827 B, Cs and W. During subduction, fluids equilibrated with altered oceanic crust interacted with
38
39 828 the Cignana serpentinites, largely modifying its trace element (prevalently Th, Sr, and Be,
40
41 829 and to a lesser extent As and Sb) and Sr and Pb isotopic compositions.

42
43
44
45 830 *Veins.* Based on petrologic evidence the type 1 olivine + Ti–clinohumite veins in
46
47 831 Cignana serpentinite formed during subduction, likely resulting from brucite + antigorite
48
49 832 dehydration occurring at about 450 °C (reaction 1 in **Figure 14**). The chemical and isotopic
50
51 833 compositions of such veins is comparable to that of the host serpentinite (**Figure 9, Figure**
52
53 834 **13, Figure 16**), which suggests that dehydration of the Cignana serpentinites occurred in a
54
55 835 closed system, and infiltration of externally–derived subduction fluids is not indicated.

1
2
3 836 Consequently, FME enrichment and fluid–rock interaction between the Cignana serpentinite
4
5 837 and fluids of crustal origin occurred during the first stages of subduction, i.e., before this
6
7 838 dehydration event. It implies that the Cignana serpentinites were associated with subducting
8
9 839 oceanic crust of the type cropping out in the nearby Lago di Cignana Unit, already since the
10
11 840 first stages of subduction.
12
13

14 841 According to petrographic observations and to recently published experimental work
15
16 842 by **Shen et al. (2015)**, the type 2 Ti–chondrodite veins in the Cignana serpentinites could
17
18 843 have crystallized during the UHP metamorphic peak at 3.2 GPa and 600 °C (peak estimates
19
20 844 for Cignana eclogites after **Groppo et al., 2009**). Hence, in the Cignana serpentinite, this Ti–
21
22 845 chondrodite likely formed after the HP type 1 veins.
23
24

25 846 The presence of Ti–chondrodite–bearing type 2 veins suggests their formation
26
27 847 occurred at PT conditions in–between the brucite–out and antigorite–out dehydration
28
29 848 reactions (reactions 1 and 2 in **Figure 14**). The origin of the fluid responsible for type 2 Ti–
30
31 849 chondrodite veins cannot thus be related to a specific serpentinite dehydration event, as
32
33 850 suggested for type 1 veins. Instead, the fluid might be derived from an external source rich in
34
35 851 U, Th, As, and Sb. Furthermore, the bulk REE patterns are strongly controlled by 2–3 % vol.
36
37 852 of overly enriched apatite crystals (**Figures 4e and 13**). Although rare in type 2 veins, apatite
38
39 853 crystals can account for the bulk LREE enrichment and thus explain its high LREE
40
41 854 concentrations.
42
43
44

45 855 The Sr–Pb isotopic signature of the Ti–chondrodite vein might help understanding
46
47 856 fluid–rock interaction and fluid paths in UHP subduction systems. The comparatively
48
49 857 radiogenic Pb–isotope composition (close to GLOSS–II values) in the Ti–chondrodite vein is
50
51 858 not yet fully understood. One possibility is that it might indicate a sedimentary/crustal
52
53 859 hybridized origin of the UHP fluid generating the vein. However, this should strongly
54
55
56
57
58
59
60

1
2
3 860 influence the Sr isotopes, making them more radiogenic (as for the cases of Voltri
4
5 861 serpentinite and Cima di Gagnone metaperidotite described by Cannà et al., 2015; 2016),
6
7 862 which is not the case.
8
9

10 863 CONCLUSIONS

11
12 864 We have shown that the eclogite facies serpentinites from Valtournenche (Zermatt–
13
14
15 865 Saas Zone and the serpentinite enveloping the UHP Lago di Cignana Unit) display different
16
17 866 metamorphic histories and different metamorphic and trace element signatures.
18

19 867 1. The Zermatt and Cignana serpentinites record different Alpine
20
21 868 pressure–temperature paths. The top of the coherent Zermatt–Saas Zone consists of a
22
23 869 thin sliver of UHP serpentinites (the Cignana serpentinite). The Zermatt–Saas
24
25 870 serpentinite shows formation of metamorphic olivine and Ti–clinohumite–bearing
26
27 871 assemblages in rock and vein systems. Overall, development of this paragenesis
28
29 872 requires a stage of antigorite + brucite dehydration in the Ti–clinohumite stability
30
31 873 field at P–T conditions of about 2–2.5 GPa and 450–500 °C. The serpentinite
32
33 874 enveloping the UHP Lago di Cignana Unit shows a first crystallization of olivine +
34
35 875 Ti–clinohumite in rocks and veins (type 1 veins) at about 2.0 GPa and 450–500 °C.
36
37 876 The Cignana serpentinite also includes Ti–chondrodite veins (type 2) formed at higher
38
39 877 pressure and temperature of about 3.0 GPa and 600–650 °C, comparable to the UHP
40
41 878 conditions recorded by the nearby UHP Cignana eclogite and metasediments. Type 1
42
43 879 and type 2 veins are both overgrown by later stage Ti–clinohumite.
44
45

46
47 880 2. Antigorite + olivine + Ti–clinohumite/chondrodite serpentinites are
48
49 881 thus a stable UHP mineral association, being representative of UHP, coesite–facies
50
51 882 conditions.
52

53
54 883 3. Bulk–rock major and trace element data indicate that the Zermatt and
55
56 884 the Cignana serpentinites derive from different mantle photoliths, and either represent
57
58
59
60

1
2
3 885 two separate units of different oceanic origin, or two sections of heterogeneous
4
5 886 oceanic mantle.

6
7 887 4. The fluid–mobile element and isotopic composition of the Cignana
8
9 888 serpentinite suggests it experienced geochemical exchange with the nearby Cignana
10
11 889 crustal rocks. This geochemical imprint is different from that of the Zermatt
12
13 890 serpentinite, which mostly preserves oceanic geochemical characteristics because
14
15 891 subduction took place under closed system conditions. This evidence reinforces the
16
17 892 hypothesis that the Cignana UHP rocks were tectonically coupled with the
18
19 893 surrounding serpentinite during subduction, and shows that the tectonic horizon
20
21 894 including the Lago di Cignana Unit and other tectonic slices (Etirol–Levaz,
22
23 895 **Beltrando et al., 2010**; Teodulo, **Skora et al., 2015**; Allalin Gabbro, **Bucher &**
24
25 896 **Grapes, 2009**; dismembered sections of Austroalpine domain like Mt. Emilius,
26
27 897 Figure 1) behaved as a major discontinuity (plate interface) during exhumation.
28
29
30

31 898 **ACKNOWLEDGEMENTS**

32
33
34 899 We greatly benefitted from discussions with P. Agard, E. Cannà, H. Marschall, J.
35
36 900 Hermann, D. Rubatto, and all scientists and fellows from the ZIP project ([http://www.zip-](http://www.zip-itn.eu/)
37
38 901 [itn.eu/](http://www.zip-itn.eu/)): discussions within ZIP stimulated this work. We thank A. Risplendente and L.
39
40 902 Negretti for technical assistance during the SEM and wavelength-dispersive spectrometry
41
42 903 microprobe work. We acknowledge funding by the People Programme (Marie Curie Actions,
43
44 904 European Union’s Seventh Framework Programme FP7/2007—2013) to the Initial Training
45
46 905 Network ZIP (Zooming In-between Plates, REA grant agreement no. 604713). M.S. also
47
48 906 acknowledges support from the Italian MIUR and the University of Genova.
49
50

51 907 **REFERENCES**

- 1
2
3 908 Agard, P., Yamato, P., Jolivet, L. & Burov, E. (2009). Exhumation of oceanic blueschists and
4
5 909 eclogites in subduction zones: timing and mechanisms. *Earth-Science Reviews* 92(1),
6
7 910 53–79.
- 8
9 911 Amato, J.M., Johnson, C.M., Baumgartner, L.P. & Beard, B.L. (1999). Rapid exhumation of
10
11 912 the Zermatt-Saas ophiolite deduced from high-precision Sm-Nd and Rb-Sr
12
13 913 geochronology. *Earth and Planetary Science Letters* 171(3), 425–438.
- 14
15 914 Andreani, M., Escartin, J., Delacour, A., Ildefonse, B., Godard, M., Dymont, J., Fallick, A.E.
16
17 915 & Fouquet, Y. (2014). Tectonic structure, lithology, and hydrothermal signature of the
18
19 916 Rainbow massif (Mid-Atlantic Ridge 36° 14' N). *Geochemistry, Geophysics,*
20
21 917 *Geosystems* 15(9), 3543-3571.
- 22
23 918 Angiboust, S., Agard, P., Jolivet, L. & Beyssac, O. (2009). The Zermatt-Saas ophiolite: the
24
25 919 largest (60-km wide) and deepest (c. 70–80 km) continuous slice of oceanic
26
27 920 lithosphere detached from a subduction zone? *Terra Nova* 21(3), 171–180.
- 28
29 921 Angiboust, S., Agard, P., Raimbourg, H., Yamato, P. & Huet, B. (2011). Subduction interface
30
31 922 processes recorded by eclogite-facies shear zones (Monviso, W. Alps). *Lithos* 127(1),
32
33 923 222–238.
- 34
35 924 Angiboust, S., Agard, P., Yamato, P. & Raimbourg, H. (2012b). Eclogite breccias in a
36
37 925 subducted ophiolite: A record of intermediate-depth earthquakes? *Geology* 40(8),
38
39 926 707–710.
- 40
41 927 Angiboust, S., Pettke, T., De Hoog, J.C., Caron, B. & Oncken, O. (2014). Channelized fluid
42
43 928 flow and eclogite-facies metasomatism along the subduction shear zone. *Journal of*
44
45 929 *Petrology* 55(5), 883–916.
- 46
47 930 Bailey, E.H. & Ragnarsdottir, K.V. (1994). Uranium and thorium solubilities in subduction
48
49 931 zone fluids. *Earth and Planetary Science Letters* 124(1-4), 119-129.
- 50
51
52
53
54
55
56
57
58
59
60

- 1
2
3 932 Bearth, P. & Schwander, H. (1981). The post-Triassic sediments of the ophiolite zone
4
5 933 Zermatt-Saas Fee and the associated manganese mineralizations. *Eclogae Geologicae*
6
7 934 *Helveticae* 74(1), 189–205.
- 8
9 935 Bearth, P.P. (1967). *Die Ophiolithe der Zone von Zermatt-Saas Fee*. Kummerly & Frey.
- 10
11 936 Bebout, G.E. (2007). Metamorphic chemical geodynamics of subduction zones. *Earth and*
12
13 937 *Planetary Science Letters* 260(3), 373–393.
- 14
15 938 Beltrando, M., Rubatto, D. & Manatschal, G. (2010). From passive margins to orogens: The
16
17 939 link between ocean-continent transition zones and (ultra) high-pressure
18
19 940 metamorphism. *Geology* 38(6), 559–562.
- 20
21 941 Bideau, D., Hebert, R., Hekinian, R. & Cannat, M. (1991). Metamorphism of deep-seated
22
23 942 rocks from the Garrett Ultrafast Transform (East Pacific Rise near 13° 25' S). *Journal*
24
25 943 *of Geophysical Research: Solid Earth* 96(B6), 10079-10099.
- 26
27 944 Bogolepov, V.G. (1970). Problem of serpentinization of ultrabasic rocks. *International*
28
29 945 *Geology Review* 12(4), 421-432.
- 30
31 946 Boschi, C., Dini, A., Früh-Green, G.L. & Kelley, D.S. (2008). Isotopic and element exchange
32
33 947 during serpentinization and metasomatism at the Atlantis Massif (MAR 30 N):
34
35 948 insights from B and Sr isotope data. *Geochimica et Cosmochimica Acta* 72(7), 1801-
36
37 949 1823.
- 38
39 950 Bostock, M., Hyndman, R., Rondenay, S. & Peacock, S. (2002). An inverted continental
40
41 951 moho and serpentinization of the forearc mantle. *Nature* 417(6888), 536–538.
- 42
43 952 Bostock, M. (2013). The moho in subduction zones. *Tectonophysics* 609, 547–557.
- 44
45 953 Brovarone, A. V., Beyssac, O., Malavieille, J., Molli, G., Beltrando, M. & Compagnoni, R.
46
47 954 (2013). Stacking and metamorphism of continuous segments of subducted lithosphere
48
49 955 in a high-pressure wedge: The example of Alpine Corsica (France). *Earth-Science*
50
51 956 *Reviews* 116, 35–56.
- 52
53
54
55
56
57
58
59
60

- 1
2
3 957 Bucher, K. & Grapes, R. (2009). The eclogite-facies Allalin gabbro of the Zermatt–Saas
4
5 958 ophiolite, Western Alps: a record of subduction zone hydration. *Journal of Petrology*,
6
7 959 *egp035*.
8
9 960 Bucher, K., Fazis, Y., Capitani, C.D. & Grapes, R. (2005). Blueschists, eclogites, and
10
11 961 decompression assemblages of the Zermatt-Saas ophiolite: High-pressure
12
13 962 metamorphism of subducted Tethys lithosphere. *American Mineralogist* 90(5-6), 821–
14
15 963 835.
16
17 964 Cannaò, E., Agostini, S., Scambelluri, M., Tonarini, S. & Godard, M. (2015). B, Sr and Pb
18
19 965 isotope geochemistry of high-pressure Alpine metaperidotites monitors fluid-mediated
20
21 966 element recycling during serpentinite dehydration in subduction mélange (Cima di
22
23 967 Gagnone, Swiss Central Alps). *Geochimica et Cosmochimica Acta* 163, 80–100.
24
25
26 968 Cannaò, E., Scambelluri, M., Agostini, S., Tonarini, S. & Godard, M. (2016). Linking
27
28 969 serpentinite geochemistry with tectonic evolution at the subduction plate-interface:
29
30 970 The Voltri massif case study (Ligurian Western Alps, Italy). *Geochimica et*
31
32 971 *Cosmochimica Acta* 190, 115–133.
33
34
35 972 Cannat, M., Mevel, C., Maia, M., Deplus, C., Durand, C., Gente, P., Agrinier, P., Belarouchi,
36
37 973 A., Dubuisson, G., Humler, E., et al. (1995). Thin crust, ultramafic exposures, and
38
39 974 rugged faulting patterns at the Mid-Atlantic Ridge (22–24 n). *Geology* 23(1), 49–52.
40
41
42 975 Coleman, R.G. & Keith, T.E. (1971). A chemical study of serpentinization—Burro Mountain,
43
44 976 California. *Journal of Petrology* 12(2), 311-328.
45
46 977 Dal Piaz, G.V., Bistacchi, A. & Massironi, M. (2003). Geological outline of the Alps.
47
48 978 *Episodes* 26(3), 175-180.
49
50 979 Dal Piaz, G.V. (1992). *Alpi dal monte bianco al lago maggiore. guide geologiche regionali*.
51
52 980 *Vol. 3. Societa Geologica Italiana. BE-MA Editrice*.
53
54
55
56
57
58
59
60

- 1
2
3 981 Debret, B., Nicollet, C., Andreani, M., Schwartz, S. & Godard, M. (2013a). Three steps of
4
5 982 serpentinitization in an eclogitized oceanic serpentinitization front (Lanzo Massif–
6
7 983 Western Alps). *Journal of Metamorphic Geology* 31(2), 165–186.
8
9 984 Debret, B., Andreani, M., Godard, M., Nicollet, C., Schwartz, S. & Lafay, R. (2013b). Trace
10
11 985 element behaviour during serpentinitization/de-serpentinitization of an eclogitized
12
13 986 oceanic lithosphere: A LA-ICPMS study of the Lanzo Ultramafic Massif (Western
14
15 987 Alps). *Chemical Geology* 357, 117–133.
16
17
18 988 Deschamps, F., Guillot, S., Godard, M., Andreani, M. & Hattori, K. (2011). Serpentinites act
19
20 989 as sponges for fluid-mobile elements in abyssal and subduction zone environments.
21
22 990 *Terra Nova* 23(3), 171–178.
23
24 991 Deschamps, F., Godard, M., Guillot, S., Chauvel, C., Andreani, M., Hattori, K., Wunder, B.
25
26 992 & France, L. (2012). Behavior of fluid-mobile elements in serpentines from abyssal to
27
28 993 subduction environments: Examples from Cuba and Dominican Republic. *Chemical*
29
30 994 *Geology* 312, 93-117.
31
32
33 995 Deschamps, F., Godard, M., Guillot, S. & Hattori, K. (2013). Geochemistry of subduction
34
35 996 zone serpentinites: A review. *Lithos* 178, 96–127.
36
37 997 Ernst, W.G. & Dal Piaz, G.V. (1978). Mineral parageneses of eclogitic rocks and related
38
39 998 mafic schists of the Piemonte ophiolite nappe, Breuil-St. Jacques area, Italian Western
40
41 999 Alps. *American Mineralogist* 63(7-8), 621-640.
42
43
44 1000 Forster, M., Lister, G., Compagnoni, R., Giles, D., Hills, Q., Betts, P., Beltrando, M.,
45
46 1001 Tamagno, E. (2004). Mapping of oceanic crust with "HP" to "UHP" metamorphism:
47
48 1002 The Lago di Cignana Unit (Western Alps). *Mapping geology in Italy*.
49
50 1003 Frezzotti, M., Selverstone, J., Sharp, Z. & Compagnoni, R. (2011). Carbonate dissolution
51
52 1004 during subduction revealed by diamond-bearing rocks from the Alps. *Nature*
53
54 1005 *Geoscience* 4(10), 703–706.
55
56
57
58
59
60

- 1
2
3 1006 Garrido, C.J., López Sánchez-Vizcaíno, V., Gómez-Pugnaire, M.T., Trommsdorff, V.,
4
5 1007 Alard, O., Bodinier, J.L. & Godard, M. (2005). Enrichment of HFSE in Chlorite
6
7 1008 Harzburgite produced by high-pressure dehydration of Antigorite-Serpentinite:
8
9 1009 implications for subduction magmatism. *Geochemistry, Geophysics, Geosystems*
10
11 1010 6(1).
12
13 1011 Godard, M., Jousselin, D. & Bodinier, J.L. (2000). Relationships between geochemistry and
14
15 1012 structure beneath a paleo-spreading centre: a study of the mantle section in the Oman
16
17 1013 ophiolite. *Earth and Planetary Science Letters* 180(1), 133-148.
18
19
20 1014 Groppo, C., Beltrando, M. & Compagnoni, R. (2009). The P-T path of the ultra-high-
21
22 1015 pressure Lago di Cignana and adjoining high-pressure meta-ophiolitic units: insights
23
24 1016 into the evolution of the subducting Tethyan slab. *Journal of Metamorphic Geology*
25
26 1017 27(3), 207–231.
27
28
29 1018 Guarnieri, L., Nakamura, E., Piccardo, G.B., Sakaguchi, C., Shimizu, N., Vannucci, R. &
30
31 1019 Zanetti, A. (2012). Petrology, trace element and SR, Nd, Hf isotope geochemistry of
32
33 1020 the North Lanzo peridotite massif (Western Alps, Italy). *Journal of Petrology* 53(11),
34
35 1021 2259-2306.
36
37 1022 Guillong, M., Meier, D.L., Allan, M.M., Heinrich, C.A. & Yardley, B.W. (2008). Appendix
38
39 1023 A6: SILLS: A MATLAB-based program for the reduction of laser ablation ICP-MS
40
41 1024 data of homogeneous materials and inclusions. *Mineralogical Association of Canada*
42
43 1025 *Short Course* 40, 328-333.
44
45
46 1026 Guillot, S., Hattori, K.H., de Sigoyer, J., Nägler, T. & Auzende, A.L. (2001). Evidence of
47
48 1027 hydration of the mantle wedge and its role in the exhumation of eclogites. *Earth and*
49
50 1028 *Planetary Science Letters* 193(1), 115-127.
51
52
53 1029 Guillot, S., Schwartz, S., Reynard, B., Agard, P. & Prigent, C. (2015). Tectonic significance
54
55 1030 of serpentinites. *Tectonophysics* 646, 1–19.
56
57
58
59
60

- 1
2
3 1031 Hattori, K.H. & Guillot, S. (2003). Volcanic fronts form as a consequence of serpentinite
4
5 1032 dehydration in the forearc mantle wedge. *Geology* 31(6), 525-528.
6
7 1033 Hattori, K.H. & Guillot, S. (2007). Geochemical character of serpentinites associated with
8
9 1034 high- to ultrahigh-pressure metamorphic rocks in the Alps, Cuba, and the Himalayas:
10
11 1035 Recycling of elements in subduction zones. *Geochemistry, Geophysics, Geosystems*
12
13 1036 8(9).
14
15 1037 Hattori, K., Takahashi, Y., Guillot, S. & Johanson, B. (2005). Occurrence of arsenic (V) in
16
17 1038 forearc mantle serpentinites based on X-ray absorption spectroscopy study.
18
19 1039 *Geochimica et Cosmochimica Acta* 69(23), 5585–5596.
20
21 1040 Hermann, J., Müntener, O. & Scambelluri, M. (2000). The importance of serpentinite
22
23 1041 mylonites for subduction and exhumation of oceanic crust. *Tectonophysics* 327(3),
24
25 1042 225–238.
26
27 1043 Ionov, D. A., Savoyant, L. & Dupuy, C. (1992). Application of the ICP-MS technique to
28
29 1044 trace element analysis of peridotites and their minerals. *Geostandards and*
30
31 1045 *Geoanalytical Research* 16(2), 311-315.
32
33 1046 Iwamori, H. (1998). Transportation of H₂O and melting in subduction zones. *Earth and*
34
35 1047 *Planetary Science Letters*, 160(1), 65-80.
36
37 1048 Jochum, K.P., Seufert, H.M. & Thirlwall, M.F. (1990). High-sensitivity Nb analysis by
38
39 1049 spark-source mass spectrometry (SSMS) and calibration of XRF Nb and Zr. *Chemical*
40
41 1050 *Geology* 81(1-2), 1-16.
42
43 1051 John, T., Scambelluri, M., Frische, M., Barnes, J.D. & Bach, W. (2011). Dehydration of
44
45 1052 subducting serpentinite: implications for halogen mobility in subduction zones and the
46
47 1053 deep halogen cycle. *Earth and Planetary Science Letters* 308(1), 65–76.
48
49
50
51
52
53
54
55
56
57
58
59
60

- 1
2
3 1054 Jones, C.E. & Jenkyns, H.C. (2001). Seawater strontium isotopes, oceanic anoxic events, and
4
5 1055 seafloor hydrothermal activity in the Jurassic and Cretaceous. *American Journal of*
6
7 1056 *Science* 301(2), 112–149.
8
9 1057 Jöns, N., Bach, W., & Klein, F. (2010). Magmatic influence on reaction paths and element
10
11 1058 transport during serpentinization. *Chemical Geology*, 274(3–4), 196–211.
12
13 1059 Kelemen, P. B., Hanghøj, K., & Greene, A. R. (2003). One view of the geochemistry of
14
15 1060 subduction-related magmatic arcs, with an emphasis on primitive andesite and lower
16
17 1061 crust. *Treatise on geochemistry*, 3, 659.
18
19 1062 Kendrick, M.A., Scambelluri, M., Honda, M. & Phillips, D. (2011). High abundances of
20
21 1063 noble gas and chlorine delivered to the mantle by serpentinite subduction. *Nature*
22
23 1064 *Geoscience* 4(11), 807–812.
24
25 1065 Kendrick, M.A., Hémond, C., Kamenetsky, V.S., Danyushevsky, L., Devey, C.W.,
26
27 1066 Rodemann, T. & Perfit, M.R. (2017). Seawater cycled throughout Earth's mantle in
28
29 1067 partially serpentinized lithosphere. *Nature Geoscience* 10(3), 222-228.
30
31 1068 Kodolányi, J. & Pettke, T. (2011). Loss of trace elements from serpentinites during fluid-
32
33 1069 assisted transformation of chrysotile to antigorite—An example from Guatemala.
34
35 1070 *Chemical Geology* 284(3), 351-362.
36
37 1071 Kodolányi, J., Pettke, T., Spandler, C., Kamber, B.S. & Gméling, K. (2012). Geochemistry of
38
39 1072 ocean floor and fore-arc serpentinites: constraints on the ultramafic input to
40
41 1073 subduction zones. *Journal of Petrology* 53(2), 235-270.
42
43 1074 Koschinsky, A., & Hein, J. R. (2003). Uptake of elements from seawater by ferromanganese
44
45 1075 crusts: Solid-phase associations and seawater speciation. *Marine Geology*, 198(3–4),
46
47 1076 331–351.
48
49 1077 Lafay, R., Deschamps, F., Schwartz, S., Guillot, S., Godard, M., Debret, B. and Nicollet, C.
50
51 1078 (2013). High-pressure serpentinites, a trap-and-release system controlled by
52
53
54
55
56
57
58
59
60

- 1
2
3 1079 metamorphic conditions: Example from the piedmont zone of the western alps.
4
5 1080 Chemical Geology 343, 38–54.
6
7 1081 Langmuir, D. (1978). Uranium solution-mineral equilibria at low temperatures with
8
9 1082 applications to sedimentary ore deposits. *Geochimica et Cosmochimica Acta*, 42(6),
10
11 1083 547–569.
12
13 1084 Li, X.-P., Rahn, M. & Bucher, K. (2004). Serpentinites of the Zermatt Saas ophiolite complex
14
15 1085 and their texture evolution. *Journal of Metamorphic Geology* 22(3), 159–177.
16
17 1086 Li, Y.H. (1982). A brief discussion on the mean oceanic residence time of
18
19 1087 elements. *Geochimica et Cosmochimica Acta* 46(12), 2671-2675.
20
21 1088 Sánchez-Vizcaíno, V.L., Gómez-Pugnaire, M.T., Garrido, C.J., Padrón-Navarta, J.A. &
22
23 1089 Mellini, M. (2009). Breakdown mechanisms of titanclinohumite in antigorite
24
25 1090 serpentinite (Cerro del Almirez massif, S. Spain): A petrological and TEM study.
26
27 1091 *Lithos* 107(3), 216-226.
28
29 1092 Marschall, H.R., Wanless, V.D., Shimizu, N., von Strandmann, P.A.P., Elliott, T. &
30
31 1093 Monteleone, B.D. (2017). The boron and lithium isotopic composition of mid-ocean
32
33 1094 ridge basalts and the mantle. *Geochimica et Cosmochimica Acta* 207, 102-138.
34
35 1095 McDonough, W.F. & Sun, S.S. (1995). The composition of the Earth. *Chemical geology*
36
37 1096 120(3-4), 223-253.
38
39 1097 Mohajerin, T. J., Helz, G. R., & Johannesson, K. H. (2016). Tungsten-molybdenum
40
41 1098 fractionation in estuarine environments. *Geochimica et Cosmochimica Acta*, 177,
42
43 1099 105–119.
44
45 1100 Müntener, O., Pettke, T., Desmurs, L., Meier, M. & Schaltegger, U. (2004). Refertilization of
46
47 1101 mantle peridotite in embryonic ocean basins: trace element and Nd isotopic evidence
48
49 1102 and implications for crust–mantle relationships. *Earth and Planetary Science Letters*
50
51 1103 221(1), 293-308.
52
53
54
55
56
57
58
59
60

- 1
2
3 1104 Niu, Y. (2004). Bulk-rock major and trace element compositions of abyssal peridotites:
4
5 1105 implications for mantle melting, melt extraction and post-melting processes beneath
6
7 1106 mid-ocean ridges. *Journal of Petrology* 45(12), 2423-2458.
8
- 9 1107 Paulick, H., Bach, W., Godard, M., De Hoog, J.C.M., Suhr, G. & Harvey, J. (2006).
10
11 1108 Geochemistry of abyssal peridotites (Mid-Atlantic Ridge, 15 20' N, ODP Leg 209):
12
13 1109 implications for fluid/rock interaction in slow spreading environments. *Chemical*
14
15 1110 *Geology* 234(3), 179-210.
16
- 17 1111 Pelletier, L. & Müntener, O. (2006). High-pressure metamorphism of the Lanzo peridotite
18
19 1112 and its oceanic cover, and some consequences for the Sesia–Lanzo zone (north-
20
21 1113 western Italian Alps). *Lithos*, 90(1), 111-130.
22
- 23 1114 Peters, D. & Pettke, T. (2017). Evaluation of Major to Ultra Trace Element Bulk Rock
24
25 1115 Chemical Analysis of Nanoparticulate Pressed Powder Pellets by LA-ICP-
26
27 1116 MS. *Geostandards and Geoanalytical Research* 41(1), 5-28.
28
- 29 1117 Peters, D., Bretscher, A., John, T., Scambelluri, M. & Pettke, T. (2017). Fluid-mobile
30
31 1118 elements in serpentinites: Constraints on serpentinitization environments and element
32
33 1119 cycling in subduction zones. *Chemical Geology* 466, 654-666.
34
- 35 1120 Pettke, T., Oberli, F., Audétat, A., Guillong, M., Simon, A.C., Hanley, J. J. & Klemm, L.M.
36
37 1121 (2012). Recent developments in element concentration and isotope ratio analysis of
38
39 1122 individual fluid inclusions by laser ablation single and multiple collector ICP-MS. *Ore*
40
41 1123 *Geology Reviews* 44, 10-38.
42
- 43 1124 Piccardo, G.B. (2008). The Jurassic Ligurian Tethys, a fossil ultraslow-spreading ocean: the
44
45 1125 mantle perspective. *Geological Society, London, Special Publications* 293(1), 11-34.
46
- 47 1126 Plank, T. (2014). The chemical composition of subducting sediments. *Treatise on*
48
49 1127 *geochemistry* 4, 607-629.
50
51
52
53
54
55
56
57
58
59
60

- 1
2
3 1128 Rampone, E. & Piccardo, G.B. (2000). The ophiolite-oceanic lithosphere analogue: new
4
5 1129 insights from the Northern Apennines (Italy). SPECIAL PAPERS-GEOLOGICAL
6
7 1130 SOCIETY OF AMERICA, 21-34.
8
9 1131 Rampone, E., Romairone, A. & Hofmann, A.W. (2004). Contrasting bulk and mineral
10
11 1132 chemistry in depleted mantle peridotites: evidence for reactive porous flow. Earth and
12
13 1133 Planetary Science Letters 218(3), 491-506.
14
15 1134 Rampone, E., Borghini, G., Romairone, A., Abouchami, W., Class, C. & Goldstein, S.L.
16
17 1135 (2014). Sm–Nd geochronology of the Erro-Tobbio gabbros (Ligurian Alps, Italy):
18
19 1136 insights into the evolution of the Alpine Tethys. Lithos 205, 236-246.
20
21 1137 Ranero, C. & Sallares, V. (2004). Geophysical evidence for hydration of the crust and mantle
22
23 1138 of the Nazca plate during bending at the North Chile trench. Geology 32(7), 549–552.
24
25 1139 Rebay, G., Spalla, M. & Zanoni, D. (2012). Interaction of deformation and metamorphism
26
27 1140 during subduction and exhumation of hydrated oceanic mantle: Insights from the
28
29 1141 Western Alps. Journal of Metamorphic Geology 30(7), 687–702.
30
31 1142 Rebay, G., Zanoni, D., Langone, A., Luoni, P., Tiepolo, M. & Spalla, M.I. (2017). Dating of
32
33 1143 ultramafic rocks from the Western Alps ophiolites discloses Late Cretaceous
34
35 1144 subduction ages in the Zermatt-Saas Zone. Geological Magazine, 1-18.
36
37 1145 Reddy, S., Wheeler, J. & Cliff, R. (1999). The geometry and timing of orogenic extension: an
38
39 1146 example from the Western Italian Alps. Journal of Metamorphic Geology 17, 573–
40
41 1147 590.
42
43 1148 Rehka, M. & Hofmann, A.W. (1997). Recycled ocean crust and sediment in Indian Ocean
44
45 1149 MORB. Earth and Planetary Science Letters 147(1), 93-106.
46
47 1150 Reinecke, T. (1991). Very-high-pressure metamorphism and uplift of coesite-bearing
48
49 1151 metasediments from the Zermatt-Saas Zone, Western Alps. European Journal of
50
51 1152 Mineralogy, 7–18.
52
53
54
55
56
57
58
59
60

- 1
2
3 1153 Reinecke, T. (1998). Prograde high-to ultrahigh-pressure metamorphism and exhumation of
4
5 1154 oceanic sediments at Lago di Cignana, Zermatt-Saas Zone, Western Alps. *Lithos*
6
7 1155 42(3), 147–189.
8
9 1156 Reynard, B. (2013). Serpentine in active subduction zones. *Lithos* 178, 171–185.
10
11 1157 Rubatto, D., Gebauer, D. & Fanning, M. (1998). Jurassic formation and Eocene subduction of
12
13 1158 the Zermatt–Saas-Fee ophiolites: implications for the geodynamic evolution of the
14
15 1159 Central and Western Alps. *Contributions to Mineralogy and Petrology* 132(3), 269–
16
17 1160 287.
18
19
20 1161 Rudnick, R.L. & Gao, S. (2003). Composition of the continental crust. *Treatise on*
21
22 1162 *geochemistry* 3, 659.
23
24 1163 Rüpke, L. H., Morgan, J. P., Hort, M., & Connolly, J. A. (2004). Serpentine and the
25
26 1164 subduction zone water cycle. *Earth and Planetary Science Letters*, 223(1), 17-34.
27
28 1165 Ryan, J. & Chauvel, C. (2014). 3.13 - the subduction-zone filter and the impact of recycled
29
30 1166 materials on the evolution of the mantle. In: Holland, H. D., Turekian, K. K. (Eds.),
31
32 1167 *Treatise on Geochemistry (Second Edition)*, second edition. Elsevier, Oxford, pp. 479
33
34 1168 – 508.
35
36
37 1169 Sánchez-Vizcaíno, V.L., Trommsdorff, V., Gómez-Pugnaire, M., Garrido, C., Müntener, O.
38
39 1170 & Connolly, J. (2005). Petrology of titanian clinohumite and olivine at the high-
40
41 1171 pressure breakdown of antigorite serpentinite to chlorite harzburgite (Almirez Massif,
42
43 1172 S. Spain). *Contributions to Mineralogy and Petrology* 149(6), 627–646.
44
45
46 1173 Savov, I.P., Ryan, J.G., D’Antonio, M., Kelley, K. & Mattie, P. (2005). Geochemistry of
47
48 1174 serpentinitized peridotites from the Mariana forearc conical seamount, ODP leg 125:
49
50 1175 Implications for the elemental recycling at subduction zones. *Geochemistry,*
51
52 1176 *Geophysics, Geosystems* 6(4).

- 1
2
3 1177 Scambelluri, M. & Philippot, P. (2001). Deep fluids in subduction zones. *Lithos* 55(1), 213-
4
5 1178 227.
6
7 1179 Scambelluri, M. & Rampone, E. (1999). Mg-metasomatism of oceanic gabbros and its
8
9 1180 control on Ti-clinohumite formation during eclogitization. *Contributions to*
10
11 1181 *Mineralogy and Petrology*, 135(1), 1-17.
12
13 1182 Scambelluri, M. & Tonarini, S. (2012). Boron isotope evidence for shallow fluid transfer
14
15 1183 across subduction zones by serpentinized mantle. *Geology* 40(10), 907–910.
16
17 1184 Scambelluri, M., Müntener, O., Hermann, J., Piccardo, G.B. & Trommsdorff, V. (1995).
18
19 1185 Subduction of water into the mantle: history of an alpine peridotite. *Geology* 23(5),
20
21 1186 459–462.
22
23 1187 Scambelluri, M., Müntener, O., Ottolini, L., Pettke, T.T. & Vannucci, R. (2004). The fate of
24
25 1188 B, Cl and Li in the subducted oceanic mantle and in the antigorite breakdown fluids.
26
27 1189 *Earth and Planetary Science Letters* 222(1), 217–234.
28
29 1190 Scambelluri, M., Pettke, T., Rampone, E., Godard, M. & Reusser, E. (2014). Petrology and
30
31 1191 trace element budgets of high-pressure peridotites indicate subduction dehydration of
32
33 1192 serpentized mantle (Cima di Gagnone, Central Alps, Switzerland). *Journal of*
34
35 1193 *Petrology* 55(3), 459–498.
36
37 1194 Scambelluri, M., Pettke, T. & Cannà, E. (2015). Fluid-related inclusions in Alpine high-
38
39 1195 pressure peridotite reveal trace element recycling during subduction-zone dehydration
40
41 1196 of serpentized mantle (Cima di Gagnone, Swiss Alps). *Earth and Planetary Science*
42
43 1197 *Letters* 429, 45–59.
44
45 1198 Schmidt, M.W. & Poli, S. (1998). Experimentally based water budgets for dehydrating slabs
46
47 1199 and consequences for arc magma generation. *Earth and Planetary Science Letters*
48
49 1200 163(1), 361–379.
50
51
52
53
54
55
56
57
58
59
60

- 1
2
3 1201 Schwartz, S., Allemand, P., & Guillot, S. (2001). Numerical model of the effect of
4
5 1202 serpentinites on the exhumation of eclogitic rocks: insights from the Monviso
6
7 1203 ophiolitic massif (Western Alps). *Tectonophysics*, 342(1), 193-206.
8
9 1204 Shen, T., Hermann, J., Zhang, L., Lü, Z., Padrón-Navarta, J.A., Xia, B. & Bader, T. (2015).
10
11 1205 UHP metamorphism documented in Ti-chondrodite-and Ti-clinohumite-bearing
12
13 1206 serpentinitized ultramafic rocks from Chinese Southwestern Tianshan. *Journal of*
14
15 1207 *Petrology* 56(7), 1425–1458.
16
17
18 1208 Skora, S., Mahlen, N., Johnson, C., Baumgartner, L., Lapen, T., Beard, B. & Szilvagy, E.
19
20 1209 (2015). Evidence for protracted prograde metamorphism followed by rapid
21
22 1210 exhumation of the Zermatt-Saas Fee ophiolite. *Journal of Metamorphic Geology*
23
24 1211 33(7), 711–734.
25
26 1212 Snow, J. E., & Dick, H. J. B. (1995). Pervasive magnesium loss by marine weathering of
27
28 1213 peridotite. *Geochimica et Cosmochimica Acta*, 59(20), 4219–4235.
29
30
31 1214 Spandler, C. & Pirard, C. (2013). Element recycling from subducting slabs to arc crust: A
32
33 1215 review. *Lithos* 170, 208-223.
34
35 1216 Tartarotti, P., Festa, A., Benciolini, L. & Balestro, G. (2017). Record of Jurassic mass
36
37 1217 transport processes through the orogenic cycle: Understanding chaotic rock units in
38
39 1218 the high-pressure Zermatt-Saas ophiolite (Western Alps). *Lithosphere* 9(3), 399-407.
40
41 1219 Todt, W., Cliff, R. A., Hanser, A. & Hofmann, A.W. (1996). Evaluation of a ^{202}Pb – ^{205}Pb
42
43 1220 Double Spike for High Precision Lead Isotope Analysis. *Earth processes: reading the*
44
45 1221 isotopic code, 429-437.
46
47
48 1222 Ulmer, P. & Trommsdorff, V. (1995). Serpentine stability to mantle depths and subduction-
49
50 1223 related magmatism. *Science* 268 (5212), 858–861.
51
52
53
54
55
56
57
58
59
60

- 1
2
3 1224 Vils, F., Tonarini, S., Kalt, A. & Seitz, H.M. (2009). Boron, lithium and strontium isotopes as
4
5 1225 tracers of seawater–serpentinite interaction at Mid-Atlantic ridge, ODP Leg
6
7 1226 209. *Earth and Planetary Science Letters* 286(3), 414-425.
8
9 1227 Weber, S. & Bucher, K. (2015). An eclogite-bearing continental tectonic slice in the Zermatt–
10
11 1228 Saas high-pressure ophiolites at Trockener Steg (Zermatt, Swiss Western Alps).
12
13 1229 *Lithos* 232, 336–359.
14
15 1230 Zanoni, D., Rebay, G., Bernardoni, J. & Spalla, M.I. (2012). Using multiscale structural
16
17 1231 analysis to infer high-/ultrahigh-pressure assemblages in subducted rodingites of the
18
19 1232 Zermatt-Saas Zone at Valtournanche, Italy. *Journal of the Virtual Explorer* 41, 2-30.
20
21 1233 Zanoni, D., Rebay, G. & Spalla, M.I. (2016). Ocean floor and subduction record in the
22
23 1234 Zermatt–Saas rodingites, Valtournanche, Western Alps. *Journal of Metamorphic*
24
25 1235 *Geology* 34(9), 941-961.
26
27
28
29 1236
30
31
32
33
34
35
36
37
38
39
40
41
42
43
44
45
46
47
48
49
50
51
52
53
54
55
56
57
58
59
60

1
2
3 1237 **Figures:**
4

- 5
6 1238 1) Simplified geological sketch and block diagram of the Western Alps around the
7
8 1239 Zermatt–Saas Zone (redrawn after **Dal Piaz, 1992**). **Upper Austroalpine outliers:**
9
10 1240 DB = Dent Blanche, VP = Valpelline Unit, MM = Mt. Mary, P = Pillonet; **Sesia-**
11
12 1241 **Lanzo Inliers (SL):** II–DK = Dioritic–kinzigitic, Gm = Gneiss Minuti, Emc =
13
14 1242 Eclogitic Micascist; **Inner Penninic:** MR = Monte Rosa, AB = Arcesa–Brusson, GP
15
16 1243 = Gran Paradiso; **Mid Penninic:** SB = Grand St. Bernard; **Outer Penninic:** VA =
17
18 1244 Valais Zone, PF = Penninic Front; **Helvetic (HE):** MB = Mt. Blanc; **Piemonte Zone:**
19
20 1245 CO = Combin, ZS = Zermatt–Saas, A = Atrona; **Lower Austroalpine Outliers:** EM
21
22 1246 = Mt. Emilius, GR = Glacier–Rafraay, S = Santanel, TP = Tour Ponton, AR = Acque
23
24 1247 Rosse, E = Etirol–Levaz, C = Lago di Cignana Unit, Ch = Chatillon, SV = St.
25
26 1248 Vincent; **major Alpine faults:** SF = Simplon Fault, CL = Canavese Line, ARF =
27
28 1249 Aosta–Ranzola Fault.
29
30
31 1250 2) Simplified geologic sketch and profile (A–A'–A'') of the Lago di Cignana Unit,
32
33 1251 modified after **Forster et al. (2004)** and **Groppo et al. (2009)**. (1) Austroalpine
34
35 1252 domain (Arolla Unit), (2) Combine Zone, (3) Pancherot Unit. Zermatt–Saas Zone: (4)
36
37 1253 Prasitites with eclogites, (5) Mg–Al metagabbros, (6) UHP Fe–Ti gabbros and
38
39 1254 metasediments of the Lago di Cignana Unit and (7) serpentinites.
40
41
42 1255 3) PT path for the Lago di Cignana Unit (**Groppo et al., 2009**) and geothermobarometric
43
44 1256 estimates for the Zermatt–Saas Zone eclogites (**Angiboust et al., 2009; Groppo et**
45
46 1257 **al., 2009**) and serpentinites (**Rebay et al., 2012**).
47
48
49 1258 4) Representative microstructures of Zermatt (a, b, c) and Cignana (d, e, f, g, h.)
50
51 1259 serpentinites and Ti–rich veins. **Zermatt serpentinite:** (a.) HP foliation in the
52
53 1260 Zermatt serpentinite wrapping a relic of mantle clinopyroxene; (b.) serpentinite with
54
55 1261 bastite after mantle pyroxene; (c.) fragment of Ti–clinohumite + olivine + magnetite
56
57
58
59
60

- 1
2
3 1262 vein embedded in serpentinite. **Cignana serpentinite**: (d.) Cignana serpentinite
4
5 1263 displaying a main foliation defined by elongated domains of HP metamorphic rock–
6
7 1264 forming olivine and metamorphic diopside; (e.) type 1 Ti–clinohumite vein hosting
8
9 1265 large (3–5 mm) crystals of olivine, Ti–clinohumite, chlorite, diopside and magnetite;
10
11 1266 (f.) type 2 Ti–chondrodite vein. Ti–chondrodite occurs with chlorite as 0.5–1 mm–
12
13 1267 sized, isolated crystals, filled with solid inclusions of ilmenite, zircon and REE–
14
15 1268 bearing phases. Finer Ti–clinohumite crystals grow at the expense of former Ti–
16
17 1269 chondrodite; (g.) mm–sized aggregates of apatite rich in solid and fluid inclusions;
18
19 1270 (h.) Metamorphic diopside crystals containing elongated fluid inclusions.
20
21
22 1271 5) Representative microstructures from the Lago di Cignana Unit. (a.) Coesite–bearing
23
24 1272 eclogite. An omphacite + rutile foliation wraps around large, inclusion-bearing garnet
25
26 1273 porphyroclasts. Coesite occurs as inclusion in garnet; (b.) Coesite–bearing garnet and
27
28 1274 tourmaline quartzite. Note the large poikiloblasts of garnet and tourmaline with quartz
29
30 1275 inclusions; (c.) Coesite– and microdiamond–bearing garnet Mn–quartzite; (d.) Coesite
31
32 1276 inclusion in garnet from Mn–quartzite; (e.) Phengite, epidote and calcite from a garnet
33
34 1277 calcschist; (f.) Poikilitic garnet porphyroclast with quartz inclusions in garnet
35
36 1278 calcschist.
37
38
39 1279 6) Major element plots (FeO vs MgO and Al₂O₃ vs CaO) for the Zermatt serpentinites
40
41 1280 and for the Cignana serpentinites and veins. FeO vs MgO: contours are Mg# = molar
42
43 1281 Mg/(Mg+Fe). Al₂O₃ vs CaO: the shaded areas refer to the mantle depletion trend.
44
45
46 1282 7) Cr vs Ni plot for the Zermatt serpentinites and for the Cignana serpentinites and veins.
47
48 1283 Shaded areas are for Alpine eclogites (Cignana, this work; Monviso, **Angiboust et al.,**
49
50 1284 **2012**), gabbroic dykelets (Voltri, **Scambelluri & Rampone, 1999**), and peridotites
51
52 1285 (Lanzo, **Müntener et al., 2004; Guarnieri et al., 2012**). Note that the Ti–chondrodite
53
54
55
56
57
58
59
60

1
2
3 1286 (orange diamond) and the Ti-clinohumite veins (yellow diamonds) fall within the
4
5 1287 peridotite area.

6
7 1288 8) C1 Chondrite-normalized (**McDonough and Sun, 1995**) REE patterns of bulk-rock
8
9 1289 from eclogite and metasediments from the UHP Lago di Cignana Unit, Cignana and
10
11 1290 Zermatt serpentinites and Cignana Ti-bearing veins. Shaded areas are for fresh
12
13 1291 plagioclase peridotite (orange) and spinel harzburgites (blue) from the Lanzo Massif
14
15 1292 (**Guarneri et al, 2012**)).

16
17
18 1293 9) PM-normalized (**McDonough and Sun, 1995**; B and Li after **Marschall et al., 2017**)
19
20 1294 TE patterns of bulk-rock (PPP data used from Table 1) from eclogite and
21
22 1295 metasediments from the UHP Lago di Cignana Unit, Cignana and Zermatt
23
24 1296 serpentinites, and Cignana Ti-bearing veins. Shaded areas are for fresh plagioclase
25
26 1297 peridotite from the Lanzo Massif (orange; **Guarneri et al, 2012**) and the mantle
27
28 1298 depletion trend (blue).

29
30
31 1299 10) $^{206}\text{Pb}/^{204}\text{Pb}$ and $^{87}\text{Sr}/^{86}\text{Sr}$ values of analysed samples from the Lago di Cignana Unit,
32
33 1300 Cignana serpentinites and veins and Zermatt serpentinites. Values from GLOSS-II
34
35 1301 (**Plank, 2014**), depleted mantle (**Rehka & Hofmann, 1997**), Jurassic seawater (**Jones**
36
37 1302 **& Jenkyns, 2001**) and average continental crust (**Rudnick and Gao, 2003**) are
38
39 1303 reported for comparison.

40
41
42 1304 11) Mineral analyses of serpentine and olivine from the Zermatt serpentinite, the Cignana
43
44 1305 serpentinite, and the Ti-bearing veins. Serpentine from Zermatt has higher Mg# and
45
46 1306 lower Al content than serpentine from Cignana. Mg# in Zermatt olivine is comparable
47
48 1307 with serpentine from the same locality. Olivine from the Cignana serpentinite and Ti-
49
50 1308 clinohumite vein have similar Mg#, lower than in the Zermatt serpentinite.

51
52
53 1309 12) Mineral analyses of Ti-chondrodite and Ti-clinohumite from the Cignana serpentinite
54
55 1310 veins and from the Zermatt serpentinite. Note the lower Ti content of both Ti-

- 1
2
3 1311 chondrodite and Ti-clinohumite from the Zermatt-serpentinite with respect to
4
5 1312 Cignana serpentinite veins. Mineral analyses from **Scambelluri & Rampone (1999)**
6
7 1313 and **Shen et al., (2014)** reported for comparison.
8
9 1314 13) REE and TE composition of antigorite, diopside, Ti-clinohumite and apatite from the
10
11 1315 Cignana and Zermatt serpentinites.
12
13 1316 14) Pressure-Temperature diagram with the stability field of Ti-clinohumite (light
14
15 orange) and Ti-chondrodite (dark orange) in serpentinite systems. The main reaction
16 1317 lines involving Ti-clinohumite and Ti-chondrodite and the quartz to coesite transition
17
18 1318 lines are from **Shen et al. (2015)**. The black arrow corresponds to the PT path of the
19
20 1319 Lago di Cignana Unit (**Groppo et al., 2009**). The dashed grey lines are the
21
22 1320 geothermal gradients for cold (5–7 °C/km) and hot (20 °C/km) subduction. Cignana
23
24 1321 type 1 veins formed during the prograde path, after the partial dehydration of the
25
26 1322 Cignana serpentinite. Type 2 veins formed at peak UHP conditions, in the stability
27
28 1323 field of Ti-chondrodite. Type 1 and 2 veins recrystallized during retrograde
29
30 1324 decompression in the stability field of Ti-clinohumite.
31
32 1325
33
34 1326 15) Petrogenetic sequence summarizing and comparing the overall evolution of the
35
36 1327 Zermatt and Cignana serpentinite and the Lago di Cignana Unit.
37
38 1328 16) As vs Sb, Sr vs B, and U vs Th plots of analysed samples from the Lago di Cignana
39
40 1329 Unit, Cignana serpentinites and veins and Zermatt serpentinites. Shaded area from
41
42 1330 Voltri (**Cannaò et al., 2016**), Cima di Gagnone (CdG; **Scambelluri et al., 2014**;
43
44 1331 **Cannaò et al., 2015**), Subduction zone (SZ serp) and abyssal serpentinites
45
46 1332 (**Deschamps et al., 2013** and references therein) and Lanzo peridotite (**Guarnieri et**
47
48 1333 **al., 2012**).
49
50
51 1334 17) Initial $^{206}\text{Pb}/^{204}\text{Pb}$ vs $^{87}\text{Sr}/^{86}\text{Sr}$, shows a mixing line between Zermatt serpentinite and a
52
53 1335 fluid of composition comparable with Cignana eclogite (Sample LCG1401), Continental
54
55
56
57
58
59
60

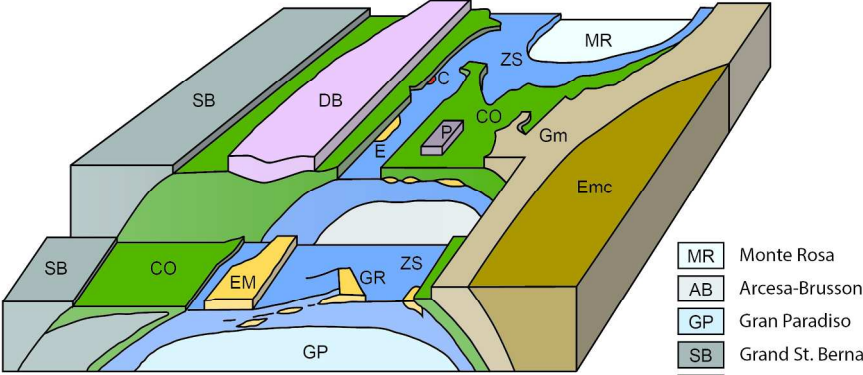
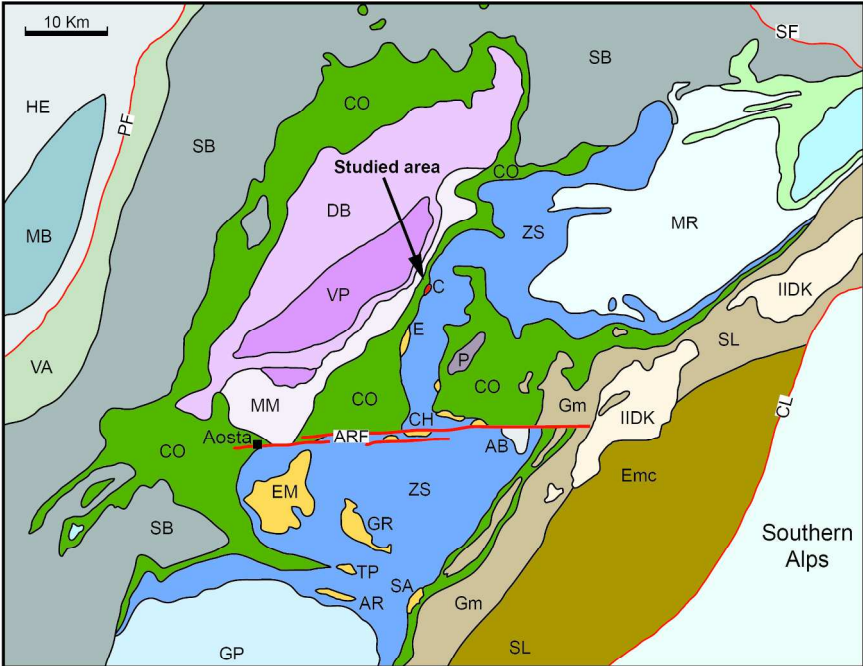
1
2
3 1336 Crust (**Rudnick and Gao, 2003**) and GLOSS-II (Plank, 2014). Shaded area from Voltri
4
5 1337 (**Cannaò et al., 2016**), Cima di Gagnone (CdG; **Cannaò et al., 2015**). Values from
6
7 1338 GLOSS-II (**Plank, 2014**), depleted mantle (**Rehka & Hofmann, 1997**), Jurassic seawater
8
9 1339 (**Jones & Jenkyns, 2001**), and average continental crust (**Rudnick and Gao, 2003**) are
10
11 1340 reported for comparison.

1341 **Tables**

- 1342 1) Lists of collected samples and mineral assemblages of the Lago di Cignana Unit and
1343 of the Cignana and Zermatt serpentinite.
- 1344 2) Major (wt.%) and Trace element ($\mu\text{g/g}$) composition of eclogite and metasediments
1345 from the Lago di Cignana Unit, Cignana serpentinites and Ti-bearing veins and of
1346 Zermatt serpentinite. Samples were analysed for major elements (d.l. = 0.01 wt.%)
1347 and V (d.l. 5 $\mu\text{g/g}$), Be, Sr, Zr (d.l. 2 $\mu\text{g/g}$), Sc, Y, and Ba (d.l. 1 $\mu\text{g/g}$) by means of
1348 Fusion-ICP-MS at Act-Lab, Canada. Trace elements were analysed by liquid ICP-MS
1349 at Geosciences Montpellier (France). Detection limits can be found in **Godard et al.**
1350 (**2000**). Furthermore, all samples were analysed for major and trace element by PPP-
1351 LA-ICP-MS at the University of Bern.
- 1352 3) Pb and Sr isotopic composition of selected samples from the Lago di Cignana Unit,
1353 the Cignana serpentinite and the Zermatt-Saas Zone serpentinite. All values are
1354 reported as observed (obs.) and as corrected (corr.) for an age of 40 Ma.
- 1355 4) Representative electron microprobe analyses of mineral phases from the UHP eclogite
1356 of the Lago di Cignana Unit.
- 1357 5) Representative electron microprobe analyses of mineral phases from the UHP
1358 quartzite of the Lago di Cignana Unit.
- 1359 6) Representative electron microprobe analyses of mineral phases from the UHP
1360 calcschist of the Lago di Cignana Unit.

- 1
2
3 1361 7) Representative electron microprobe analyses of mineral phases from the Cignana
4
5 1362 serpentinite.
6
7 1363 8) Representative electron microprobe analyses of mineral phases from Ti–chondrodite
8
9 1364 and Ti–clinohumite veins hosted within Cignana serpentinite.
10
11 1365 9) Representative electron microprobe analyses of mineral phases from the Zermatt
12
13 1366 serpentinite.
14
15 1367 10) Representative laser ablation in–situ trace element analyses of mineral phases from
16
17 1368 the UHP eclogite and metasediments of the Lago di Cignana Unit. All data are
18
19 1369 reported in $\mu\text{g/g}$.
20
21 1370 11) Representative laser ablation in–situ trace element analyses of mineral phases from
22
23 1371 the Cignana serpentinite. All data are reported in $\mu\text{g/g}$.
24
25 1372 12) Representative laser ablation in–situ trace element analyses of mineral phases from
26
27 1373 Ti–chondrodite and Ti–clinohumite veins hosted in the Cignana serpentinite. All data
28
29 1374 are reported in $\mu\text{g/g}$.
30
31 1375 13) Representative laser ablation in–situ trace element analyses of mineral phases from
32
33 1376 the Zermatt serpentinite. All data are reported in $\mu\text{g/g}$.
34
35
36
37
38
39
40
41
42
43
44
45
46
47
48
49
50
51
52
53
54
55
56
57
58
59
60

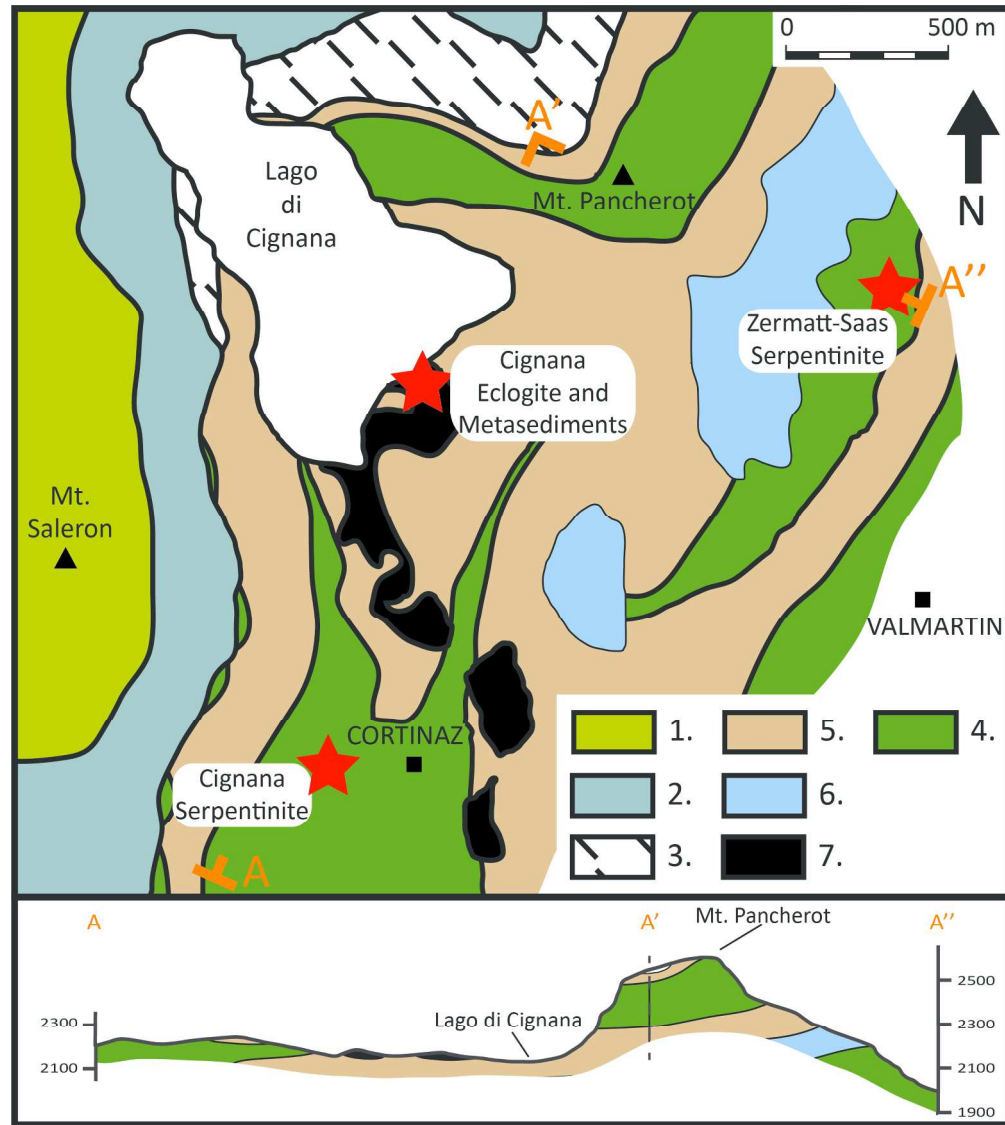
1
2
3
4
5
6
7
8
9
10
11
12
13
14
15
16
17
18
19
20
21
22
23
24
25
26
27
28
29
30
31
32
33
34
35
36
37
38
39
40
41
42
43
44
45
46
47
48
49
50
51
52
53
54
55
56
57
58
59
60



- | | | | |
|---|---|---|---|
| DB Dent Blanche | IIDK IIDK | CO Combin Zone | MR Monte Rosa |
| VP Valpelline unit | Gm Gneiss Minuti | ZS Zermatt-Saas Zone | AB Arcesa-Brusson |
| MM Mont Mary | Emc Eclogitic Micaschists | A Atrona | GP Gran Paradiso |
| P Pillonet | Lower Australpine Outliers | | SB Grand St. Bernard |
| | | | VA Valais Zone |
| | | | MB Mont Blanc |
| | | | Southern Alps |

Figure 1 - Simplified geological sketch and block diagram of the Western Alps around the Zermatt-Saas Zone (redrawn after Dal Piaz, 1992). Upper Austroalpine outliers: DB = Dent Blanche, VP = Valpelline Unit, MM = Mt. Mary, P = Pillonet; Sesia-Lanzo Inliers (SL): II-DK = Dioritic-kinzigitic, Gm = Gneiss Minuti, Emc = Eclogitic Micaschist; Inner Penninic: MR = Monte Rosa, AB = Arcesa-Brusson, GP = Gran Paradiso; Mid Penninic: SB = Grand St. Bernard; Outer Penninic: VA = Valais Zone, PF = Penninic Front; Helvetic (HE): MB = Mt. Blanc, Piemonte Zone: CO = Combin, ZS = Zermatt-Saas, A = Atrona; Lower Austroalpine Outliers: EM = Mt. Emilius, GR = Glacier-Rafra, S = Santanel, TP = Tour Ponton, AR = Acque Rosse, E = Etirol-Levaz, C = Lago di Cignana Unit, Ch = Chatillon, SV = St. Vincent; major Alpine faults: SF = Simplon Fault, CL = Canavese Line, ARF = Aosta-Ranzola Fault.

197x261mm (300 x 300 DPI)



43 Figure 2 - Simplified geologic sketch and profile (A-A'-A'') of the Lago di Cignana Unit, modified after
 44 Forster et al. (2004) and Groppo et al. (2009). (1) Austroalpine domain (Arolla Unit), (2) Combine Zone, (3)
 45 Pancherot Unit. Zermatt-Saas Zone: (4) Prasinites with eclogites, (5) Mg-Al metagabbros, (6) UHP Fe-Ti
 46 gabbros and metasediments of the Lago di Cignana Unit and (7) serpentinites.

47 211x237mm (300 x 300 DPI)

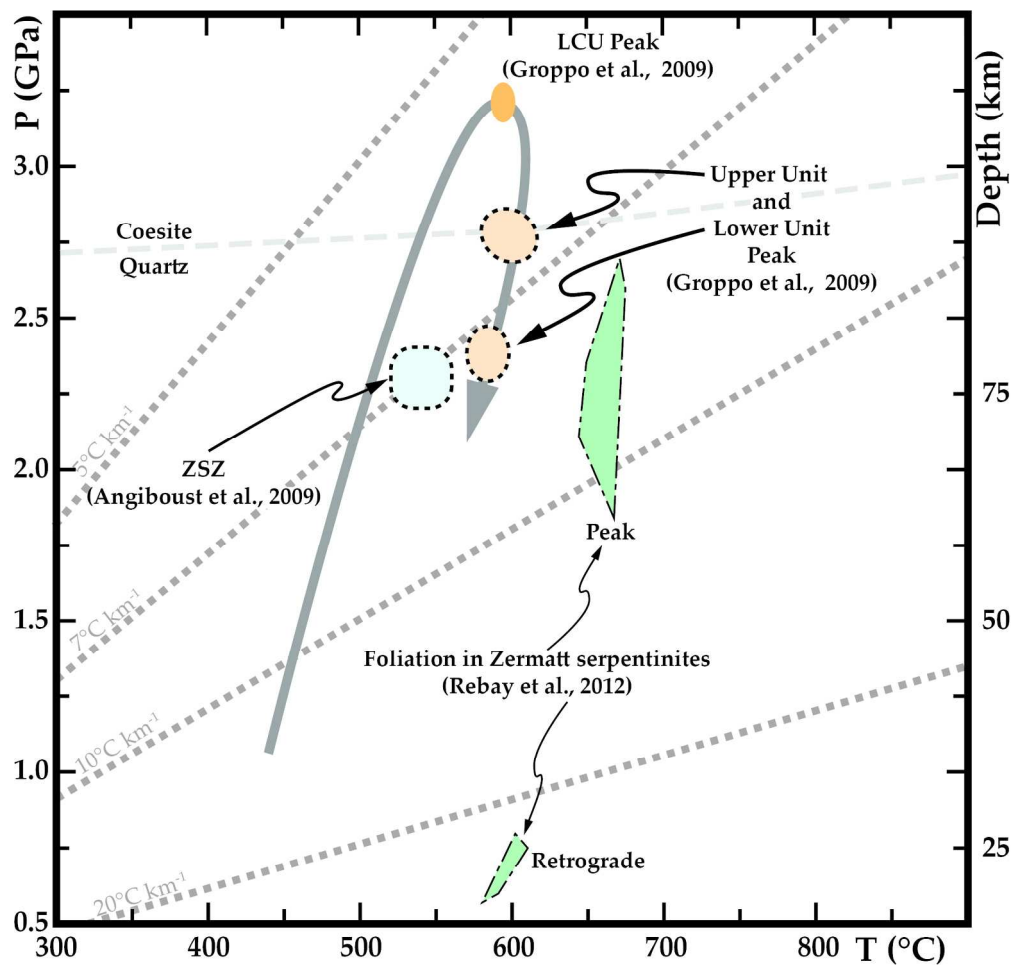


Figure 3 - PT path for the Lago di Cignana Unit (Groppo et al., 2009) and geothermobarometric estimates for the Zermatt-Saas Zone eclogites (Angiboust et al., 2009; Groppo et al., 2009) and serpentinites (Rebay et al., 2012).

187x180mm (300 x 300 DPI)

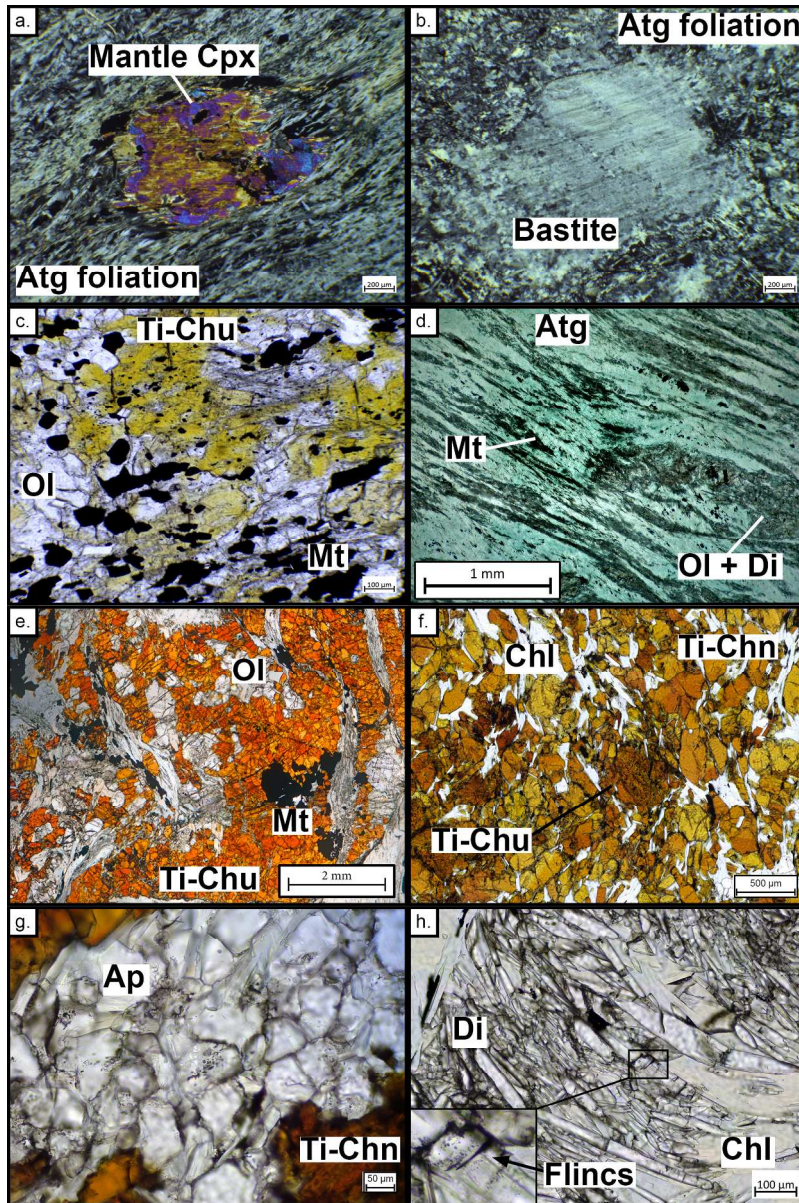


Figure 4 - Representative microstructures of Zermatt (a., b. and c.) and Cignana (d., e., f., g. and h.) serpentinites and Ti-rich veins. Zermatt serpentinite: (a.) HP foliation in the Zermatt serpentinite wrapping a relic of mantle clinopyroxene; (b.) serpentinite with bastite after mantle pyroxene and serpentine + magnetite mesh structure after mantle olivine; (c.) fragment of Ti-clinohumite + olivine + magnetite vein embedded in serpentinite. Cignana serpentinite: (d.) Cignana serpentinite displaying a main foliation defined by elongated domains of HP metamorphic rock-forming olivine and diopside; (e.) type 1 Ti-clinohumite vein hosting large (3–5 mm) crystals of olivine, Ti-clinohumite, chlorite, diopside and magnetite; (f.) type 2 Ti-chondrodite vein. Ti-chondrodite occurs with chlorite as 0.5–1 mm-sized, isolated crystals, filled with solid inclusions of ilmenite, zircon and REE-bearing phases. Finer Ti-clinohumite crystals grow at the expenses of former Ti-chondrodite; (g.) mm-sized aggregates of apatite rich in solid and fluid inclusions; (h.) Diopside crystals containing elongated fluid inclusions.

180x270mm (300 x 300 DPI)

1
2
3
4
5
6
7
8
9
10
11
12
13
14
15
16
17
18
19
20
21
22
23
24
25
26
27
28
29
30
31
32
33
34
35
36
37
38
39
40
41
42
43
44
45
46
47
48
49
50
51
52
53
54
55
56
57
58
59
60

For Peer Review

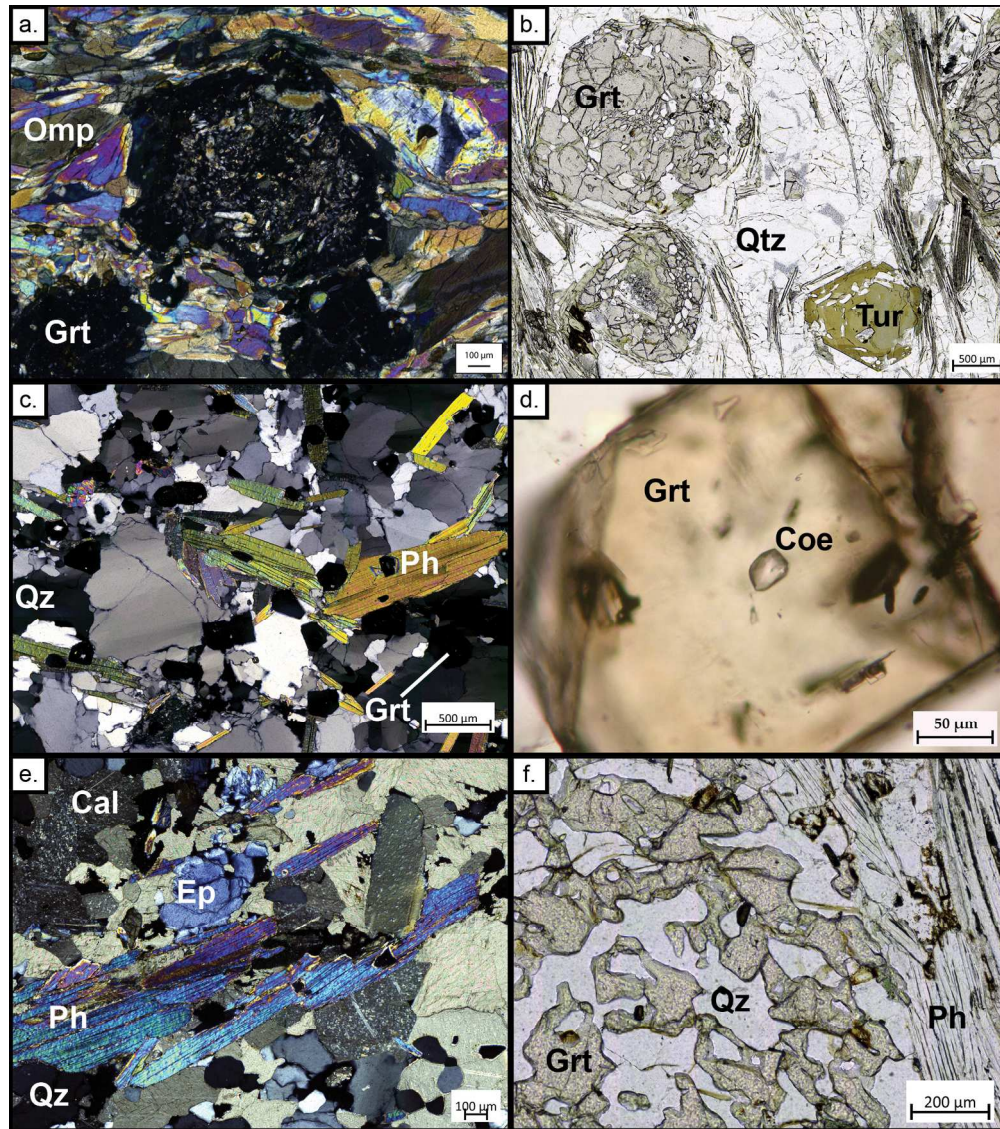


Figure 5 - Representative microstructures from the Lago di Cignana Unit. (a.) Coesite-bearing eclogite. Large, inclusion-bearing garnet porphyroclasts are wrapped around an omphacite + rutile foliation. Coesite occurs as inclusion in garnet; (b.) Coesite-bearing garnet and tourmaline quartzite. Note the large poikiloblasts of garnet and tourmaline with quartz inclusions; (c.) Coesite- and microdiamond-bearing garnet Mn-quartzite; (d.) Coesite inclusion in garnet from Mn-quartzite; (e.) Phengite, epidote and calcite from a garnet calcschist; (f.) Poikilitic garnet porphyroclast with quartz inclusions in garnet calcschist.

180x202mm (300 x 300 DPI)

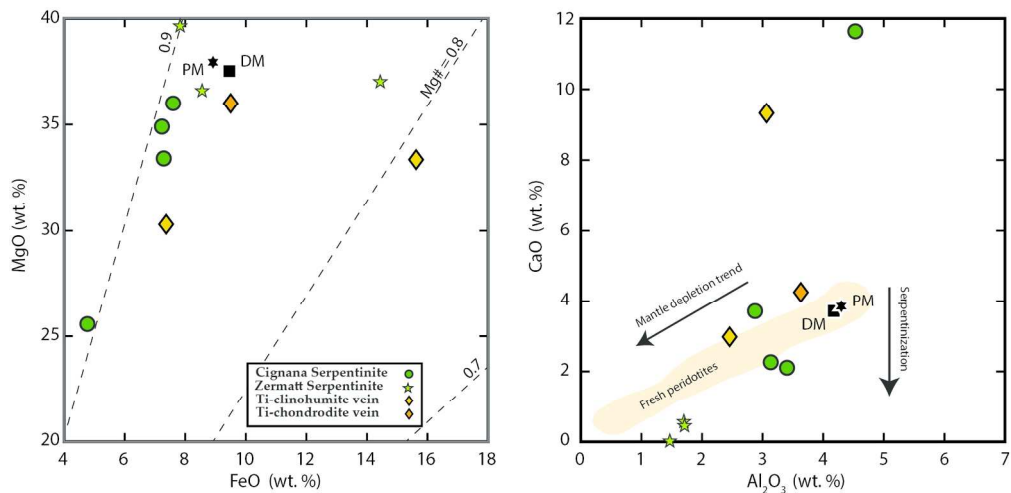


Figure 6 - Major element plots (FeO vs MgO and Al₂O₃ vs CaO) for the Zermatt serpentinites and for the Cignana serpentinites and veins. FeO vs MgO: contours are Mg# = Mg/(Mg+Fe). Al₂O₃ vs CaO: the shaded areas refer to the mantle depletion trend in peridotite.

170x83mm (300 x 300 DPI)

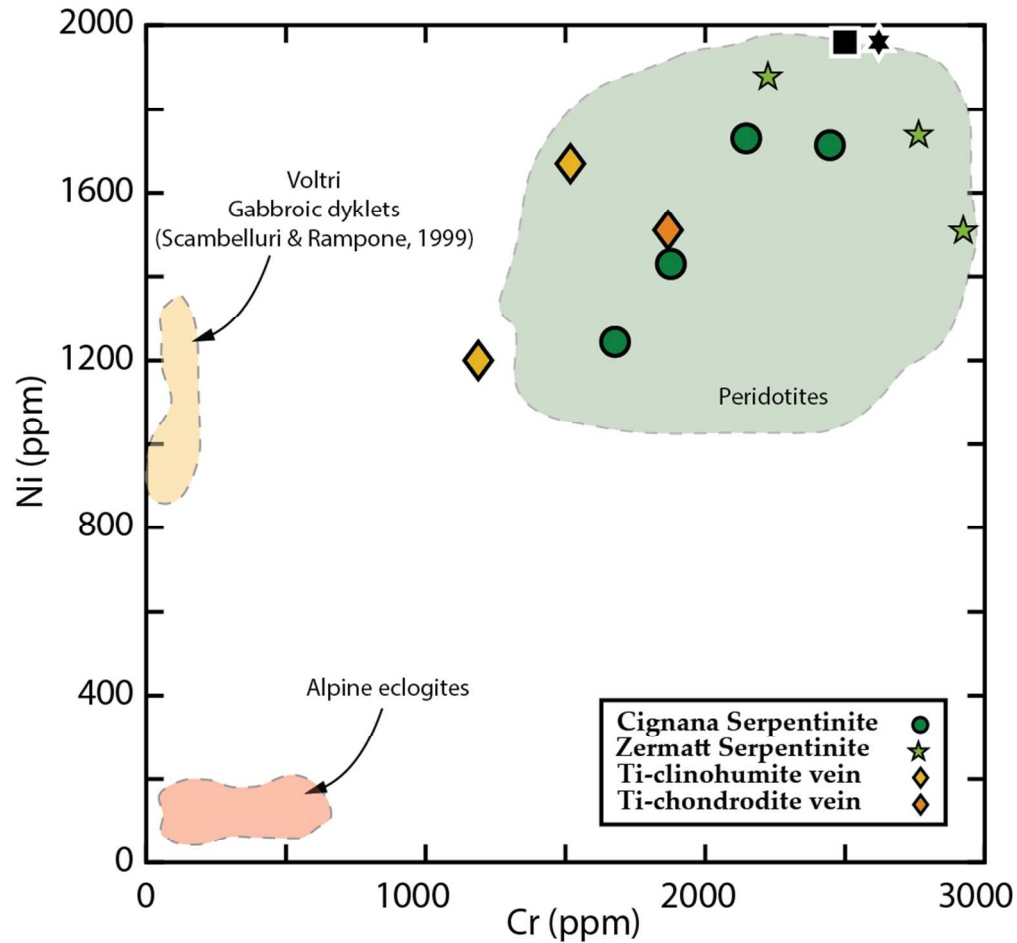


Figure 7 - Cr vs Ni plot for the Zermatt serpentinites and for the Cignana serpentinites and veins. Shaded areas are for Alpine eclogites (Cignana, this work; Monviso, Angiboust et al., 2012), gabbroic dykelets (Voltri, Scambelluri & Rampono, 1999) and peridotites (Lanzo, Müntener et al., 2004; Guarnieri et al., 2012). Note that the Ti-chondrodite (orange diamond) and the Ti-clinohumite veins (yellow diamonds) fall within the peridotite area.

86x81mm (300 x 300 DPI)

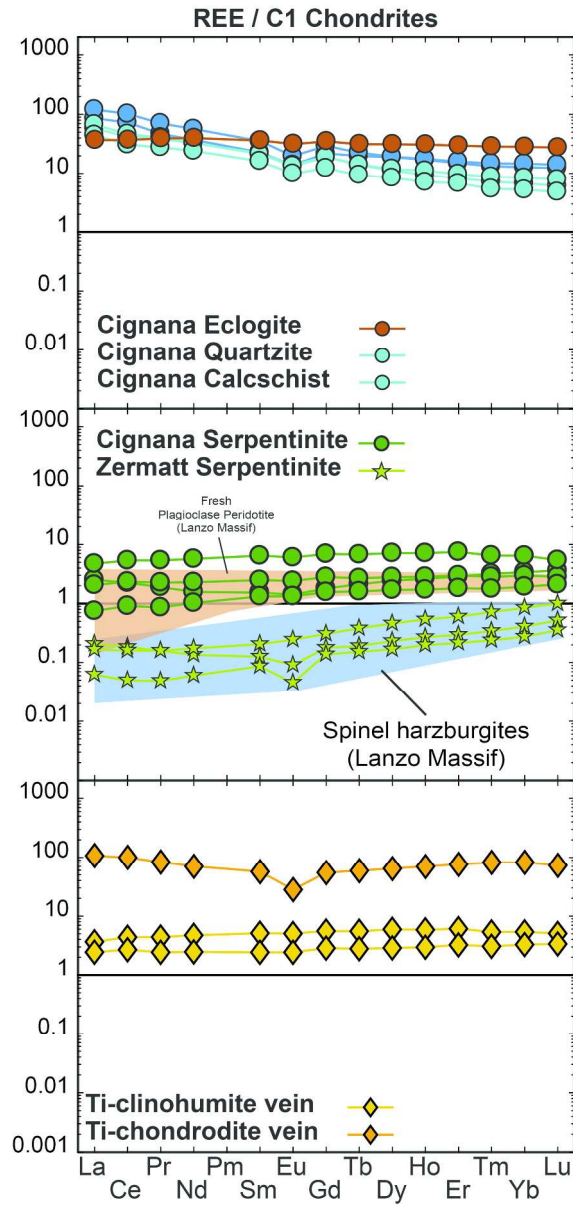


Figure 8 - C1 Chondrite-normalized (McDonough and Sun, 1995) REE patterns of bulk-rock from: eclogite and metasediments from the UHP Lago di Cignana Unit, Cignana and Zermatt serpentinites and Cignana Ti-bearing veins. Shaded areas are for fresh plagioclase peridotite (orange) and spinel harzburgites (blue) from the Lanzo Massif (Guarneri et al, 2012).

184x392mm (300 x 300 DPI)

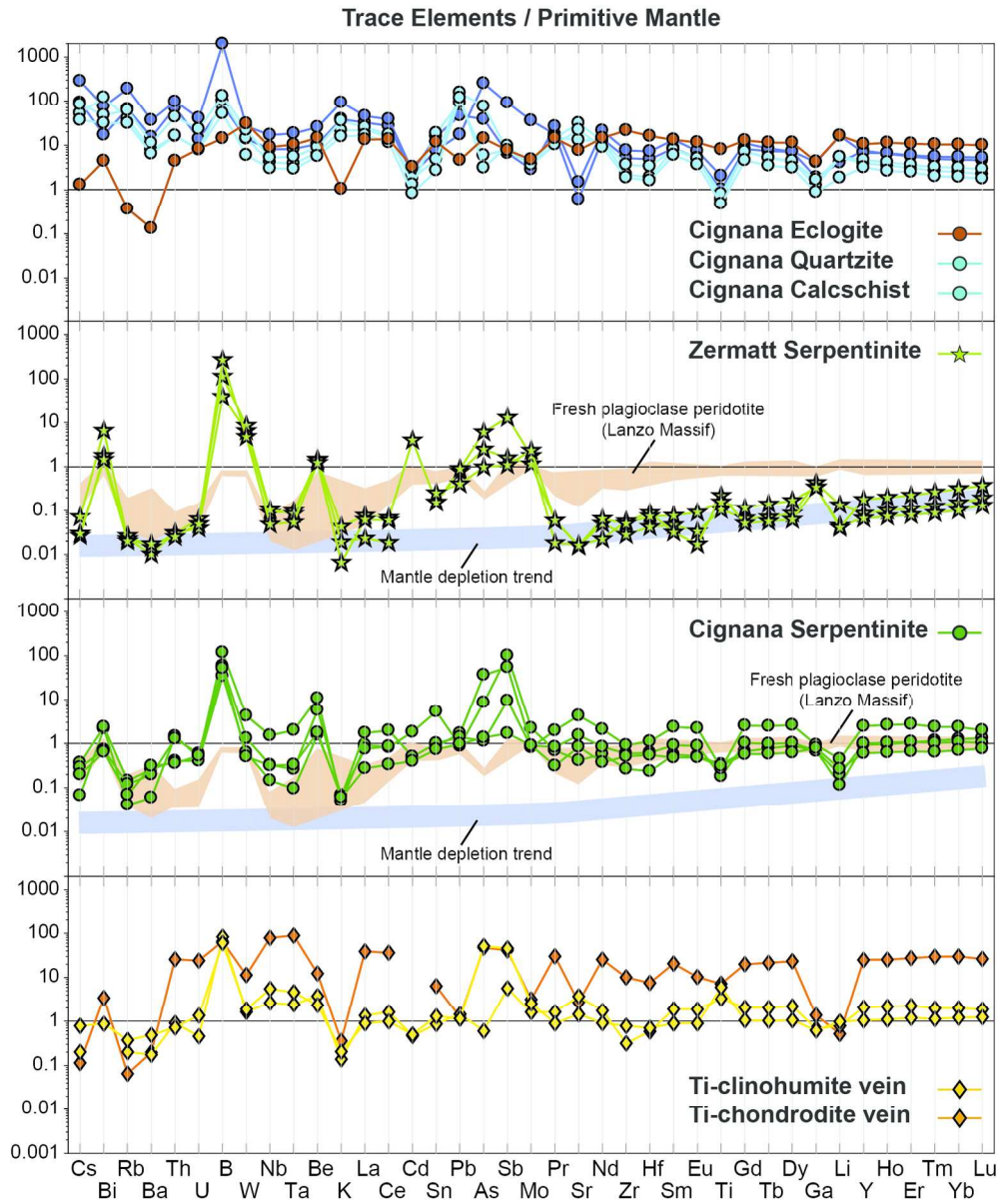


Figure 9 - PM-normalized (McDonough and Sun, 1995; B and Li after Marschall et al., 2017) TE patterns of bulk-rock from: eclogite and metasediments from the UHP Lago di Cignana Unit, Cignana and Zermatt serpentinites and Cignana Ti-bearing veins. Shaded areas are for fresh plagioclase peridotite from the Lanzo Massif (orange; Guarneri et al, 2012) and the mantle depletion trend (blue).

159x194mm (300 x 300 DPI)

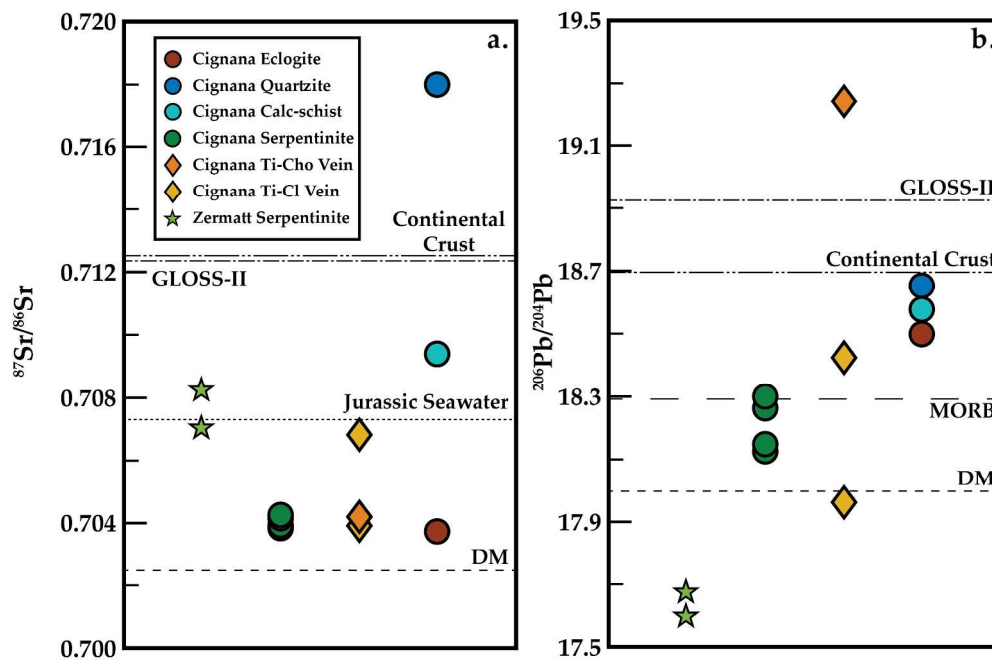


Figure 10 - $^{206}\text{Pb}/^{204}\text{Pb}$ and $^{87}\text{Sr}/^{86}\text{Sr}$ values of analysed samples from the Lago di Cignana Unit, Cignana serpentinites and veins and Zermatt serpentinites. Values from GLOSS-II (Plank, 2014), depleted mantle (Rehka & Hofmann, 1997), Jurassic seawater (Jones & Jenkyns, 2001) and average continental crust (Rudnick and Gao, 2003) are reported for comparison.

255x167mm (300 x 300 DPI)

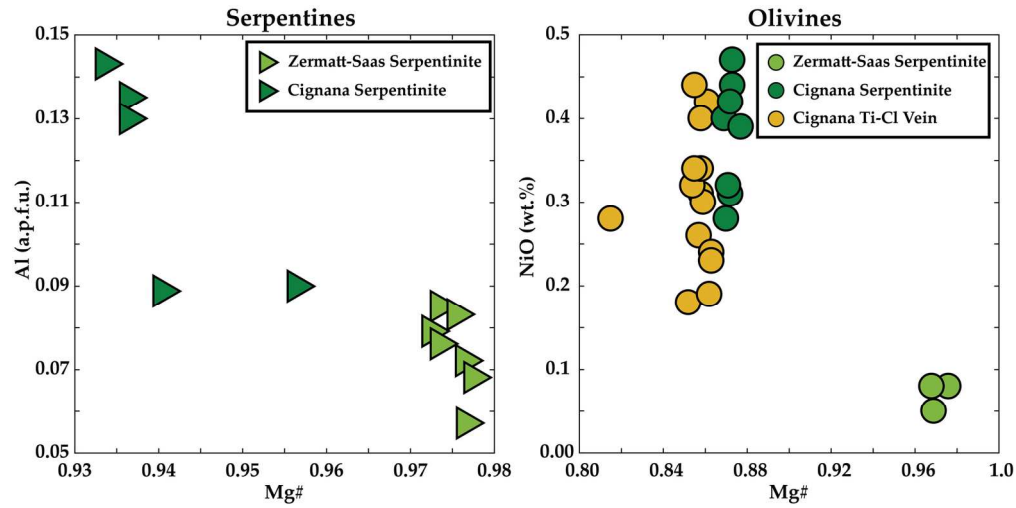


Figure 11 - Mineral analyses of serpentine and olivine from the Zermatt serpentinite, the Cignana serpentinite and the Ti-bearing veins. Serpentine from Zermatt has higher Mg# and lower Al content than serpentinite from Cignana. Mg# in Zermatt olivine is comparable with serpentinite from the same locality. Olivine from the Cignana serpentinite and Ti-clinohumite vein have similar Mg#, lower than in the Zermatt serpentinite.

162x81mm (300 x 300 DPI)

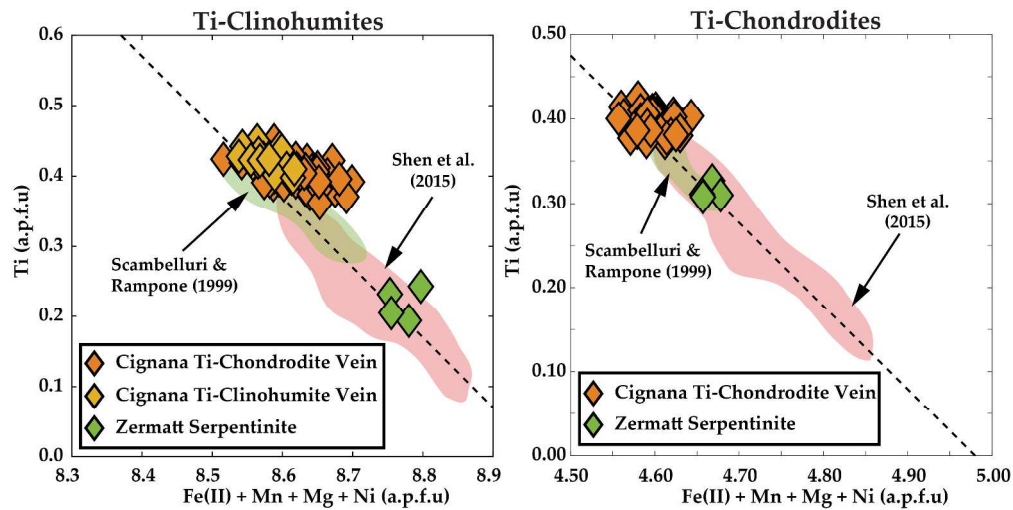


Figure 12 - Mineral analyses of Ti-chondrodite and Ti-clinohumite from the Cignana serpentinite veins and from the Zermatt serpentinite. Note the lower Ti content of both Ti-chondrodite and Ti-clinohumite from the Zermatt-serpentinite respect to Cignana serpentinite veins. Mineral analyses from Scambelluri & Rampone (1999) and Shen et al., (2014) reported for comparison.

323x161mm (300 x 300 DPI)

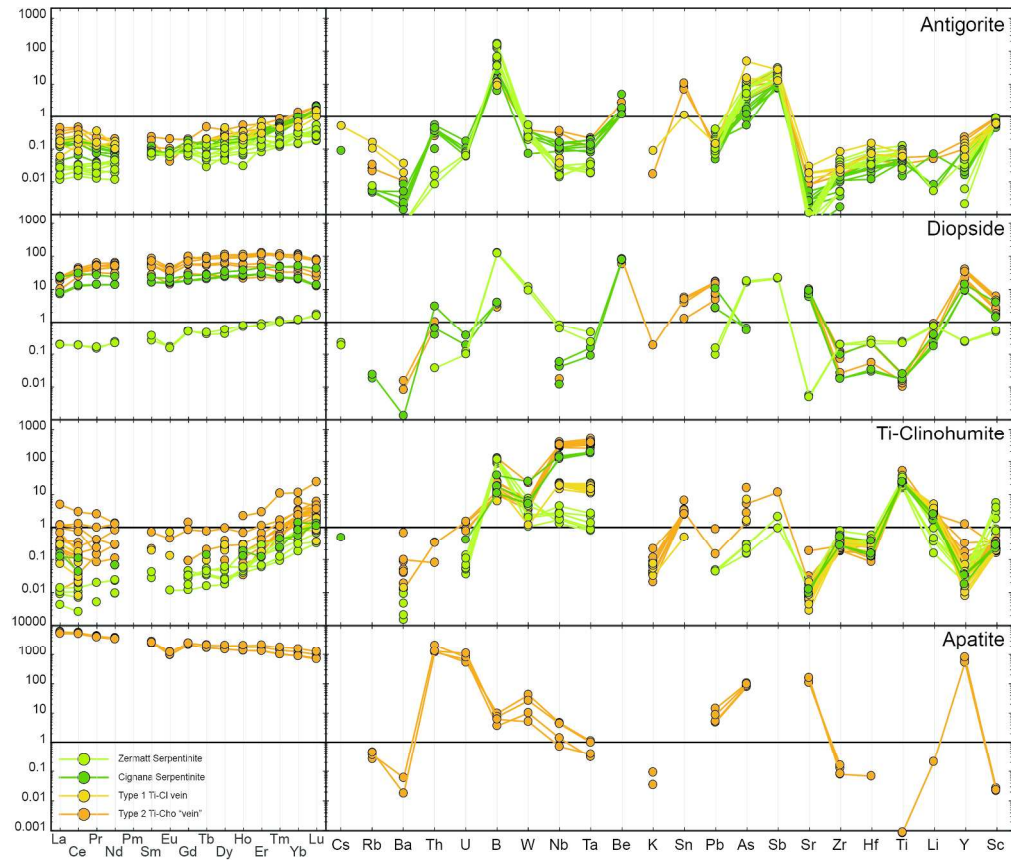


Figure 13 - REE and TE composition of antigorite, diopside, Ti-clinohumite and Apatite from the Cignana and Zermatt serpentinites.

211x180mm (300 x 300 DPI)

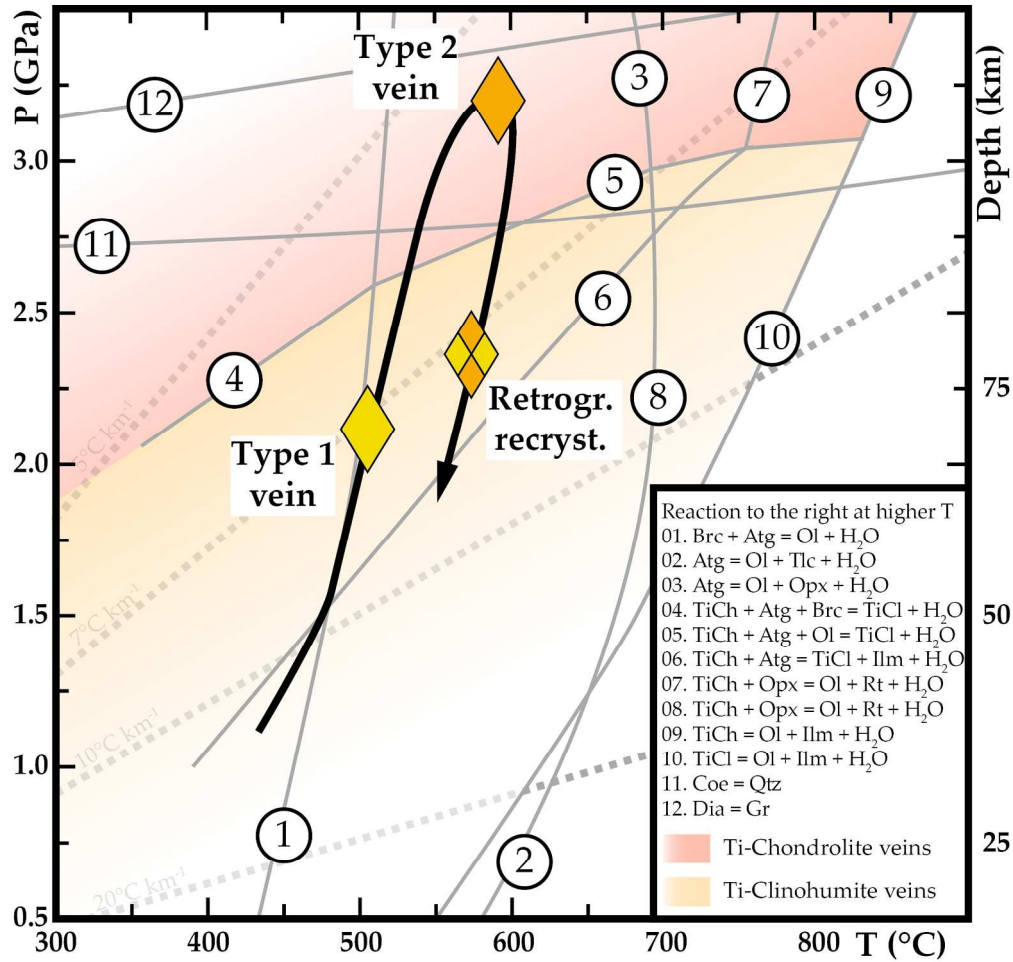


Figure 14 - Pressure-Temperature diagram with the stability field of Ti-clinohumite (light orange) and Ti-chondrodite (dark orange) in serpentinite systems. The main reaction lines involving Ti-clinohumite and Ti-chondrodite and the quartz to coesite transition lines are from Shen et al. (2015). The black arrow corresponds to the PT path of the Lago di Cignana Unit (Groppo et al., 2009). The dashed grey lines are the geothermal gradients for cold (5–7 °C/km) and hot (20 °C/km) subduction. Cignana type 1 veins formed during the prograde path, after the partial dehydration of the Cignana serpentinite. Type 2 veins formed at peak UHP conditions, in the stability field of Ti-chondrodite. Type 1 and 2 veins recrystallized during the retrograde decompression in the stability field of Ti-clinohumite.

187x179mm (300 x 300 DPI)

	Mantle stage	Seafloor exposure	Prograde metamorphism	UHP peak metamorphism	Retrograde metamorphism
Zermatt serpentinite	Mantle processes during the Jurassic opening of the Tethys ocean (Mantle depletion).	Oceanic serpentinization: formation of mesh-structures after olivine and bastites after mantle pyroxene. Chloritization of plagioclase and/ or oxidation of mantle spinel.	Development of a Atg + Ol foliation and veins of Ti-Chu + Ol + Chl + Mt ± Di		Crenulation of previous Ol-bearing foliation and Ti-chu veins and development of a Ol-free axial-plane foliation.
Cignana serpentinite	Mantle processes during the Jurassic opening of the Tethys ocean (Melt-rock interactions).	Oceanic serpentinization: formation of mesh-structures after olivine and bastites after mantle pyroxene. Chloritization of plagioclase and/ or oxidation of mantle spinel.	Development of a Atg + Ol foliation and type 1 Ti-Chu + Ol + Chl + Mt ± Di veins	Formation of type 2 Ti-Chn + Ol + Chl + Di veins	Crenulation of previous Ol-bearing foliation and Ti-chu veins and development of a Ol-free axial-plane foliation. In type 1 and 2 veins, original Ti-Chu and Ti-Chn recrystallize into second generation Ti-chu
Lago di Cignana Unit		Deposition of carbonatic and silicoclastic (and possibly radiolarites) sediments on the seafloor during Jurassic times.	Prograde growth of garnet in basaltic eclogite and metasediments	Formation of coesite inclusion in host garnet and tourmaline. Precipitation of diamond in garnet.	Retrograde chloritization of garnet. Low pressure barrosite and glaucophane partially replace the UHP mineral assemblage.

Figure 15 - Petrogenetic sequence summarizing and comparing the overall evolution of the Zermatt and Cignana serpentinite and the Lago di Cignana Unit.

184x90mm (300 x 300 DPI)

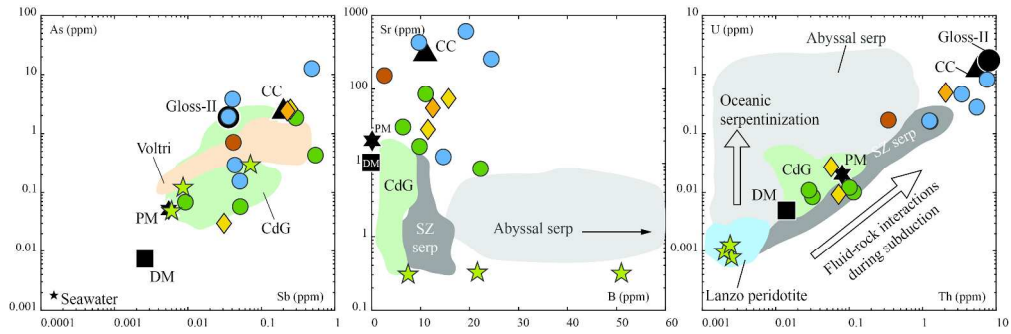


Figure 16 - As vs Sb, Sr vs B and U vs Th plots of analysed samples from the Lago di Cignana Unit, Cignana serpentinites and veins and Zermatt serpentinites. Shaded area from Voltri (Cannaò et al., 2016), Cima di Gagnone (CdG; Scambelluri et al., 2014; Cannaò et al., 2015), Subduction zone (SZ serp) and abyssal serpentinites (Deschamps et al., 2013 and references therein) and Lanzo peridotite (Guarnieri et al., 2012).

340x110mm (300 x 300 DPI)

Peer Review

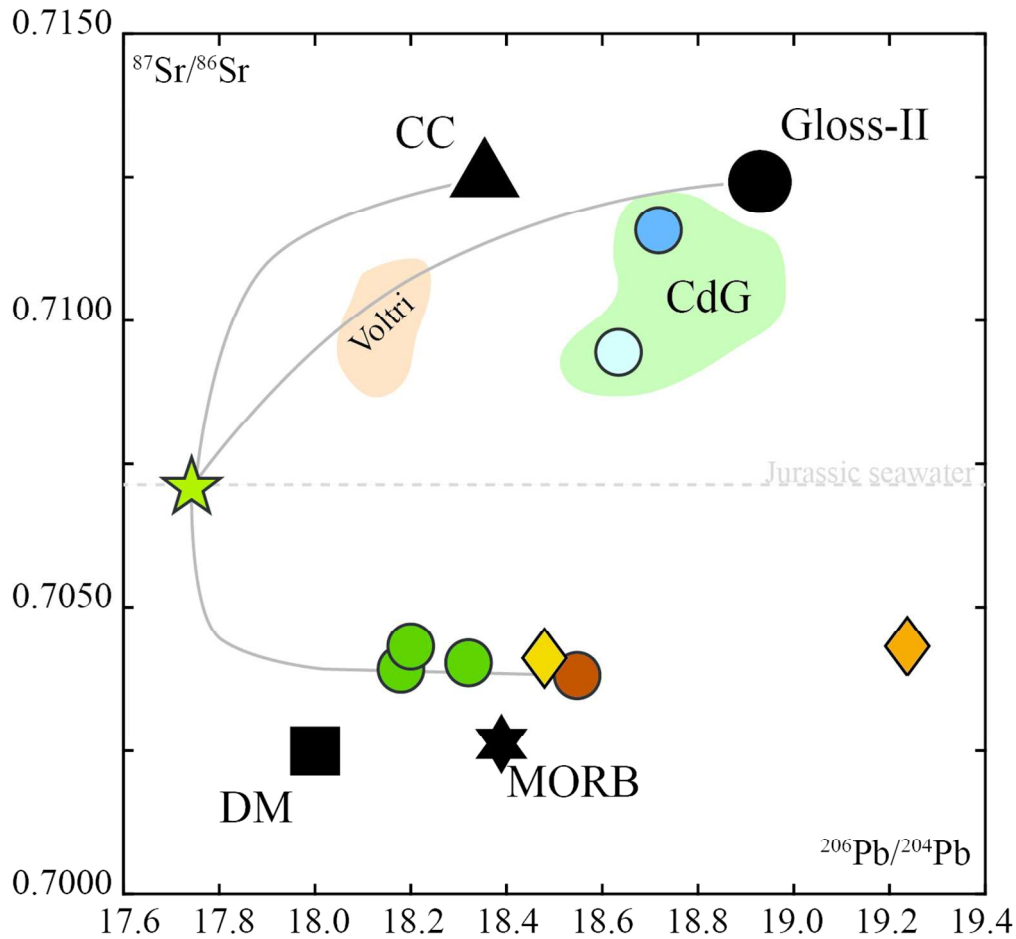


Figure 17 - $^{206}\text{Pb}/^{204}\text{Pb}$ vs $^{87}\text{Sr}/^{86}\text{Sr}$, shows a mixing line between Zermatt serpentinite and a fluid of composition comparable with Cignana eclogite (Sample LCG1401), Continental Crust (Rudnick and Gao, 2003) and GLOSS-II (Plank, 2014). Shaded area from Voltri (Cannaò et al., 2016), Cima di Gagnone (CdG; Scambelluri et al., 2014; Cannaò et al., 2015). Values from GLOSS-II (Plank, 2014), depleted mantle (Rehka & Hofmann, 1997), Jurassic seawater (Jones & Jenkyns, 2001) and average continental crust (Rudnick and Gao, 2003) are reported for comparison.

116x109mm (300 x 300 DPI)

Table 1 - Lists of collected samples and mineral assemblages of the Lago di Cignana Unit and of the Cignana and Zermatt serpentinite.

	Sample Name	Rock Type	Mineral assemblage	GPS coordinates	
				N	E
LCU	LCG1401	Eclogite	Omp, Grt, Rt	5081691	390860
	LCG1414	Quartzite	Qz, Grt, Ph, Ep	5081468	390669
	LCG1415A	Quartzite	Qz, Tur, Grt, Ph, Ep	5081468	390669
	LCG1416A	Calcschists	Cal, Qz, Grt, Ph, Ep	5081405	390653
	LCG1416B	Calcschists	Cal, Qz, Grt, Ph, Ep	5081405	390653
	LCG1501	Impure marble	Cal, Qz, Grt, Ph, Ep	5081405	390653
Cignana serp.	ZSG1402	Ti-chondrodite vein	Ti-Chn, Ti-Chu, Ap, Ol, Chl, Di, Ilm, REE-phases	5080411	390635
	ZSG1502 V	Ti-clinohumite vein	Ti-Chu, Ol, Chl, Di, Ilm, Mag, Atg	5079863	390554
	ZSG1507 V	Ti-clinohumite vein	Ti-Chu, Ol, Chl, Di, Ilm, Mag, Atg	5079808	390474
	ZSG1403	Serpentinite	Atg, Ol, Di, Chl, Mag	5080411	390635
	ZSG1502 S	Serpentinite	Atg, Ol, Di, Chl, Mag	5079863	390554
	ZSG1507 S	Serpentinite	Atg, Ol, Di, Chl, Mag	5079808	390474
ZSZ	ZSG1510	Serpentinite	Atg, Ol, Di, Chl, Mag	5079908	390620
	ZSG1405	Serpentinite	Atg, Ol, Di, Chl, Mag	5070553	395494
	ZSG1406	Serpentinite	Atg, Ol, Di, Chl, Mag	5070553	395494
	ZSG1410	Serpentinite	Atg, Ol, Di, Chl, Mag	5081326	392588

Table 2 - Major (wt.%) and Trace element ($\mu\text{g/g}$) composition of eclogite and metasediments from the Lago di Cignana Unit, Cignana serpentinites and Ti-bearing veins and of Zermatt serpentinite. Samples were analysed for major elements (d.l. = 0.01 wt.%) and V (d.l. 5 $\mu\text{g/g}$), Be, Sr, Zr (d.l. 2 $\mu\text{g/g}$), Sc, Y, and Ba (d.l. 1 $\mu\text{g/g}$) by means of Fusion-ICP-MS at Act-Lab, Canada. Trace elements were analysed by liquid ICP-MS at Geosciences Montpellier (France). Detection limits can be found in Godard et al. (2000). Furthermore, all samples were analysed for major and trace element by PPP-LA-ICP-MS at the University of Bern.

Lago di Cignana Unit																
	Eclogite			Quartzite			Calcschist									
	LCG1401			LCG 1414B			LCG 1415A			LCG 1416A			LCG 1416B			LCG 1501
	FUS	ICP	PPP	FUS	ICP	PPP	FUS	ICP	PPP	FUS	ICP	PPP	FUS	ICP	PPP	PPP
SiO ₂	46.89		49.18	78.28		79.36	71.24		72.43	33.96		37.46	49.45		51.11	29.69
TiO ₂	2.49		2.37	0.219		0.23	0.454		0.44	0.131		0.14	0.182		0.19	0.1
Al ₂ O ₃	15.77		14.55	7.44		6.96	11.73		10.96	3.38		3.12	4.77		4.36	2.59
Fe ₂ O ₃ (T)	10.65		10.55	4.15		3.99	5.18		4.96	1.79		1.85	2.12		2.14	1.6
MnO	0.173		0.17	3.679		3.37	0.234		0.24	0.371		0.38	0.424		0.44	0.39
MgO	6.07		5.83	1.17		1.14	1.8		1.72	0.81		0.95	0.8		0.82	0.94
CaO	12.38		12.09	1.78		1.68	2.45		2.45	33.87		30.5	22.32		21.17	30.46
Na ₂ O	4.75		4.53	0.23		0.27	0.65		0.65	0.19		0.18	0.23		0.21	0.09
K ₂ O	0.03		0.0356	1.09		1.03	2.63		2.53	0.61		0.54	1.01		0.91	0.46
P ₂ O ₅	0.73		0.69	0.06		0.0526	0.11		0.1	0.06		0.0541	0.11		0.0887	0.0324
LOI	0.4		0.4	0.4		0.4	3.09		3.09	25.54		25.54	19.08		19.08	33.65
Total	100.3		100.4	99.23		98.48	99.57		99.57	100.7		100.71	100.5		100.52	100
Li		22.5	24.3		5.61	5.49		22.1	20.2		7.42	6.65		7.35	6.61	2.56
Be	1		0.983	< 1		0.709	2		1.7	< 1		0.462	< 1		0.598	0.382
B			2.68			14.7			365			19.3			24.5	9.69
Sc	33	30.2	28.5	10	8.85	9.99	14	12.6	12.6	5	4.79	5.02	6	5.92	6.5	4.29
Ti		9570	14200		1220	1380		2440	2640		734	839		969	1140	583
V	263	246	269	38	34.7	37.3	89	86.2	86	29	26.7	26.5	35	31.4	32.1	23
Cr			121			41.2			68.7			36.7			32.7	32.4
Mn		1190	1320		26800	26100		1710	1860		2840	2940		3200	3410	3000
Co		27.1	30.5		40.3	38.3		32.7	32.5		15.7	16.6		19.7	20.7	13.2
Ni		85.4	114		48	49.1		84.7	82.1		36.5	47.4		46.1	51.1	37
Cu		14.3			4.67			52.3			369			17.4		87.3
Zn		65.3	49.8		51.5	34.6		101	57.2		27.1	20.7		40.7	24.6	21.1
Ga		17			7.53			16.4			5			6.6		3.53
Ge																1.1
As		0.704	0.229		12.5	12.8		1.89	1.38		3.73	4.13		-	0.291	0.154
Se																0.295
Rb		0.218	0.375		39.1	40.5		113	112		23.4	25.1		36.2	37.9	18.5
Sr	162	152	178	14	12.1	13.7	32	29	30.8	634	605	668	265	255	292	428
Y	42	45	38	32	31.8	28	31	28.7	25.1	20	16.7	16.6	22	19.9	19.6	13.5
Zr	256	10.9	224	61	5.24	53.1	101	3.23	79.3	27	0.671	23.1	39	0.78	37.9	19.5
Nb		5.93	8.26		5.2	5.11		11	10.3		2.71	3.14		3.44	3.94	1.96
Mo			0.237			1.76			0.142			0.182			0.201	0.18
Cd			0.129			0.088			0.103			0.0717			0.052	0.0325
In																0.0116
Sn		1.52			0.987			2			0.623			2.39		0.345
Sb		0.0415	0.0475		0.491	0.441		0.0364	0.037		0.0408	0.0646		0.0436	0.0719	0.0515
Cs		0.0265	0.032		1.91	1.93		5.92	5.86		1.07	1.14		1.73	1.79	0.761
Ba	< 2	0.874	1.41	110	98.7	109	261	237	254	57	50.7	62.4	81	72.5	88.8	42.3
La		8.58	8.28		20.5	18.4		28.8	27.5		13.9	13.4		16.1	16.4	10.7
La		8.58	8.28		20.5	18.4		28.8	27.5		13.9	13.4		16.1	16.4	10.7
Pr		3.6	3.99		4.42	4.4		6.63	7.06		3.58	3.86		3.77	4.27	2.59
Nd		18	19.3		17.1	17.1		26	27.5		15	16.3		15.3	17.4	11.1
Sm		5.26	5.32		3.37	3.46		5.28	5.6		3.31	3.62		3.23	3.69	2.41
Eu		1.76	1.98		0.794	0.812		1.12	1.21		0.79	0.866		0.76	0.888	0.558
Gd		6.89	5.67		4.35	3.45		5.88	4.7		3.86	3.4		3.81	3.38	2.46
Tb		1.12	0.968		0.724	0.644		0.821	0.761		0.513	0.501		0.512	0.503	0.339
Dy		7.55	6.49		4.74	4.35		4.8	4.44		2.79	2.83		2.96	3.01	2.07
Ho		1.67	1.32		0.935	0.837		0.966	0.868		0.52	0.5		0.606	0.573	0.394
Er		4.71	4.14		2.42	2.32		2.57	2.43		1.32	1.41		1.57	1.71	1.09
Tm		0.697	0.58		0.331	0.3		0.366	0.338		0.18	0.184		0.218	0.217	0.135
Yb		4.51	3.95		2.07	1.96		2.37	2.24		1.09	1.17		1.36	1.4	0.853
Lu		0.669	0.574		0.306	0.286		0.345	0.321		0.15	0.158		0.195	0.203	0.119
Hf		0.315	4.45		0.269	1.36		0.108	2.02		0.0279	0.533		0.0295	0.936	0.445
Ta		0.378	0.452		0.301	0.319		0.669	0.689		0.141	0.186		0.201	0.242	0.108
W		0.883	0.332		-	0.398		-	0.763		-	0.412		-	0.632	0.171
Tl																0.111
Pb		0.69	0.785		2.56	2.35		6.89	6.7		23.1	23.6		13.6	12.8	17.6
Bi			0.0106			0.042			0.187			0.298			0.117	0.0774
Th		0.345	0.32		5.51	5.22		7.6	7.73		1.25	1.36		3.44	3.69	1.28
U		0.167	0.284		0.275	0.326		0.812	1.16		0.162	0.233		0.458	0.545	0.159

Table 2 – (continued 1)

Cignana Serpentinite											
	Serpentinite						Ti-chondrodite vein			Ti-Clinohumite Vein	
	ZSG 1403			ZSG 1502S	ZSG 1507S	ZSG 1510	ZSG 1402			ZSG 1502V	ZSG 1507V
	FUS	ICP	PPP	PPP	PPP	PPP	FUS	ICP	PPP	PPP	PPP
SiO ₂	38.94		40.48	40.34	40.98	39.97	35.77		37.91	37.12	42.05
TiO ₂	0.064		0.065	0.04	0.06	0.06	1.537		1.54	1.2	0.66
Al ₂ O ₃	3.13		2.79	2.89	4.55	3.43	3.65		3.33	2.45	3.06
Fe ₂ O ₃ (T)	7.6		7.59	7.34	4.8	7.29	9.5		9.06	15.63	7.41
MnO	0.098		0.0999	0.08	0.07	0.09	0.176		0.17	0.23	0.17
MgO	36		34.84	33.65	25.7	35.19	35.98		34.37	33.38	30.33
CaO	2.26		2.23	3.74	11.71	2.14	4.26		4.54	3	9.34
Na ₂ O	0.01		0.0186	0.05	0.1	0.06	0.02		0.0263	0.05	0.09
K ₂ O	< 0.01		0.0015	0.002	0.0019	0.0017	< 0.01		0.0104	0.0058	0.0039
P ₂ O ₅	< 0.01		0.0023	0.0006	0.0006	0.0017	1		0.94	0.0041	0.0009
LOI	10.42		10.42	11.87	12.03	11.77	8.03		8.03	6.93	6.89
Total	98.53		98.54	100	100	100	99.92		99.93	100	100
Li		0.16	0.255	0.28	0.619	0.369		0.721	0.787	1.35	1.09
Be	< 1		0.727	0.107	0.391	0.12	1		0.842	0.159	0.256
B			22.3	6.45	11.1	9.83			12.5	11.5	15.7
Sc	12	12.9	11.3	16.9	19.7	14.7	13	13.7	12.3	13.2	17.4
Ti		414	390	220	331	380		8690	9230	7190	3960
V	57	64.5	59	66.2	47	70.8	73	77.7	69.4	104	42.1
Cr			2450	1880	1680	2150			1870	1520	1190
Mn		771	774	644	568	683		1360	1320	1780	1320
Co		79.7	89.4	77.4	65	88.3		91.6	103	119	86.5
Ni		1710	2060	1430	1240	1730		1510	1710	1670	1200
Cu		19.8		14.7	9.77	27.1		8.7		59.8	9.77
Zn		40.9	18.1	20.1	13.8	23.9		55.8	45.1	50.7	31.8
Ga		2.73		2.74	3.68	3.15		5.5		2.46	2.7
Ge				0.765	1.02	0.717				0.743	1.05
As		0.43	0.882	1.82	0.0568	0.0676		2.39	3.12	2.56	0.0299
Se				0.138							
Rb		0.0236	0.0333	0.0863	0.0717	0.0406		0.0385	0.107	0.223	0.12
Sr	10	8.33	8.9	30.5	84.9	16.7	62	55.4	60	28.5	74.4
Y	5	4	3.74	4.3	10.6	2.6	103	108	98	4.5	8.8
Zr	4	2.81	2.33	6.24	9.58	5.4	118	106	111	8.15	3.32
Nb		0.999	0.913	0.0961	0.216	0.21		52.2	55.2	3.6	1.74
Mo			0.111	0.0448	0.0412	0.0448			0.159	0.127	0.0796
Cd			0.0729		0.0201	0.016			<0.0582	0.0198	0.0186
In				0.0113	0.008	0.0126				0.0085	0.0068
Sn		0.69		0.11	0.131	0.0959		0.833		0.168	0.112
Sb		0.55	0.448	0.298	0.0521	0.0093		0.227	0.261	0.25	0.031
Cs		0.0014	0.0028	0.0077	0.0061	0.0042		0.0024	0.0058	0.0164	0.0042
Ba	< 2	0.388	1.01	1.73	1.31	2.07	2	1.3	1.65	3.17	1.15
La		0.598	0.561	0.494	1.12	0.178		25.3	25.4	0.577	0.868
La		0.598	0.561	0.494	1.12	0.178		25.3	25.4	0.577	0.868
Pr		0.177	0.186	0.211	0.5	0.08		7.74	8.22	0.226	0.414
Nd		0.717	0.722	1.05	2.61	0.472		31.8	34.3	1.13	2.16
Sm		0.227	0.217	0.369	0.957	0.196		8.42	8.84	0.361	0.762
Eu		0.08	0.0808	0.136	0.338	0.0751		1.58	1.65	0.137	0.285
Gd		0.356	0.33	0.557	1.38	0.312		10.9	10.1	0.574	1.11
Tb		0.0771	0.0694	0.0966	0.245	0.0579		2.13	1.97	0.101	0.2
Dy		0.604	0.53	0.69	1.76	0.416		15.8	14.1	0.706	1.47
Ho		0.144	0.125	0.155	0.386	0.0935		3.76	3.23	0.162	0.321
Er		0.464	0.445	0.484	1.2	0.292		12.1	11.2	0.517	0.98
Tm		0.0787	0.0731	0.0695	0.161	0.0438		2.02	1.77	0.0759	0.133
Yb		0.554	0.532	0.479	1.04	0.312		13.2	12	0.527	0.868
Lu		0.0888	0.0835	0.0695	0.134	0.0517		1.79	1.57	0.083	0.125
Hf		0.0667	0.0543	0.176	0.315	0.156		2.14	2.13	0.198	0.165
Ta		0.0737	0.0716	0.0035	0.0098	0.0123		3.33	3.5	0.17	0.0902
W		0.123	0.117	0.0182	0.038	0.0147		0.325	0.276	0.0537	0.047
Tl				0.0013	0.0015	0.0013				0.0036	0.0015
Pb		0.132	0.229	0.253	0.209	0.146		0.189	0.282	0.171	0.215
Bi			0.0054	0.0059	0.0018	0.0016			0.0086	0.0022	
Th		0.116	0.105	0.0319	0.102	0.0286		2.06	1.91	0.0569	0.0718
U		0.0101	0.0115	0.0083	0.012	0.0108		0.491	0.442	0.0273	0.0092

Table 2 – (continued 2)

Zermatt Serpentinite									
Serpentinite									
	ZSG 1405			ZSG 1406			ZSG 1410		
	FUS	ICP	PPP	FUS	ICP	PPP	FUS	ICP	PPP
SiO ₂	39.07		40.05	36.44		38.11	39.24		40.98
TiO ₂	0.02		0.0189	0.043		0.0447	0.032		0.0317
Al ₂ O ₃	1.71		1.44	1.46		1.26	1.7		1.5
Fe ₂ O ₃ (T)	8.57		8.67	14.45		14.44	7.83		7.73
MnO	0.107		0.11	0.142		0.15	0.13		0.13
MgO	36.61		35.87	37.08		35.68	39.66		38.11
CaO	0.48		0.42	0.02		<0.00980	0.57		0.49
Na ₂ O	<		<	<		<	<		<
	0.01		0.0064	0.01		0.006	0.01		0.0062
K ₂ O	<		<	<		<	<		<
	0.01		0.0013	0.01		0.0006	0.01		<0.00019
P ₂ O ₅	<		<	<		<	<		<
	0.01		0.0015	0.01		0.0008	0.01		0.0018
LOI	11.98		11.98	10.62		10.62	10.56		10.56
Total	98.57		98.57	100.3		100.31	99.72		99.54
Li		0.188	0.201		0.0626	0.0776		0.0566	0.115
Be	< 1		<0.0986	< 1		<0.0960	< 1		<0.0831
B			7.45			21.6			51
Sc	11	12.6	10.7	10	10.9	9.9	12	12.2	11.3
Ti		126	113		268	268		190	190
V	58	63.8	59.3	45	46.8	45.5	51	54.7	53.9
Cr			2930			2770			2230
Mn		844	852		1080	1160		968	1010
Co		74.6	83.8		95.3	111		95.6	114
Ni		1510	1770		1740	2020		1880	2470
Cu		30.9			9.01			17.8	
Zn		44.3	26.7		51.3	46.5		39.3	17.9
Ga		1.73			1.35			1.37	
Ge									
As		-	0.123		0.303	0.446		-	0.0493
Se									
Rb		0.0135	0.0279		0.0157	0.0168		0.0121	0.0164
Sr	< 2	0.308	0.304	< 2	0.328	0.317	< 2	0.318	0.344
Y	3	0.372	0.313	< 1	0.286	0.298	2	0.765	0.71
Zr	2	0.296	0.241	3	0.601	0.641	3	0.525	0.495
Nb		0.0578	0.0544		0.0678	0.0711		0.0315	0.0301
Mo			0.0566			0.0882			0.116
Cd			0.158			<0.0522			<0.0599
In									
Sn		0.0205			0.0196			0.033	
Sb		0.0086	0.0207		0.0706	0.0726		0.006	<0.0151
Cs		0.0015	0.0037		0.0006	0.0025		0.0006	<0.00312
Ba	< 2	0.0672	2.11	< 2	0.0964	0.46	< 2	0.114	1.78
La		0.0502	0.0428		0.0154	0.0182		0.0397	0.0355
La		0.0502	0.0428		0.0154	0.0182		0.0397	0.0355
Pr		0.0148	0.0135		0.0046	0.006		0.0154	0.0153
Nd		0.0627	0.0605		0.0281	0.0339		0.0813	0.0809
Sm		0.0192	0.0175		0.0131	0.0205		0.0313	0.0293
Eu		0.0052	0.005		0.0026	<0.00349		0.014	0.0142
Gd		0.0357	0.0294		0.028	0.0264		0.0624	0.0581
Tb		0.007	0.0062		0.0056	0.0059		0.0139	0.0132
Dy		0.0579	0.0448		0.0423	0.0414		0.115	0.0969
Ho		0.0149	0.0123		0.0106	0.0107		0.0295	0.0242
Er		0.048	0.0467		0.0348	0.0374		0.0978	0.0957
Tm		0.0086	0.0074		0.006	0.0056		0.0176	0.0155
Yb		0.0672	0.055		0.0451	0.0377		0.139	0.117
Lu		0.0128	0.0109		0.0088	0.0095		0.0245	0.0217
Hf		0.0123	0.0079		0.0245	0.0225		0.021	0.0198
Ta		0.0036	0.0021		0.0031	0.0031		0.002	0.0012
W		0.186	0.126		0.246	0.248		0.137	0.14
Tl									
Pb		0.117	0.182		0.134	0.208		0.0614	0.0989
Bi			0.0163			0.0044			0.0036
Th		0.0025	0.0025		0.0024	0.0022		0.002	<0.0027
U		0.0008	0.0014		0.0013	0.002		0.001	0.0019

Table 3 - Pb and Sr isotopic composition of selected samples from the Lago di Cignana Unit, the Cignana serpentinite and the Zermatt-Saas Zone serpentinite. All values are reported as observed (obs.) and as corrected (corr.) for an age of 40 Ma.

		Pb				Sr			
		206/204	2 σ mean	207/204	2 σ mean	208/204	2 σ mean	87/86	2 σ mean
Eclogite	LCG1401	18.547	0.003	15.518	0.002	37.986	0.006	0.703764	0.000006
Tur-Quartzite	LCG1415A	18.706	0.001	15.652	0.001	38.881	0.001	0.711573	0.000006
Calc-schist	LCG1416A	18.636	0.001	15.648	0.001	38.719	0.002	0.709368	0.000005
	ZSG1403	18.341	0.036	15.596	0.03	38.129	0.074	0.704671	0.000007
Cignana	ZSG1502S	18.191	0.025	15.453	0.021	37.737	0.05	0.704160	0.000008
Serpentinite	ZSG1507S	18.172	0.044	15.402	0.036	37.692	0.086	0.703883	0.000004
	ZSG1510	18.32	0.014	15.542	0.013	37.958	0.031	0.703937	0.000011
Ti-Cho vein	ZSG1402	19.239	0.024	15.566	0.02	39.287	0.051	0.704221	0.000004
Ti-Cl vein	ZSG1502V	18.477	0.063	15.576	0.054	38.117	0.131	0.704059	0.000015
Ti-Cl vein	ZSG1507V	18.016	0.071	15.304	0.065	37.404	0.129	0.706789	0.000060
Zermatt	ZSG1406	16.887	0.250	14.841	0.226	35.776	0.558	0.708303	0.000042
Serpentinite	ZSG1410	17.731	0.023	15.548	0.019	37.555	0.046	0.707051	0.000036

Table 4 - Representative electron microprobe analyses of mineral phases from the UHP eclogite of the Lago di Cignana Unit.

Sample LCG1401														
	Garnet		Omphacite					Epidote		Paragonite		Rutile	Titanite	
	Core	Rim												
SiO ₂	38.54	38.75	38.44	38.82	56.86	56.93	56.37	56.46	39.06	38.76	48.30	47.38	0.01	31.20
TiO ₂	-	0.07	0.16	0.02	0.07	0.13	0.05	0.08	0.49	0.28	0.09	0.05	97.63	37.25
Al ₂ O ₃	21.66	21.40	21.67	21.49	11.24	16.07	11.40	11.14	27.00	27.70	38.61	38.91	0.04	1.31
Cr ₂ O ₃	0.01	-	0.01	0.10	0.04	0.05	0.00	0.02	0.09	-	-	0.02	0.04	0.01
FeO	27.45	28.12	27.50	27.57	5.30	6.22	4.65	5.05	7.81	7.29	0.82	0.39	1.11	0.26
MnO	0.77	1.05	1.24	0.67	0.02	-	-	0.00	0.04	0.25	0.03	-	0.05	0.04
MgO	1.95	2.27	2.46	2.03	7.40	3.63	7.64	7.94	0.09	0.14	0.15	0.04	-	-
NiO	-	-	-	-	-	-	-	0.05	0.04	-	0.03	0.02	0.02	-
CaO	11.63	10.92	11.21	11.75	11.78	6.26	11.93	12.12	23.05	23.11	0.22	0.29	0.15	28.75
Na ₂ O	0.03	0.02	0.03	0.03	8.04	11.61	7.95	7.70	0.02	-	7.07	7.50	-	0.02
K ₂ O	-	-	0.01	0.00	0.01	0.00	0.01	0.01	0.00	0.01	0.27	0.32	0.01	-
Totals	102.04	102.61	102.72	102.48	100.76	100.90	100.01	100.58	97.69	97.54	95.59	94.92	99.06	98.84
Si	2.990	2.993	2.960	2.999	1.997	1.966	1.989	1.986	3.025	3.005	3.067	3.033	0.000	4.007
Ti	-	0.004	0.009	0.001	0.002	0.003	0.001	0.002	0.028	0.016	0.004	0.002	0.983	3.598
Al	1.981	1.948	1.967	1.957	0.465	0.654	0.474	0.462	2.464	2.531	2.890	2.936	0.001	0.198
Cr	0.000	-	0.001	0.006	0.001	0.001	0.000	0.001	0.006	-	-	0.001	0.000	0.001
Fe(III)*	0.077	0.055	0.176	0.073	0.013	0.033	0.012	0.013	0.506	0.473	-	-	0.000	-
Fe(II)	1.704	1.762	1.595	1.708	0.143	0.147	0.125	0.136	-	-	0.044	0.021	0.012	0.028
Mn	0.051	0.069	0.081	0.044	0.001	-	-	0.000	0.003	0.016	0.001	-	0.001	0.004
Mg	0.226	0.261	0.282	0.234	0.387	0.187	0.402	0.416	0.010	0.016	0.015	0.003	-	-
Ni	-	-	-	-	-	-	-	0.002	0.002	-	0.002	0.001	0.000	-
Ca	0.967	0.904	0.925	0.973	0.443	0.232	0.451	0.457	1.913	1.920	0.015	0.020	0.002	3.956
Na	0.005	0.004	0.004	0.004	0.547	0.777	0.544	0.525	0.003	-	0.871	0.931	-	0.005
K	-	-	0.001	0.000	0.001	0.000	0.001	0.000	0.000	0.001	0.022	0.026	0.000	-
H*	-	-	-	-	-	-	-	-	1.000	1.000	2.000	2.000	-	1.000
Totals	8.000	8.000	8.000	8.000	4.000	4.000	4.000	4.000	8.960	8.977	8.930	8.974	1.000	12.798

*Fe(III) and H₂O contents calculated stoichiometrically

Table 5 - Representative electron microprobe analyses of mineral phases from the UHP quartzite of the Lago di Cignana Unit.

	Sample LCG1414						Sample LCG1415								
	Epidote		Phengite		Garnet Core Rim		Barroisite		Garnet		Chlorite	Phengite		Tourmaline Core Rim	
SiO ₂	38.08	37.33	51.98	51.96	37.61	37.36	49.51	50.15	37.62	37.12	26.87	53.18	52.87	37.67	37.53
TiO ₂	0.11	0.13	0.35	0.33	0.04	0.05	0.15	0.08	0.02	0.03	-	0.14	0.22	-	-
Al ₂ O ₃	25.25	23.24	27.86	27.36	21.48	21.74	7.66	6.45	21.58	21.31	20.17	27.97	28.08	31.06	29.74
Cr ₂ O ₃	0.06	-	0.07	0.02	-	0.06	0.05	0.04	0.00	0.05	-	0.01	0.00	-	-
FeO	11.03	13.24	3.48	3.78	5.66	29.55	17.48	16.53	30.36	26.40	22.91	2.32	2.22	3.60	6.41
MnO	0.31	0.69	0.05	0.09	30.45	4.47	0.61	0.89	1.71	4.46	0.46	-	0.04	-	-
MgO	0.03	0.03	3.02	2.96	2.02	1.86	11.34	12.42	3.46	1.43	16.53	3.06	3.11	9.06	8.04
NiO	0.01	-	0.04	0.09	0.05	-	0.04	0.08	-	-	-	0.04	0.02	-	-
CaO	23.07	22.59	-	0.03	4.68	7.21	7.04	8.11	5.66	9.06	0.06	0.02	0.01	0.28	0.33
Na ₂ O	-	0.02	0.49	0.44	0.02	0.05	3.49	2.78	0.04	-	0.03	0.42	0.47	2.72	2.81
K ₂ O	-	0.04	9.83	9.82	-	0.03	0.22	0.25	0.00	0.01	-	9.29	9.47	0.04	-
Totals	97.95	97.31	97.17	96.88	102.01	102.38	97.59	97.78	100.44	99.87	87.03	96.45	96.51	84.43	84.86
Si	2.977	2.964	6.806	6.837	2.962	2.924	7.049	7.138	2.974	2.969	5.615	6.928	6.893	6.162	6.210
Ti	0.007	0.008	0.035	0.033	0.002	0.003	0.016	0.009	0.001	0.002	-	-	-	-	-
Al	2.326	2.175	4.300	4.243	1.994	2.006	1.285	1.082	2.010	2.009	4.979	0.014	0.021	5.988	5.799
Cr	0.004	-	0.007	0.002	-1.650	0.004	0.005	0.004	0.000	0.003	-	4.295	4.315	-	-
Fe(III)*	0.721	0.879	-	-	0.030	0.285	1.583	1.432	0.092	0.083	0.111	-	-	-	-
Fe(II)	-	-	0.381	0.416	0.343	1.650	0.498	0.536	1.915	1.683	3.893	-	-	0.492	0.887
Mn	0.021	0.046	0.005	0.011	2.031	0.296	0.073	0.107	0.114	0.303	0.081	0.253	0.242	-	-
Mg	0.004	0.003	0.589	0.581	0.237	0.217	2.407	2.635	0.407	0.171	5.150	-	0.005	2.209	1.983
Ni	0.001	-	-	-	0.003	-	0.005	0.009	-	-	-	0.594	0.604	-	-
Ca	1.932	1.922	-	0.004	0.395	0.605	1.074	1.237	0.480	0.776	0.014	-	-	0.049	0.058
Na	-	0.003	0.124	0.113	0.003	0.008	0.963	0.767	0.006	-	0.024	0.002	0.002	0.863	0.901
K	-	0.004	1.642	1.648	-	0.003	0.041	0.046	0.000	0.001	-	0.107	0.118	0.008	-
H*	1.000	1.000	4.000	4.000	-	-	2.000	2.000	-	-	16.000	-	-	4.004	4.001
B*	-	-	-	-	-	-	-	-	-	-	-	4.000	4.000	3.001	3.002
Totals	8.993	9.004	17.889	17.888	8.000	8.001	16.999	17.002	8.000	8.000	35.868	16.193	16.200	22.776	22.841

*Fe(III), B and H₂O contents calculated stoichiometrically

Table 6 - Representative electron microprobe analyses of mineral phases from the UHP calcschist of the Lago di Cignana Unit.

	Sample LCG1416A										Sample LCG1416B						
	Garnet		Paragonite		Phengite		Chlorite		Calcite		Epidote Core Rim		Phengite		Calcite		
SiO ₂	37.66	38.14	47.31	47.39	47.70	50.82	50.90	25.99	27.42	0.08	0.01	36.51	38.96	51.39	50.38	0.04	-
Al ₂ O ₃	19.55	20.73	38.59	38.36	38.24	27.51	26.73	20.62	19.91	0.02	0.02	21.62	24.70	26.67	27.25	0.01	0.02
FeO	22.12	18.80	0.31	0.34	0.30	2.34	2.74	29.19	20.86	1.71	1.83	12.00	9.44	2.77	3.13	1.47	1.56
MnO	7.50	13.83	-	0.04	0.01	0.02	0.02	0.43	0.43	0.32	0.39	0.53	0.41	0.02	0.04	0.58	0.53
MgO	1.74	1.38	0.20	0.24	0.21	2.94	2.83	11.89	18.46	1.10	1.15	0.16	0.04	2.88	2.75	0.99	0.91
CaO	9.35	8.30	0.20	0.09	0.16	0.01	0.08	0.00	-	55.84	52.66	19.25	22.33	0.03	-	50.91	56.32
Na ₂ O	0.07	0.00	7.51	7.56	7.46	0.58	0.25	-	0.02	-	-	0.05	0.02	0.52	0.63	-	-
K ₂ O	-	0.00	0.71	0.36	0.67	9.71	10.13	0.02	-	-	0.02	0.00	-	10.02	9.95	0.01	-
Totals	97.99	101.19	94.82	94.37	94.74	93.92	93.67	88.14	87.10	59.07	56.07	90.11	95.91	94.31	94.14	54.01	59.34
Si	3.066	3.024	6.074	6.100	6.121	6.840	6.897	5.541	5.660	0.001	0.000	3.091	3.086	6.915	6.813	0.001	-
Al	1.876	1.937	5.840	5.820	5.784	4.365	4.269	5.197	4.853	0.000	0.000	2.157	2.306	4.230	4.343	0.000	0.000
Fe(III)*	-	-	-	-	-	-	-	0.153	0.093	-	-	0.850	0.625	-	-	-	-
Fe(II)	1.506	1.247	0.033	0.037	0.032	0.263	0.310	5.052	3.508	0.024	0.026	-	-	0.312	0.354	0.021	0.022
Mn	0.517	0.929	-	0.004	0.001	0.002	0.002	0.078	0.076	0.005	0.006	0.038	0.028	0.003	0.005	0.009	0.007
Mg	0.211	0.164	0.038	0.046	0.041	0.590	0.572	3.779	5.681	0.028	0.029	0.020	0.005	0.578	0.554	0.026	0.023
Ca	0.816	0.705	0.027	0.013	0.021	0.001	0.011	0.001	-	1.008	0.969	1.746	1.895	0.005	-	0.948	1.016
Na	0.011	0.001	1.869	1.887	1.856	0.151	0.066	-	0.015	-	-	0.008	0.004	0.136	0.166	-	-
K	-	0.000	0.116	0.058	0.110	1.667	1.751	0.009	-	-	0.000	0.000	-	1.720	1.716	0.000	-
H*	-	-	4.000	4.000	4.000	4.000	4.000	16.000	16.000	-	-	1.000	1.000	4.000	4.000	-	-
C*	-	-	-	-	-	-	-	-	-	0.966	0.984	-	-	-	-	0.997	0.965
Totals	8.002	8.007	17.997	17.963	17.966	17.880	17.877	35.810	35.887	2.031	2.015	8.910	8.950	17.897	17.951	2.002	2.034

*Fe(III), CO₂ and H₂O contents calculated stoichiometrically

Table 7 - Representative electron microprobe analyses of mineral phases from the Cignana serpentinite.

Sample 1503										
	Chlorite		Diopside		Olivine		Antigorite		Ti-Clinohumite	
SiO ₂	33.60	33.59	56.01	55.29	39.99	40.10	42.17	42.22	36.15	36.36
TiO ₂	0.04	0.00	0.15	0.00	0.00	0.00	0.06	0.00	4.64	4.40
Al ₂ O ₃	12.90	12.66	0.03	0.00	0.01	0.01	2.44	2.60	0.00	0.00
Cr ₂ O ₃	0.66	0.74	0.05	0.03	0.01	0.06	0.34	0.31	0.00	0.00
FeO	4.61	4.55	1.87	1.26	13.13	13.04	4.51	4.75	12.65	12.46
MnO	0.03	0.07	0.12	0.05	0.37	0.40	0.07	0.07	0.40	0.49
MgO	34.30	33.76	18.14	17.93	47.96	47.22	37.44	37.69	45.50	45.73
NiO	0.12	0.17	0.11	0.00	0.47	0.40	0.14	0.19	0.32	0.22
CaO	0.02	0.00	25.45	25.67	0.01	0.04	0.01	0.03	0.02	0.04
Na ₂ O	0.00	0.00	0.18	0.09	0.00	0.02	0.00	0.05	0.02	0.03
K ₂ O	0.00	0.00	0.00	0.00	0.00	0.00	0.00	0.02	0.00	0.02
Y ₂ O ₃	0.00	0.00	0.00	0.00	0.00	0.00	0.00	0.00	0.00	0.00
P ₂ O ₅	0.03	0.00	0.00	0.00	0.04	0.04	0.00	0.01	0.01	0.00
Totals	86.32	85.55	102.11	100.31	102.00	101.33	87.17	87.93	99.70	99.74
Si	6.435	6.495	1.989	1.996	0.974	0.984	1.982	1.972	3.959	3.973
Ti	0.006	0.000	0.004	0.000	0.000	0.000	0.002	0.000	0.382	0.362
Al	2.916	2.886	0.001	0.000	0.000	0.000	0.135	0.143	0.000	0.000
Cr	0.100	0.114	0.001	0.001	0.000	0.001	0.013	0.011	0.000	0.000
Fe(III)	0.000	0.000	0.001	0.001	0.014	0.008	0.000	0.000	0.000	0.000
Fe(II)	0.780	0.740	0.054	0.038	0.254	0.259	0.177	0.186	1.159	1.139
Mn	0.006	0.012	0.004	0.001	0.008	0.008	0.003	0.003	0.037	0.045
Mg	9.792	9.732	0.961	0.965	1.741	1.728	2.624	2.625	7.429	7.450
Ni	0.019	0.026	0.003	0.000	0.009	0.008	0.005	0.007	0.028	0.019
Ca	0.004	0.000	0.969	0.993	0.000	0.001	0.000	0.001	0.002	0.004
Na	0.000	0.000	0.012	0.006	0.000	0.001	0.000	0.004	0.004	0.006
K	0.000	0.001	0.000	0.000	0.000	0.000	0.000	0.001	0.000	0.002
H	16.000	16.000	0.000	0.000	0.000	0.000	4.000	4.000	0.000	0.000
Totals	36.057	36.006	4.000	4.000	3.000	3.000	8.942	8.953	13.000	13.000

*Fe(III) and H₂O contents calculated stoichiometrically

Table 8 - Representative electron microprobe analyses of mineral phases from Ti-chondrodite and Ti-clinohumite veins hosted within Cignana serpentinite.

	Sample 1402				Sample 1502				Sample 1507													
	Chlorite		Ti-Chondrodite		Ti-Clinohumite		Chlorite		Diopside		Olivine		Ti-Clinohumite		Chlorite		Diopside		Olivine		Ti-Clinohumite	
SiO ₂	33.83	33.74	32.42	32.60	35.70	35.86	33.68	34.25	55.20	55.55	40.03	39.88	35.65	35.88	33.73	35.05	55.43	55.50	40.01	40.00	35.47	35.31
TiO ₂	0.00	0.02	8.85	8.55	5.13	5.11	0.04	0.00	0.04	0.00	0.00	0.00	5.03	4.62	0.10	0.20	0.02	0.00	0.13	0.09	4.91	4.92
Al ₂ O ₃	13.12	13.44	0.01	0.03	0.00	0.00	13.04	13.42	0.03	0.01	0.00	0.01	0.00	0.02	13.61	10.90	0.05	0.17	0.00	0.02	0.00	0.02
Cr ₂ O ₃	0.35	0.27	0.00	0.00	0.03	0.03	0.05	0.38	0.00	0.00	0.04	0.01	0.00	0.00	0.12	0.04	0.02	0.09	0.05	0.00	0.02	0.00
FeO	4.92	4.85	12.88	12.73	12.63	12.34	5.17	5.16	1.34	1.32	13.77	13.75	13.81	13.73			1.96	2.87				
MnO	0.05	0.04	0.51	0.43	0.32	0.33	0.02	0.00	0.13	0.15	0.54	0.49	0.58	0.63	5.63	5.15	0.09	0.15	14.03	13.11	16.54	16.93
MgO	34.25	33.49	42.79	42.52	45.83	45.53	32.96	32.91	17.65	17.56	46.08	45.81	43.01	43.49	0.11	0.09	17.28	16.47	0.66	0.50	0.66	0.66
NiO	0.16	0.10	0.14	0.10	0.19	0.16	0.28	0.23	0.00	0.01	0.31	0.26	0.16	0.32	32.53	33.79	0.05	0.06	45.17	46.15	40.95	40.66
CaO	0.00	0.00	0.05	0.01	0.00	0.01	0.01	0.00	25.45	25.47	0.00	0.00	0.00	0.01	0.18	0.16	24.92	24.05	0.18	0.24	0.22	0.12
Na ₂ O	0.01	0.00	0.03	0.01	0.00	0.03	0.03	0.03	0.06	0.06	0.01	0.01	0.02	0.01	0.02	0.00	0.27	0.70	0.00	0.02	0.02	0.00
K ₂ O	0.04	0.02	0.02	0.00	0.01	0.01	0.01	0.00			0.00	0.00	0.02	0.00	0.03	0.00	0.00	0.01	0.00	0.00	0.02	0.00
Totals	86.73	86.03	97.70	97.00	99.84	99.44	85.28	86.39	99.90	100.15	100.78	100.22	98.28	98.71	86.07	85.39	100.08	100.07	100.23	100.14	98.82	98.64
Si	6.452	6.481	1.986	2.010	3.904	3.939	6.531	6.544	2.003	2.009	0.992	0.994	4.003	4.003	6.491	6.779	2.010	2.017	1.000	0.996	4.014	4.009
Ti	0.000	0.002	0.408	0.396	0.422	0.422	0.006	0.000	0.001	0.000	0.000	0.000	0.425	0.388	0.014	0.029	0.000	0.000	0.002	0.002	0.418	0.420
Al	2.953	3.045	0.000	0.002	0.001	0.000	2.983	3.028	0.001	0.000	0.000	0.000	0.000	0.003	3.087	2.485	0.002	0.007	0.000	0.001	0.000	0.003
Cr	0.053	0.041	0.000	0.000	0.003	0.003	0.008	0.058	0.000	0.000	0.001	0.000	0.000	0.000	0.018	0.007	0.001	0.003	0.001	0.000	0.002	0.000
Fe(III)	0.000	0.030	0.000	0.000	0.000	0.000	0.031	0.093	0.000	0.000	0.004	0.003	0.000	0.000	0.060	0.062	0.000	0.000	0.000	0.001	0.000	0.000
Fe(II)	0.821	0.749	0.660	0.656	1.155	1.134	0.807	0.732	0.041	0.040	0.281	0.283	1.297	1.281	0.846	0.771	0.059	0.087	0.293	0.272	1.565	1.608
Mn	0.008	0.007	0.027	0.022	0.029	0.031	0.003	0.000	0.004	0.005	0.011	0.010	0.055	0.060	0.019	0.014	0.003	0.005	0.014	0.010	0.063	0.064
Mg	9.738	9.590	3.908	3.908	7.470	7.456	9.528	9.373	0.955	0.947	1.703	1.703	7.199	7.233	9.331	9.742	0.934	0.892	1.683	1.713	6.909	6.883
Ni			0.007	0.005	0.016	0.014	0.044	0.035	0.000	0.000	0.006	0.005	0.014	0.028	0.028	0.025	0.001	0.002	0.004	0.005	0.020	0.011
Ca	0.025	0.015	0.003	0.001	0.000	0.001			0.989	0.987	0.000	0.000	0.000	0.001	0.003	0.001	0.968	0.937	0.000	0.001	0.002	0.000
Na			0.000	0.000	0.000	0.000	0.002	0.001	0.004	0.004	0.000	0.000	0.004	0.003	0.024	0.003	0.019	0.050	0.000	0.000	0.005	0.000
K			0.000	0.000	0.000	0.000	0.020	0.025	0.000	0.001	0.000	0.000	0.003	0.000	0.009	0.000	0.000	0.000	0.000	0.000	0.000	0.002
H	16.000	16.000	0.000	0.000	0.000	0.000	16.000	16.000	0.000	0.000	0.000	0.000	0.000	0.000	16.000	16.000	0.000	0.000	0.000	0.000	0.000	0.000
Totals	36.050	35.961	7.000	7.000	13.000	13.000	35.968	35.888	3.998	3.993	3.000	3.000	13.000	13.000	35.929	35.917	3.998	4.000	2.997	3.000	13.000	13.000

*Fe(III) and H₂O contents calculated stoichiometrically

Table 9 - Representative electron microprobe analyses of mineral phases from the Zermatt serpentinite.

Sample ZSG1406																
Olivine		Antigorite				Ti-Clinohumite				Ti-Chondrodite						
SiO ₂	42.21	42.12	42.11	42.42	43.5 7	44.5 3	42.5 7	43.3 5	37.90	37.88	38.13	38.75	33.8 5	34.2 2	34.6 6	34.8 1
TiO ₂	0.04	0.03	0.08	0.00	0.05	0.00	0.00	0.05	2.43	3.09	2.93	2.62	7.35	7.02	7.06	7.01
Al ₂ O ₃	0.02	0.00	0.00	0.00	1.55	1.52	1.22	1.44	0.01	0.00	0.03	0.02	0.01	0.00	0.00	0.03
Cr ₂ O ₃	0.00	0.00	0.00	0.04	0.04	0.01	0.07	0.09	0.00	0.00	0.00	0.00	0.04	0.00	0.07	0.00
FeO	3.25	2.43	3.20	3.25	1.88	1.75	1.62	1.94	3.15	2.96	2.89	2.81	3.48	3.64	3.44	3.48
MnO	0.40	0.45	0.48	0.57	0.02	0.04	0.00	0.07	0.44	0.53	0.42	0.52	0.72	0.56	0.65	0.65
MgO	54.88	55.06	55.03	54.87	39.9 8	39.6 1	39.9 4	39.9 0	53.37	54.51	53.94	54.47	50.5 4	51.0 2	50.9 9	51.1 5
NiO	0.08	0.08	0.05	0.08	0.07	0.06	0.04	0.13	0.16	0.04	0.01	0.07	0.05	0.04	0.11	0.05
CaO	0.00	0.00	0.02	0.00	0.00	0.00	0.00	0.01	0.00	0.02	0.01	0.01	0.00	0.01	0.02	0.02
Totals	100.8 8	100.1 8	100.9 7	101.2 4	87.1 7	87.5 2	85.4 6	86.9 8	97.46	99.03	98.36	99.27	96.0 4	96.5 2	96.9 9	97.2 0
Si	0.996	0.997	0.992	0.998	2.01 6	2.04 6	2.00 9	2.01 3	4.024	3.957	4.011	4.036	2.00 2	2.01 1	2.02 9	2.03 2
Ti	0.001	0.001	0.001	0.000	0.00 2	0.00 0	0.00 0	0.00 2	0.194	0.243	0.232	0.205	0.32 7	0.31 0	0.31 1	0.30 8
Al	0.000	0.000	0.000	0.000	0.08 5	0.08 3	0.06 8	0.07 9	0.001	0.000	0.003	0.002	0.00 0	0.00 0	0.00 0	0.00 2
Cr	0.000	0.000	0.000	0.001	0.00 1	0.00 0	0.00 3	0.00 3	0.000	0.000	0.000	0.000	0.00 2	0.00 0	0.00 3	0.00 0
Fe(III)	0.000	0.000	0.001	0.000	0.00 0	0.00 0	0.00 0	0.00 0	0.000	0.000	0.000	0.000	0.00 0	0.00 0	0.00 0	0.00 0
Fe(II)	0.064	0.048	0.062	0.064	0.07 3	0.06 7	0.06 4	0.07 5	0.280	0.259	0.254	0.245	0.17 2	0.17 9	0.16 8	0.17 0
Mn	0.008	0.009	0.010	0.011	0.00 1	0.00 1	0.00 0	0.00 3	0.040	0.047	0.038	0.046	0.03 6	0.02 8	0.03 2	0.03 2
Mg	1.930	1.943	1.933	1.924	2.75 8	2.71 3	2.81 0	2.76 3	8.448	8.489	8.459	8.458	4.45 7	4.46 9	4.45 0	4.45 2
Ni	0.002	0.002	0.001	0.002	0.00 3	0.00 2	0.00 2	0.00 5	0.014	0.003	0.001	0.006	0.00 2	0.00 2	0.00 5	0.00 2
Ca	0.000	0.000	0.000	0.000	0.00 0	0.00 0	0.00 0	0.00 1	0.000	0.002	0.001	0.002	0.00 0	0.00 1	0.00 1	0.00 1
H	0.000	0.000	0.000	0.000	4.00 0	4.00 0	4.00 0	4.00 0	13.00 0	13.00 0	13.00 0	13.00 0	7.00 0	7.00 0	7.00 0	7.00 0
Totals	3.000	3.000	3.000	3.000	8.93 9	8.91 3	8.95 6	8.94 4	8.780	8.797	8.753	8.755	4.66 8	4.67 8	4.65 6	4.65 7

*Fe(III) and H₂O contents calculated stoichiometrically

Table 10 - Representative laser ablation in-situ trace element analyses of mineral phases from the UHP eclogite and metasediments of the Lago di Cignana Unit. All data are reported in µg/g.

	Sample LCG1401					Sample LCG1414					Sample LCG1415			
	Garnet		Omphacite		Rutile	Garnet		White Mica			Garnet		White Mica	
Li	1.05	1.08	64	61	<0.195	<0.3	2.79	5.3	45	47	20.8	19.8	57	55
Be	<1.21	<1.09	2.04	1.89	<0.218	<0.55	<0.35	<0.34	6.2	7.1	<0.076	<0.292	6.4	6.7
B	<0.39	<0.37	0.7	0.64	<0.26	<0.33	<0.201	<0.2	111	109	0.089	<0.143	100	104
Sc	62	77	27.1	24.1	1.96	1.04	87	29.8	2.06	2.02	75	231	2.07	2.14
V	45	51	340	313	1020	960	11.5	18.8	231	234	30.7	34	220	220
Cr	49	49	33	74	202	252	40	86	122	116	63	59	104	160
Co	27.8	44	21.6	14.6	0.0265	<0.0246	201	189	67	67	107	65	31.4	34
Ni	<0.93	0.98	142	129	15	10.8	2.99	5.2	420	440	1.15	1.41	131	141
Cu	<0.238	0.35	13.3	9.6	1.7	1.37	29.4	19	2.2	1.85	0.315	0.153	2.78	0.78
Zn	56	65	84	76	1.08	0.97	165	216	193	186	108	159	166	184
As	<0.094	<0.093	0.032	0.038	<0.047	<0.045	94	19.4	0.171	0.122	0.0261	<0.0261	0.0216	0.0215
Rb	0.102	<0.0295	0.094	0.0218	<0.0182	<0.0156	<0.022	0.08	430	430	0.015	0.0229	400	420
Sr	0.063	0.064	22.8	23.4	4.1	4.5	0.018	0.0143	8.6	8.3	0.0112	0.0182	19.9	20.6
Y	450	218	0.256	0.4	0.309	0.308	91	146	0.083	0.074	180	302	0.04	0.039
Zr	16.3	7.7	0.55	0.68	55	48	0.34	0.66	0.042	0.051	1.59	51	0.0245	0.023
Nb	<0.019	0.042	<0.0033	<0.0052	275	308	<0.0122	<0.0104	0.89	0.86	<0.0032	0.211	2.2	1.48
Mo	0.39	0.226	<0.0271	<0.043	10.1	6.5	13.2	9.1	<0.093	<0.085	0.281	0.96	<0.0203	<0.0183
Cd	0.73	0.64	0.168	0.126	<0.081	0.167	<0.153	<0.122	<0.168	<0.155	<0.037	<0.142	<0.0266	0.0303
Sb	<0.117	<0.115	0.0251	<0.036	1.47	1.09	<0.078	<0.07	<0.085	<0.079	<0.0124	<0.047	0.0159	0.0151
Cs	<0.0143	<0.0137	0.0211	<0.0035	<0.0108	<0.0094	<0.0137	<0.0145	21.8	22.1	<0.00198	<0.0076	26.3	28.2
Ba	<0.122	<0.116	0.144	0.079	<0.066	<0.08	<0.09	<0.1	920	940	<0.0142	<0.055	800	810
La	<0.0123	<0.0144	0.0061	0.0127	<0.0083	0.0167	<0.0083	<0.0081	0.0186	0.026	<0.00187	<0.0072	0.0055	0.0066
Ce	<0.0181	<0.0173	0.042	0.087	<0.007	0.075	0.0045	<0.0103	0.045	0.039	0.0043	<0.0093	0.00123	0.00156
Pr	<0.0142	<0.0136	0.0118	0.0276	0.0035	<0.0109	<0.0077	<0.0089	<0.0087	<0.0079	0.00292	<0.0071	<0.00131	<0.00115
Nd	<0.071	0.085	0.152	0.257	<0.0135	<0.047	<0.044	<0.035	<0.05	<0.045	0.164	0.073	<0.0097	<0.0086
Sm	0.39	0.48	0.112	0.201	<0.046	<0.056	0.149	0.52	<0.0187	0.0231	2.15	0.82	<0.00282	<0.00215
Eu	0.63	0.56	0.068	0.087	<0.0048	<0.0112	0.18	0.53	<0.0134	<0.012	2	0.83	0.0035	0.0035
Gd	6.7	6.5	0.194	0.311	<0.047	<0.039	1.99	6.6	<0.07	<0.064	26.4	14.6	<0.0094	<0.0082
Tb	4.3	3.5	0.0263	0.048	<0.0054	<0.0091	0.97	2.6	<0.00266	0.00246	6.6	6.6	<0.00127	<0.00111
Dy	63	39	0.095	0.12	<0.037	<0.051	11.3	21.5	<0.0147	<0.0123	41	62	<0.0071	<0.0062
Ho	17.6	8.7	0.0089	0.0134	<0.00255	<0.006	2.95	4.2	<0.00292	<0.00244	6.5	11.4	<0.00045	0.00063
Er	58	24.7	0.013	0.037	<0.0115	<0.0271	10.4	10.3	<0.033	<0.0293	13.7	25.6	<0.00206	<0.00157
Tm	9.1	3.2	<0.00238	<0.0038	<0.006	<0.0102	1.57	1.12	<0.00291	0.0036	1.32	3.15	<0.00045	<0.00035
Yb	66	23.3	<0.0159	0.039	0.0192	<0.041	12	7.1	<0.0191	<0.016	7.4	21.4	<0.00294	<0.00224
Lu	11	4.2	<0.0043	<0.0068	<0.00285	<0.01	1.71	0.92	<0.00312	<0.00261	1.17	4	<0.00049	<0.00037
Hf	0.43	0.181	0.045	0.063	2.41	2	<0.0296	0.0114	<0.033	<0.0301	0.0265	1.64	<0.0079	<0.0071
Ta	<0.0207	<0.0199	<0.00264	<0.0042	16.6	18.5	<0.0068	<0.0085	0.0083	0.0136	<0.00168	0.0262	0.0159	0.0226
W	<0.0225	<0.0207	<0.0157	<0.0248	1.06	1.93	<0.0101	<0.027	1.48	1.34	<0.00214	0.0155	1.39	1.23
Pb	<0.058	<0.06	0.108	0.088	<0.04	<0.047	<0.038	<0.04	3.9	3.8	<0.0117	<0.045	13.8	14.6
Bi	<0.0314	<0.0303	0.0166	0.0121	<0.0151	<0.0183	<0.0175	<0.0175	<0.0193	<0.0177	0.0046	<0.015	0.0043	0.0045
Th	<0.0141	<0.0134	<0.0038	<0.006	<0.0032	<0.011	<0.0045	<0.004	0.0187	0.0295	<0.00229	0.049	0.0037	0.00215
U	0.0236	<0.013	0.0041	<0.0038	1.5	0.148	0.0094	<0.0142	0.0075	<0.0049	0.00242	0.192	<0.00101	<0.00089

Table 11 - Representative laser ablation in-situ trace element analyses of mineral phases from the Cignana serpentinite. All data are reported in µg/g.

Sample ZSG1403										
	Antigorite		Ti-Clinohumite		Diopside		Olivine		Magnetite	
Li	0.0074	<0.0271	2.29	3.12	0.299	0.242	2.6	1.12	1.28	0.9
Be	0.081	0.08	<0.9	<0.57	5.1	5	<0.0205	<0.078	<0.293	<0.142
B	5.1	4.9	7.1	3.3	0.67	0.75	1.63	9.4	0.136	<0.063
Sc	11	9.8	4.1	3.5	25.1	23	1.25	2.13	1.71	1.9
V	48	59	20.4	27.3	5.1	5.2	0.103	0.053	930	960
Cr	2190	2270	30.8	48	68	50	1.81	1.55	39000	32000
Co	57	61	206	211	14.5	14.7	198	208	216	219
Ni	1120	1360	2490	2480	174	177	2830	2770	2740	2750
Cu	2.31	2.06	2.05	2.28	0.85	0.86	1.98	2.11	0.09	<0.042
Zn	46	41	123	120	8	7.8	98	99	360	247
As	0.065	0.169	<0.109	<0.091	0.032	<0.0283	0.009	0.0257	0.054	0.0142
Rb	<0.00276	0.00284	<0.035	<0.0272	<0.0073	0.0109	0.00263	<0.0041	<0.0083	<0.0043
Sr	0.037	0.049	0.192	0.25	118	141	0.00145	0.0117	0.092	0.036
Y	0.47	0.37	0.153	0.143	39	40	0.01	0.281	0.128	0.0056
Zr	0.11	0.159	5.4	2.86	0.188	0.186	0.0089	0.0242	0.72	1.1
Nb	0.069	0.091	94	77	0.0078	0.0272	0.089	0.126	0.6	0.52
Mo	0.0255	0.0274	0.58	0.291	<0.043	0.039	0.202	0.157	2.18	1.87
Cd	0.0308	0.085	<0.246	<0.204	0.145	0.129	0.159	0.046	0.079	0.039
Sb	0.041	0.058	<0.138	<0.129	<0.038	<0.035	0.0122	0.0288	0.054	<0.0191
Cs	<0.00116	<0.00182	0.01	<0.0205	<0.0049	<0.0042	<0.00162	<0.00255	<0.0059	<0.00302
Ba	<0.0123	0.0127	<0.11	<0.098	<0.036	<0.0306	<0.00285	<0.0216	0.23	<0.0162
La	0.032	0.039	0.035	0.0287	1.68	1.85	0.00069	0.0246	0.07	0.0036
Ce	0.122	0.139	0.0259	0.066	7.6	8.2	<0.00141	0.0157	0.056	0.0057
Pr	0.0096	0.0108	<0.0184	<0.0124	1.28	1.29	<0.00083	0.0042	0.0079	<0.00254
Nd	0.037	0.037	0.0305	<0.057	6.3	6.2	<0.00165	0.0203	0.042	0.0034
Sm	0.0161	0.0102	<0.074	<0.0236	2.37	2.4	<0.0056	0.0035	<0.0291	<0.0143
Eu	0.0033	0.0039	<0.04	<0.0245	0.87	0.93	<0.00056	<0.00094	0.0044	0.00142
Gd	0.0278	0.0177	<0.0249	<0.086	3.6	3.7	<0.0073	0.0036	0.0154	<0.00281
Tb	0.004	0.005	<0.0104	0.0049	0.73	0.79	<0.001	<0.00125	0.00127	<0.00039
Dy	0.058	0.035	<0.059	<0.053	5.8	6.2	<0.0044	0.0131	0.0071	<0.00215
Ho	0.0135	0.0139	0.0098	0.0069	1.37	1.45	<0.00145	0.0081	0.0037	<0.00166
Er	0.066	0.064	0.0191	<0.06	4.6	4.7	<0.004	0.072	<0.023	<0.0116
Tm	0.0147	0.0117	<0.0213	0.0108	0.57	0.59	0.00174	0.0314	0.00139	<0.00042
Yb	0.162	0.118	0.223	0.09	3.2	3.4	0.0294	0.51	<0.0089	0.0059
Lu	0.04	0.0278	0.032	0.032	0.31	0.33	0.0099	0.144	<0.0047	<0.00233
Hf	0.0051	0.0111	0.107	0.036	0.0083	0.0095	<0.00114	<0.0052	0.092	0.075
Ta	0.00294	0.0073	6.9	6.4	<0.0034	0.0033	0.0036	0.0061	0.046	0.044
W	0.007	<0.0061	0.7	0.18	<0.0136	<0.0115	<0.00133	<0.00222	<0.016	<0.0076
Pb	0.0197	0.0073	<0.09	<0.074	0.4	0.41	0.0079	0.0093	<0.0222	<0.0119
Bi	0.0069	0.0191	<0.032	<0.0295	<0.0094	<0.0084	0.0253	0.0043	0.0088	0.0045
Th	0.0235	0.043	<0.0157	<0.005	0.0314	0.05	<0.00041	<0.00188	0.0064	0.00164
U	<0.00106	0.0035	<0.0132	<0.0119	<0.0037	0.0038	<0.00043	<0.00225	<0.0069	<0.0034

Table 12 - Representative laser ablation in-situ trace element analyses of mineral phases from Ti-chondrodite and Ti-clinohumite veins hosted in the Cignana serpentinite. All data are reported in µg/g.

	Sample ZSG1402								Sample ZSG1502							
	Ti-clinohumite		Apatite		Diopside		Chlorite		Ti-clinohumite		Olivine		Antigorite		Chlorite	
Li	2.91	3.08	<0.086	<0.193	<0.66	0.48	<0.44	<0.227	4	3.3	4.9	2.81	<0.127	<0.48	<0.18	0.09
Be	<1.31	<1.68	<0.49	<0.249	3.4	4.5	<1.18	<0.61	<0.57	<1.21	<0.67	<0.38	<0.43	<1.6	<0.4	<0.246
B	2.65	2.68	0.65	1.06	<1.28	0.52	0.98	0.87	1.85	2.96	1.16	4.1	2.17	1.83	0.66	0.68
Sc	5.3	5.6	0.47	0.42	36	42	12.2	8.5	3.3	3.4	2.18	1.64	10.2	8.6	6.2	5.6
V	30.4	38	0.54	0.63	9.6	11.6	117	95	25.2	17.9	0.231	0.103	65	56	80	75
Cr	19.8	42	<2.35	<2.36	115	22.1	1050	1380	33	23	4.3	3.9	1680	1830	2520	860
Co	175	175	<0.039	0.058	15.7	14.4	67	67	188	208	223	223	75	68	76	72
Cu	2.25	10.3	<0.186	1	1.04	0.89	1.56	1.22	1.31	0.78	1.19	1.33	1.78	2.87	1.5	1.21
Zn	116	116	<0.45	<0.45	7.9	7.3	36	35	121	140	104	105	46	58	44	32
As	<0.269	<0.294	4.2	3.9	<0.276	<0.097	<0.136	0.071	<0.057	<0.123	0.36	<0.0237	2.42	0.72	0.078	<0.0204
Rb	<0.072	<0.083	0.274	0.266	<0.094	<0.037	<0.05	<0.0255	<0.0197	<0.042	<0.0237	<0.0128	0.093	<0.075	<0.0142	<0.0092
Sr	0.65	0.7	2440	2500	170	183	0.064	0.052	0.147	0.118	0.118	0.291	0.57	0.37	0.08	0.042
Y	0.52	0.54	2270	2570	72	83	0.0276	0.071	0.141	0.075	0.032	0.307	0.62	0.5	0.0135	0.0127
Zr	4.2	2.33	0.89	0.92	0.243	0.32	0.087	0.09	3.2	5.3	<0.0198	0.125	0.85	0.28	0.046	0.082
Nb	140	190	0.89	0.47	<0.041	0.0133	<0.0251	0.058	14.1	13.8	0.0279	0.079	0.033	<0.037	0.011	<0.0043
In	<0.0288	<0.035	<0.0118	<0.0154	<0.0255	<0.0161	0.0305	0.0271	<0.0089	<0.019	<0.0095	<0.0054	0.0148	<0.0259	0.0147	0.0144
Sn	<0.27	0.43	<0.097	<0.095	<0.271	0.164	2.86	1.49	0.064	<0.136	<0.082	<0.043	0.144	<0.194	0.248	0.208
Sb	<0.305	<0.33	<0.106	<0.103	<0.308	<0.117	<0.151	<0.078	<0.057	<0.122	<0.059	<0.032	0.148	<0.139	<0.036	<0.0234
Cs	<0.055	<0.064	<0.0211	<0.0218	<0.046	<0.0205	<0.033	<0.0167	<0.0144	<0.0307	<0.0124	<0.0069	0.0105	<0.035	<0.0074	<0.0049
Ba	0.37	0.63	<0.165	0.134	<0.39	0.118	<0.235	<0.12	<0.0314	<0.067	<0.126	<0.07	0.234	<0.225	<0.076	<0.033
La	0.279	0.099	940	890	3.8	4.7	<0.041	<0.0211	<0.0042	<0.009	<0.0117	0.0173	0.0137	0.049	<0.007	<0.0055
Ce	0.61	0.217	2460	2260	17.7	19.1	<0.0254	<0.013	0.0049	<0.0095	0.0069	0.036	0.085	0.159	<0.00284	<0.0046
Pr	0.037	<0.038	288	264	3.2	3.4	<0.0068	<0.0034	<0.0034	<0.0072	<0.0035	0.00267	0.0114	0.032	0.00238	<0.0035
Nd	0.38	<0.212	1240	1140	19	17.9	<0.104	<0.053	<0.064	<0.136	<0.054	<0.0309	0.075	0.06	<0.032	<0.0252
Sm	<0.198	<0.243	304	281	7.3	6.9	<0.043	<0.0218	<0.0226	<0.048	<0.062	<0.036	<0.042	<0.158	<0.037	<0.0234
Eu	<0.055	<0.068	50	49	1.49	1.41	<0.0121	<0.0061	0.0073	<0.0141	<0.007	<0.0047	<0.0146	<0.057	<0.0042	<0.0027
Gd	<0.195	<0.24	360	360	9.6	10	<0.044	<0.0219	<0.0227	<0.048	<0.062	<0.036	<0.042	<0.158	<0.037	<0.0234
Tb	<0.0254	<0.0312	57	55	1.65	1.81	<0.0153	<0.0078	0.0034	<0.0066	<0.0033	<0.00221	0.007	<0.0212	<0.00197	<0.00126
Dy	0.051	0.099	360	370	12.1	13.5	<0.0229	<0.0115	<0.034	<0.073	<0.0137	0.034	0.056	<0.088	<0.0083	<0.0053
Ho	<0.032	<0.038	71	81	2.27	2.66	<0.0157	<0.008	<0.0033	0.0077	0.0038	0.0085	0.0178	0.0131	<0.00206	<0.0033
Er	0.076	<0.075	204	249	6.6	8.3	<0.07	<0.036	0.0273	<0.0316	0.0171	0.043	0.106	0.074	<0.0094	0.0088
Tm	0.0203	<0.016	25.4	32	0.73	1.05	0.0061	<0.00277	<0.0081	<0.0173	<0.0107	0.008	0.0103	<0.0301	<0.0064	<0.0051
Yb	0.38	0.5	144	186	4.7	6.3	<0.096	<0.049	0.145	<0.141	0.071	0.14	0.106	<0.135	<0.033	0.021
Lu	0.105	0.104	18.1	22.7	0.52	0.66	0.0128	0.0215	0.0189	0.038	0.036	0.0281	0.035	<0.0219	0.0055	0.0039
Hf	<0.087	<0.107	0.0208	<0.033	<0.034	0.0172	<0.068	<0.035	0.069	0.111	<0.039	<0.0221	0.041	<0.03	<0.0236	<0.0115
Ta	7.5	12.2	0.0116	0.0147	<0.0103	<0.0212	<0.0061	<0.00305	0.72	0.79	<0.0095	<0.0055	<0.0082	<0.033	<0.0057	<0.00139
W	0.096	0.197	0.261	0.136	<0.045	<0.057	<0.106	<0.054	<0.0154	<0.033	0.047	0.149	<0.0137	<0.041	<0.0249	<0.0061
Tl	<0.073	<0.087	<0.0211	<0.0273	<0.046	<0.0261	<0.033	<0.017	<0.0169	<0.036	<0.0151	<0.0087	<0.0091	<0.033	<0.0091	<0.007
Pb	<0.134	<0.156	1.87	1.17	0.9	0.69	<0.088	<0.045	<0.046	<0.098	<0.0274	<0.0153	0.0213	<0.078	<0.0164	<0.0142
Bi	<0.083	<0.096	<0.0265	0.036	<0.101	<0.05	<0.05	<0.0258	<0.0047	<0.01	<0.0128	<0.0073	<0.0115	<0.046	<0.0077	<0.006
Th	<0.085	<0.102	69	76	<0.0266	0.08	<0.0154	<0.0077	<0.0045	<0.0096	<0.0127	<0.0073	<0.0092	<0.035	<0.0076	<0.00194
U	<0.044	<0.057	10.2	16.2	<0.0225	<0.0253	<0.032	<0.0164	<0.0042	<0.0089	<0.0045	<0.00307	<0.0069	<0.0246	<0.00274	<0.0034

Table 13 - Representative laser ablation in-situ trace element analyses of mineral phases from the Zermatt serpentinite. All data are reported in µg/g.

ZSG1406											
	Serpentine			Ti-Clinohumite		Diopside			Magnetite		
Li	<0.0208	<0.0106	<0.0067	0.215	0.5	1.32	1.07	1.02	1.34	0.35	<0.34
Be	<0.051	<0.044	<0.039	<0.037	<0.068	<0.077	<0.075	<0.086	<0.042	<0.4	<0.41
B	23.3	32	9.9	22.4	21.5	18.9	24.1	23.1	16.4	1.46	0.86
Sc	12.4	12.5	11.3	14.2	29.7	65	7.8	8.6	90	1.03	0.85
V	25.9	25	23.2	19.5	14.8	18.2	17.4	18.2	18.2	198	203
Cr	1640	2630	530	90	60	104	298	330	141	4000	3500
Co	9	8.6	8.2	56	50	37	27.1	31	17.7	86	84
Ni	286	213	210	550	480	380	410	480	320	1920	1690
Cu	9.5	4.4	3.7	2.79	2.52	2.55	46	19.9	2.4	3.2	0.97
Zn	19.5	19.1	15.6	57	50	42	34	33	45	138	134
As	0.51	0.53	0.235	0.0139	<0.0048	0.0078	0.81	0.89	0.0075	0.051	<0.045
Rb	0.0045	<0.00312	<0.00257	<0.0026	<0.0048	<0.0041	<0.0043	<0.0049	<0.00182	<0.0236	<0.0291
Sr	0.0164	0.0225	0.014	0.198	0.205	0.36	0.109	0.098	0.4	0.035	0.044
Y	0.311	0.208	0.221	0.087	0.117	0.12	1.01	1.07	0.138	0.174	0.15
Zr	0.5	0.41	0.295	4.9	4.3	8.3	2.08	2.04	3.9	0.91	0.313
Nb	0.0208	0.0205	0.0195	0.86	1.14	2.93	0.53	0.41	1.87	0.073	0.041
Mo	0.0285	0.0238	0.0289	0.283	0.289	0.36	0.191	0.205	0.39	0.271	0.34
Cd	0.0226	0.026	0.1	0.034	0.0297	<0.023	0.0292	<0.0256	0.0296	<0.182	<0.226
Sb	0.17	0.167	0.096	0.0117	<0.0095	<0.009	0.116	0.122	0.0052	<0.064	<0.089
Cs	<0.00221	<0.00189	<0.0021	<0.00159	<0.00293	<0.00193	0.0047	0.0039	<0.00143	<0.0206	<0.025
Ba	<0.0106	<0.0145	0.0036	0.0311	<0.0212	<0.0044	<0.0294	<0.034	0.01	<0.059	0.038
La	0.006	0.0072	0.0064	0.00249	0.00102	<0.00232	0.047	0.046	<0.00093	<0.0216	<0.0254
Ce	0.0204	0.0154	0.0194	0.0064	0.00163	<0.00202	0.115	0.114	<0.00094	0.033	0.0206
Pr	0.0035	0.0033	0.00274	<0.00093	<0.00172	0.00048	0.0137	0.0152	<0.00091	0.0107	0.005
Nd	0.0153	0.0208	0.0204	0.0104	0.0044	<0.0069	0.108	0.099	<0.00131	0.069	<0.065
Sm	0.0117	0.0113	0.0087	0.0062	<0.01	<0.0081	0.039	0.055	<0.00154	<0.09	<0.099
Eu	0.0032	0.004	<0.00216	<0.00155	<0.00289	<0.00085	0.0095	0.0086	0.00066	<0.0261	<0.0287
Gd	0.0291	0.0154	0.0211	0.009	0.0066	0.0034	0.105	0.099	0.0024	<0.041	0.0265
Tb	0.0038	0.00189	0.0049	0.0012	0.00132	<0.00115	0.0148	0.0167	0.00057	0.0082	0.006
Dy	0.041	0.0174	0.0313	0.006	0.0067	0.0061	0.103	0.143	0.0044	<0.0316	0.027
Ho	0.0105	0.0091	0.0085	0.00219	0.00247	0.00292	0.038	0.042	0.0032	0.0162	0.008
Er	0.043	0.0188	0.0313	0.0095	0.0217	0.0188	0.141	0.116	0.0244	<0.074	<0.085
Tm	0.0055	0.0049	0.0037	0.00227	0.0054	0.0079	0.0273	0.0249	0.0095	<0.0119	<0.0121
Yb	0.054	0.045	0.042	0.0287	0.062	0.105	0.185	0.192	0.131	<0.041	0.035
Lu	0.013	0.0093	0.0065	0.0078	0.0165	0.035	0.043	0.039	0.046	<0.0068	0.0072
Hf	0.028	0.0221	0.01	0.092	0.088	0.164	0.074	0.059	0.084	0.035	<0.0136
Ta	0.00083	0.00136	0.00069	0.0297	0.032	0.099	0.0174	0.0088	0.083	<0.0068	<0.0039
W	0.0078	0.0101	0.0055	0.216	0.0306	0.056	0.34	0.268	0.069	0.0296	0.0172
Pb	0.06	0.0129	0.0165	0.0066	<0.0087	<0.0089	0.0144	0.0229	0.0066	<0.056	<0.071
Bi	0.0062	0.0053	0.0272	0.0173	0.0042	0.0037	<0.0037	<0.0043	0.0082	<0.0226	<0.0266
Th	0.00173	<0.0019	0.0012	<0.000299	<0.00058	<0.0006	<0.00254	0.00299	<0.001	<0.0149	<0.0152
U	<0.00078	<0.00077	0.00147	0.00102	0.00111	0.00138	0.00239	0.00203	0.00073	<0.0096	<0.0105